Department of Aerospace Science and Technology

Master of Science in Aeronautical Engineering

Characterization of liquefying fuels for hybrid rocket propulsion

Supervisor:
Professor Luciano GALFETTI

Candidate:
Francesca CAIELLI
898979

Academic year 2019-2020

Abstract

The limitation of low regression rate in hybrid rocket propulsion can be overcome through the use of liquefying fuels. These form a melt layer over the grain, which allows mechanical mass transfer of fuel into the oxidiser flow by an entrainment process. The most promising fuel formulations are $n-$alkanes, specifically paraffin-based fuels, which show a good trade-off between structural properties and regression rate enhancement through entrainment.

In this work the behaviour of different paraffin formulations under the effect of an oxidiser flow was studied by numerical means, using a multiphase solver of OpenFOAM. The influence of the viscosity and of the surface tension on the onset of the entrainment and on the primary break-up time was recorded, resulting to be in accordance with the theoretical model for hybrid combustion.

The evolution of the temperature in the combustion chamber was considered; its influence is of essence for the residence time of the fuel droplets, but also for the characterisation of the transport and thermophysical properties that are required for numerical simulations. A simplified case was setup using a multi-region solver of OpenFOAM, as a basis for a future simulations, including both fluid interaction and heat transfer. The simplified implementation, considering only conjugate heat transfer, allowed for a sensitivity analysis of the two-dimensional temperature profile when changing the thickness of the melt layer and the flame location. The heat fluxes at the interfaces were also calculated. The results showed an increasing surface temperature and a decreasing heat flux of the liquid layer with its thickness, and a decreasing trend for both as the flame location is shifted upwards.

Acknowledgments

I wish to thank Professor Luciano Galfetti for the opportunity of working on such a fascinating subject, and for his guidance in these troubling times.

I also express my gratitude to all my friends in Italy and all around the world; a virtual hug to all of you in the hope of sharing a real one soon.

A huge thank you to Davide, always ready to help and encourage me in all my adventures and choices.

Finally, my full gratitude to my family, whose support was fundamental in all my years of study; you were the ones that made all of this possible.

Contents

List of Figures

List of Tables

List of Symbols

The next list describes symbols and acronymes that will be later used within the body of the document

Acronyms and Abbreviations

ABCs Asymptotic Behavior Correlations

ABS   Acrylonitrile Butadiene Styrene

BC   Boundary Condition

CFD   Computational Fluid Dynamics

HTP   High-Test Peroxide

HTPB Hydroxyl-Terminated Polybutadiene

RANS Reynolds-Averaged Navier–Stokes

SEBS Styrene-Ethylene-Butylene-Styrene

TNT   Trinitrotoluene

VOF   Volume Of Fluid

Greek Symbols

α Dynamic pressure exponent for entrained mass flow rate

α_p Weight fraction of radiative particles

α_{phase1} Indicator function

β Thickness exponent for entrained mass flow rate

δ Thermal thickness $[m]$

γ Dynamic viscosity exponent for entrained mass flow rate

$\hat{\alpha}$ Absorptivity

$\hat{\sigma}$ Stefan-Boltzmann constant $[W/m^2/K^4]$

κ_l Thermal diffusivity $[m^2/s]$

λ Thermal conductivity $[W/m/K]$

μ Dynamic viscosity $[kg/m/s]$

ν Kinematic viscosity $[m^2/s]$

ϕ Non-dimensional thermal parameter

π Surface tension exponent for entrained mass flow rate

ψ Non-dimensional regression rate

ρ Density $[kg/m^3]$

σ Surface tension $[N/m]$

ε Emissivity

φ Non-dimensional radiation parameter

Roman Symbols

$\Delta H f^o$ Enthalpy of formation $[J/mol]$

Δh Enthalpy difference $[J/kg]$

$\dot{m}$ Mass flow rate $[kg/s]$

$\dot{Q}$ Heat flux $[W/m^2]$

$\dot{Q}_c$ Convective heat flux $[W/m^2]$

$\dot{Q}_r$ Radiative heat flux $[W/m^2]$

$\dot{r}_{\mathrm{cl}}$ Regression rate predicted by classical theory $[m/s]$

$\dot{r}$ Regression rate $[m/s]$

$\mathbf{u}$ Velocity vector

$\mathbf{x}$ Position vector

A Amplitude

a Absorption coefficient $[1/m]$

a_p Constant for particle cloud emissivity

a_t Thickness parameter $[m^2/s]$

a_{ent} Entrainment coefficient

B Blowing parameter

B_g Evaporation blowing parameter

B_{rad} Radiative blowing parameter

C Specific heat $[J/kg/s]$

C_f Skin-friction coefficient

C_{B1}, C_{B2} Blowing correction coefficients

C_{f0} Skin friction for a turbulent flow over a flat plate

e_0 Entrainment coefficient

F_r Heat-transfer correction factor for surface roughness

G Instantaneous mass flux $[kg/m^2/s]$

h Thickness of the melt layer $[m]$

h_e Total heat of entrainment $[J/kg]$

h_m Total heat of melting $[J/kg]$

h_v Total effective heat of gasification $[J/kg]$

K Entrainment parameter coefficient

k_n Wave number

L_m Latent heat of melting $[J/kg]$

L_v Latent heat of vaporisation $[J/kg]$

n Number of carbon atoms

N_p Particle number density

Nu Nusselt number

O/F Oxidiser to fuel mass ratio

P_c Combustion chamber pressure $[Pa]$

P_d Dynamic pressure of the oxidiser $[Pa]$

Pr Prandtl number

q_r Radiative energy flux $[J/m^2/s]$

R Ratio thermal to radiative thickness

R_{he} Ratio of effective heats of gasification for entrainment

R_{hv} Ratio of effective heats of gasification for vaporisation

Re Reynolds number

S Surface $[m^2]$

St Stanton number

T	Temperature $[K]$
t	Time
T_a	Initial solid fuel temperature $[K]$
T_m	Melting temperature $[K]$
T_v	Vaporisation temperature $[K]$
T_{cg}	Congealing point temperature $[K]$
u	Velocity $[m/s]$
V	Volume $[m^3]$
W	Molecular mass $[g/mol]$
x	Distance from the interface $[m]$
X_e	Entrainment parameter $[N^{-0.5}]$
z	Axial distance from grain leading edge $[m]$

Subscripts

ent	Entrainment
b	Flame zone
e	Edge of boundary layer
f	fuel
g	Gas phase
i	i-th cell
j	j-th face
l	Liquid phase
s	Solid phase
v	Vaporisation
w	Wall

Chapter 1

Introduction

Hybrid rockets are a promising technology, unifying advantages of solid and liquid rockets for more reliable and cost effective propulsion systems. They are characterized by the storage of fuel and oxidizer in different states of matter, conventionally a liquid oxidiser and a solid fuel. The main obstacle to the realization of this technology is the low regression rate of the solid propellant. A solution is offered by liquefying fuels, such as paraffin based fuels, that are solid at room temperature and produce a low-viscosity liquid when melted. The instabilities originated in the melted layer lead to droplet formation and entrainment in the oxidizer flow, significantly enhancing the fuel mass transfer. M. A. Karabeyoglu, D. Altman, and B. J. Cantwell, through their research at Stanford University and with the Space Propulsion Group, in the late '90s started developing an extensive theoretical model for the liquid layer hybrid propulsion theory. Paraffin based fuels and their properties have been largely investigated, leading to the launch of a sounding hybrid rocket propelled by solid paraffin and liquid nitrous oxide, by the start-up HyEnD, in cooperation with the DLR Institute of Space Propulsion and University of Stuttgart, in 2018[26].

1.1   Thesis motivations

The technology represented by hybrid rocket motors potentially stands for a turning point in the space exploration, opening the way to a more reliable, cost-effective and environment friendly launch vehicles. Their realization is approaching through the use of liquefying fuels, but, thought many theoretical and experimental studies have been performed about this configuration, the fully characterization of the combustion process has still to be carried on. Thus, the current work is conducted in order to understand the main factors affecting the entrainment process and the temperature profile across the solid, liquid and gaseous phase, which has a direct influence on the entrainment and evaporation of the fuel droplets. This is crucial to understand which kind of characteristic the liquefying fuel should possess to allow an optimal combustion performance, in addition to the ones that satisfy the structural needs of the rocket. Since the most promising solution is offered by paraffin fuels, formulations based on paraffin are analysed and considered in the study of the temperature profile and entrainment phenomenon.

1.2   Thesis work objectives

The aim of this work is to identify proper numerical tools to simulate the processes ongoing in a hybrid rocket motor. Firstly, the visualisation of the entrainment process through a multiphase solver is performed. This kind of simulation could give a better understanding of the phenomenon, by evaluating how fuel and oxidizer properties influence hydrodynamic instabilities origination, primary breakup times and droplets characterization. Also, it would represent a convenient tool to compare the behavior of different paraffin-based fuels. Secondly, a simulation of the temperature profile and the heat flux across the two interfaces solid/liquid and liquid/gas is performed with a multi region conjugate heat transfer solver. The effect of the melt layer thickness and of the flame location on the evolution of the temperature in the combustion chamber is analysed. Although it is not possible during this time to perform an experimental study to validate the numerical simulation, the sensitivity to some parameter underlined by the simulations is of importance to better understand the influence of the fuel formulation. Also, the main challenges related to the numerical computation and the promising features which would have to be further developed and tested are highlighted.

1.3   Presentation plan

The outline of the work is organised as follows.

Chapter 2: Literature survey

This chapter illustrates the concept of the hybrid rocket motors, with the main benefits and the possibilities of improvement. An overview of the developed models for the hybrid rocket combustion theory is presented, along with previous numerical modelling for the entrainment and the temperature evaluation.

Chapter 3: Physical and mathematical modeling of the liquefying fuels behaviour

The hybrid rocket motor classical combustion theory and extended hybrid theory for liquefying fuels are explained in details.

Chapter 4: Investigated paraffin-based formulations

The characteristic of the paraffin-based fuel employed for the simulation are reported, together with the procedure to obtain them or the literature reference from previous experimental results. The characteristic of gaseous oxygen are also reported.

Chapter 5: Numerical simulation of the entrainment

The operation of the multiphase solver used for the simulation is described. The results obtained with the different paraffin formulations and with different initial interface and turbulent model are reported, showing the influence on the primary break-up time and on the entrainment visualization.

Chapter 6: Numerical simulation of the temperature profile through the solid, liquid and gaseous phase

The heat flux at the interfaces, the trend of the temperature profile along the three different phases and at the liquid surface in the axial direction are presented in this chapter. It is illustrated the operating of the multi region solver and the calculation with the software CEA for the flame temperature and the properties of the combustion products. A sensitivity analysis to the thickness of the melt layer and the flame height is then performed.

Chapter 7: Conclusions and future work

This chapter contains a summary of the performed numerical modelling and presents suggestion for future improvement and further analysis to perform.

Chapter 2

Literature survey

This chapter is devoted to explain the concept and the functioning of the hybrid rocket engines. The goal is to underline the potential of this technology and the difficulties that have still to be overcome for the it to take off at large scale.

2.1 Hybrid Rocket Motor

In order to operate in vacuum conditions, rocket engines store both fuel and oxidiser. The reactants are forced to mix in a combustion chamber and after the ignition, the combustion reaction takes place. The combustion products are drove towards a nozzle, where the exhausted gas expand and accelerate, thus generating thrust. The risk of chemical explosion is intrinsic with this configuration, leading to high costs of propellant handling and safety hazards during launch. Hybrid rocket motors stands as a possible alternative; by storing the oxidizer as a liquid and the fuel as a solid, the possibility of chemical explosion is significantly reduced, both in flight and during ground operations.

2.1.1 Concept

There are two major configurations of hybrid rockets, that have been investigated up to now. The classical one involves a pressure vessel with liquid oxidiser and a cylindrical combustion chamber where the solid fuel is stored, with one or more port for the oxidizer to flow through. The two parts are mechanically separated with a device, like a valve, and an ignition system is present in the combustion chamber.
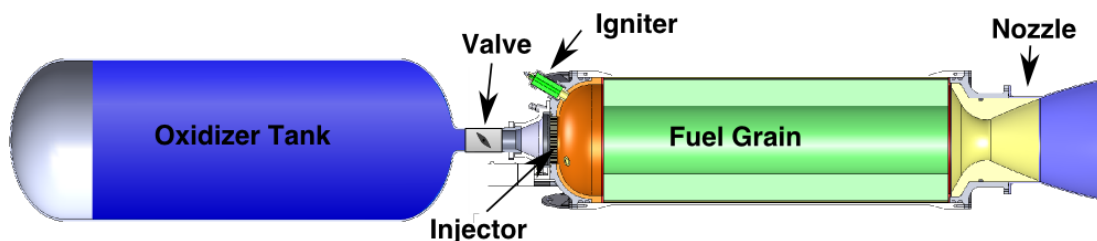
Figure 2.1.1: Conceptual schematic of a hybrid rocket propulsion system.

The vaporisation of the liquid oxidiser is possible through the addition of hot gas

generator to heat the oxidizer in a pre-combustion chamber, or decomposition by catalysis, or addition of small amount of hypergolic propellant. Once the valve is opened, the vaporised oxidiser flows into the ports. The fuel sublimates, or melts and subsequently evaporates, thus mixing with the oxidizer. When the ignition is started, a diffusion flame establishes where the mixture is stoichiometric; the rise of temperature would make the process of gasification of the solid fuel self-sustained. There are many processes taking place at this stage. The fuel undergoes a thermal heating and pyrolysis process. The polymer fragments are desorbed from the pyrolyzing fuel surface and diffused towards the flame zone. The oxidiser forms a boundary-layer shear flow close to the surface and it diffuses towards it. Heterogeneous reactions take place, propagating the pyrolysis front and the heating over the exposed fuel surface. As the port area increases, the axial mass flux is reduced. The bulk flow is accelerated in the axial direction and ejected through the nozzle.

Another possible configuration is the vortex hybrid rocket engine, which shows interesting possibilities of enhancing regression rate and avoid the presence of unburnt species in the nozzle. In this case, the oxidizer is injected tangentially into the chamber; an outer, annular flow field spirals up the fuel port walls while an inner, core vortex carries the combustion products through a unique exit nozzle. The centrifugal forces generated by the swirling flow lead to high, axially uniform regression rates and neutral burning.
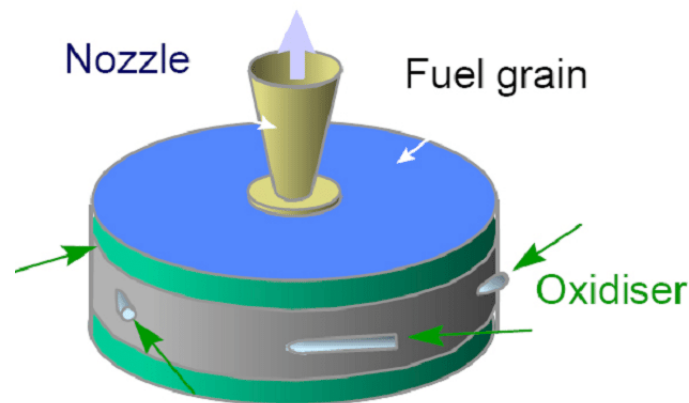
Figure 2.1.2: Conceptual schematic of a vortex flow hybrid engine[12].

2.1.2   Fuel and oxidiser

Among the choice of fuels, the two main competitors are synthetic rubbers, like hydroxyl-terminated polybutadiene (HTPB) and acrylonitrile butadiene styrene (ABS), and liquefying fuel. The former are safe to handle and have high energy content; besides, HTPB has a long history of use in solid rocket motors. The latter are a promising solution to increase significantly the regression rate, as it will be further discussed later. The enhancement using these fuels were reported to be up to 400%, by researchers at the Air Force Research Laboratory (AFRL)[31] and ORBITEC[20]. The Goldilocks conditions among hydrocarbon liquefying fuels can be found in paraffin wax: it is cheap to produce and transport, solid at ambient temperature, inert, and environmentally-friendly, having simply carbon dioxide and water as by-products. The low structural performance, though,

leads to the necessity of additives that, by changing the melting point and the viscosity, partially reduce the benefits on the regression rate.

The manufacturing process is also important, when considering the costs and the performance of a particular configuration. Traditional casting techniques may be expensive when complex geometries are required, like multi-port combustion chamber, or may require internal webbing to support the grain. Additive manufacturing technique can overcome these challenges. Peculiar configurations like helical ports have been tested with ABS, conferring good regression rate and volume efficiency[33].

Most common oxidisers are liquid oxygen, nitrous oxide and hydrogen peroxide. There has been large experience with liquid oxygen in rocket engines, because of its readily availability and its high specific impulses. However, its cryogenic conditions leads to the necessity of high-pressurized tanks. Nitrous oxide is a possible alternative; having self-pressurizing properties, it permits a simple propulsion system with good performance, without external pressurization[26]. An interesting liquid oxidiser is the high-test peroxide (HTP), a highly concentrated solution of hydrogen peroxide ($80-99\%$)[55]. It decomposes catalytically or thermally, with high adiabatic temperature, that could eliminate the need for ignition device. Furthermore, hydrogen peroxide and its decomposition products are non-toxic.

2.1.3 Benefits and possible applications

The main advantages of hybrid rockets regard safety, compared with solid rockets, and the absence of mechanical complexity, compared with liquid. This is why the realization of large scale hybrid launcher will perfectly suit manned flight, both for commercial and exploration purposes, and the possibility of space-storable rocket motors for planetary missions. At small scale, hybrid sounding rockets were successfully tested in 2018, by Nammo[15] and HyEnD[26]. These carry instruments to perform scientific experiments and measurement in sub-orbital flight; the hybrid rocket technology allows them to avoid toxic combustion products, typical of solid propellant, and to match the thrust profile more accurately with the mission requirements.

The main benefits that are leading to the development of this kind of engine can be summarized as follows:

- **Avoided safety hazard:** the TNT equivalent of zero, due to the different phases of fuel and oxidiser, avoid danger during storage and handling; there is no risk of auto-ignition due to heating or stray electrical charges, and it is also more resilient to process errors, like grain crack. Even in case of failure, the difficulty in oxidiser and fuel mixing could prevent the risk of explosion. Also, the solid grain breaks up acoustic waves, accounting for less high frequency combustion instabilities than in liquid engine combustion chamber.

- **Reduced system complexity:** compared to liquid propelled rockets, there is less need of plumbing and valves, and the operations are simpler. It is also possible to avoid turbo-pump, by employing self-pressurized oxidiser or blow-down system. Since the combustion chamber is lined with solid fuel, a cooling system is not necessary.

- **Enhanced performance and flexibility:** the specific impulse is higher than solid and lower than liquid. However, it can be easily improved with metal additives, that increase also density, reducing the overall system volume when compared with liquid propellant. Still, the thrust is throttable and the combustion can be stopped and restarted, permitting flexibility in flight operations.

- **Environmentally-friendly:** there is no need for toxic and harmful solid propellant, but simple hydrocarbon fuel can be used instead, avoiding the release of toxic substances in the atmosphere during launch.

All these characteristics lead also to reduced costs of production and transport, accomplishing more affordable sub-orbital and space flights for national agencies and private companies.

2.1.4   Challenges and possible solutions

There are still some drawbacks linked to hybrid rocket motors, that require improvements and alternative solutions with respect to previous technologies.

- **Low regression rate:** the main difficulty to overcome is the very low burning rate, which is a direct consequence of the different phases of oxidiser and solid fuel, that need to be vaporised for the combustion to happen. This problem is further increased by the blocking effect, which is the blowing from the solid fuel towards the flame reducing the convective heat transfer, thus the evaporating mass transfer; also, the boundary layer is thickened and the flame sheet is displaced further from the fuel surface. Possible adjustments are multi-port fuel grain, with poor volumetric and structural efficiency as side-effect, swirl injectors, that add system complexity, adding small amount of oxidiser into the fuel, thus having the possibility of safety hazards. The most promising solutions are turbulence generators device, to improve mixing and convective heat transfer, and liquefying fuels, with mechanical mass transfer.

- **Shifting oxidiser/fuel ratio:** the increase in diameter of the fuel port results in an increased fuel mass flow rate, which has to be compensated by increasing oxidiser mass flow rate. The ratio varies not only during the burn, but also along the grain, decreasing down the port.

- **Post-combustion chamber:** inadequate mixing and flame stabilisation lead to incomplete reactions, requiring a post-combustion chamber to have efficient combustion.

- **Low frequency instabilities:** these are caused by coupling of the feed system of the liquid oxidiser, which needs to be vaporised, and by the boundary layer combustion behaviour. The first one especially causes a vaporisation lag, leading to low frequency pressure oscillations (50% of the mean chamber pressure).

- **Turbo-pumps for large rockets:** turbo-pumps may be needed to achieve high flow rates and pressurization of the oxidiser in large hybrid rockets; they would need to be powered by the liquid oxidiser or by the hot gases in the combustion chamber, leading to a more complex system.

- **Re-usability:** the liquid tank can be re-fueled, but the solid fuel can not be pumped into the combustion chamber, which needs to be manufactured again; this allows low opportunities of reusable hybrid rockets.

2.2 Hybrid rocket combustion model

In hybrid engines the combustion happens within the turbulent boundary layer developed by the flow of the oxidiser over the fuel slab. The mechanism is markedly different from the one occurring in liquid and solid rocket, and it is modeled after turbulent diffusion flames.

The oxidiser is fed from the port in the combustion chamber; it develops a boundary layer that growths over the grain surface. After the ignition, the fuel vaporises and enters the boundary layer, mixing with the other reactant. Where the local mixture ratio reaches stoichiometric conditions, the combustion reaction occurs and the diffusive flame is originated. The released thermal energy sustains the vaporization process of the fuel grain by convection and radiation, so that the mixing in gaseous phase and the combustion reaction continue. The boundary layer is divided into two parts, the oxidizer-rich and the fuel-rich zone, with the flame as a discontinuity, as it is schematized in Figure 2.2.1.
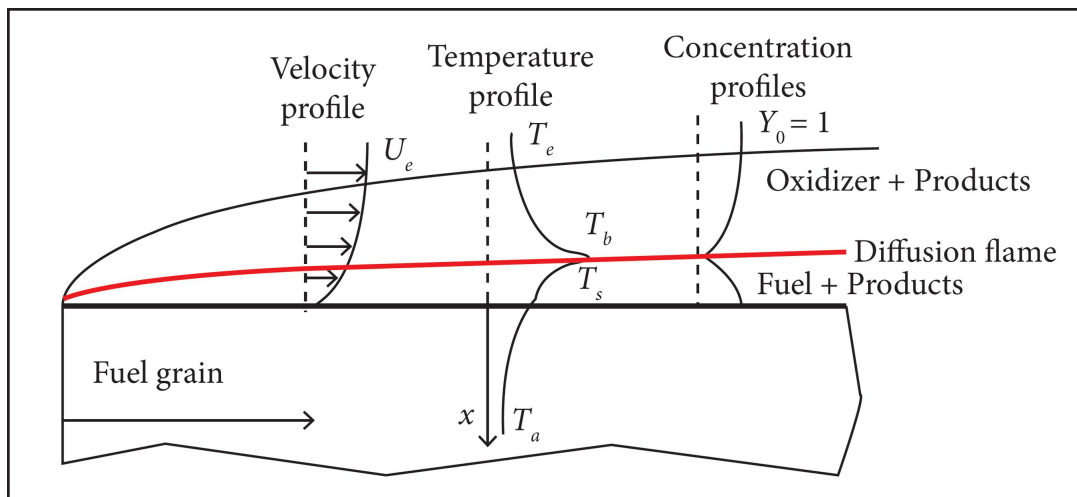
Figure 2.2.1: Schematic of the classical hybrid fuel combustion mechanism[9].

Once the flame is established, the combustion is then governed by the rate at which the heat is driven to the fuel surface, determining the regression rate of the solid grain. This parameter is of great importance, since it dictates the exhaust mass flow through the nozzle, and consequently, the thrust. It is therefore necessary to establish a theoretical model, to be able to predict with accuracy the regression rate of a given propellant and for given dimensions and structure of the engine. Being the low burning rate the main drawback of hybrid rockets, this would also provide some insights to find a possible solutions.

Marxman[36][37] and coworkers developed a model based on diffusion-limited processes, which was then modified by Karabeyoglu and coworkers[23][24] to take into account

some peculiarities of liquefying fuels. This advancement was essential to include the phenomenon of entrainment, which significantly raises the regression rate by mechanical fuel mass transfer.

2.2.1 Diffusion-limited model

Diffusion-limited reactions are those in which the reaction rate depends solely on the speed at which solute molecules diffuse to the site of reaction[54]. Following this model, in the '60s Marxman and coworkers published a formulation of the regression rate in hybrid combustion process, which agreed reasonably with the experimental data. They stated that the combustion is controlled by the rate at which heat can be delivered to the fuel surface, rather than by the surface reaction rates, the main affecting factors being the position of the flame and the effective heat of gasification[36]. The latter corresponds to the total energy required to gasify a unit mass of solid fuel originally at the internal temperature of the solid grain. The dependency is expressed as follows:

$$\rho_f \dot{r} = \dot{Q}_w / h_v \tag{2.2.1}$$

Under the assumption of turbulent flow along the length of the grain, of heat transfer only due to convection, of no liquid layer formation and of reaction at stoichiometric conditions, the regression rate is found to be dependent on the mass flux, the dynamic viscosity of the gas phase, the position along the grain and the blowing parameter. The last one accounts for the modification of the skin friction with respect to the case of a turbulent flow over a flat plate, due to the convective blockage. The mass flow towards the flame is opposed to the heat flux, thus reducing the effective convective heat transfer and being an obstacle for the enhancing of the regression rate.

In a successive work[37], radiation heat transfer was considered; since this one is not affected by the convection blockage, the blowing parameter is corrected to take into account the radiation effect. This contribution is particular important when there is fuel grain with metal additives or generation of soot particles.

2.2.2 Liquid layer hybrid combustion theory

Karabeyoglu and coworkers[23] developed an extensive theory considering the case when a melted layer is formed before the vaporisation of the solid grain. The peculiarity of the liquefying fuels is the origination of hydrodynamic instabilities in a gas flow environment, leading to substantial droplet entrainment into the gas stream. This results in having two different mass transfer mechanisms: a thermal one and a mechanical one. The last one, not being affected by the blocking factor, may dominate and confer the liquefying fuels that much higher regression rate observed with experiments. Also, the blocking factor is reduced, because of the presence of two-phase flow in the boundary layer, and the heat transfer increases due to the surface roughness, which extends the contact fuel area. Thus, the mass transfer due to vaporisation is enhanced, too.

The ideal characteristics for the fuel are then found in low viscosity and surface tension, that help develop shear driven instabilities. To express all the dependencies and to find the best performing propellants, the formulation of the regression rate including the entrainment process needs to be developed.

$$\dot{r} = \dot{r}_v + \dot{r}_{\text{ent}} \tag{2.2.2}$$
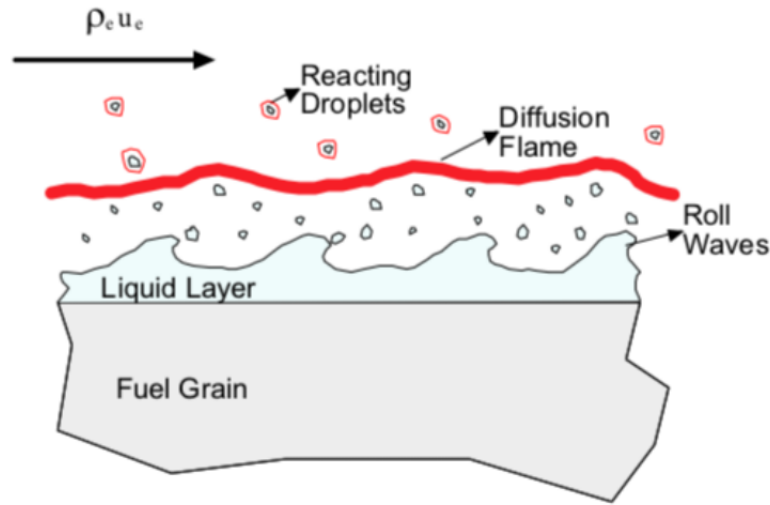
Figure 2.2.2: Schematic of the entrainment mechanism[22].

The major steps are the definition of the effective heat of gasification, majorly reduced due to the mechanical transfer of the fuel droplets, the thickness of the melt-layer, and the entrainment parameter. The prediction of entrainment onset for a liquid layer and the resulting mass transfer was studied by Gater and l'Ecuyer in 1970[19], by means of experimental correlations. In light of their results and of other experimental findings, Karabeyoglu suggested an empirical expression to estimate the entrained liquid mass, depending on the dynamic pressure of the gas flow, the thickness of the liquid layer, the viscosity of the liquid layer, and the surface tension.

These progresses lead to the formulation of the extended hybrid rocket theory, with the definition of the non-dimensional regression rate formulation, normalized by classic regression rate. This can be expressed as a dependency of the local mass flow, axial coordinate and the fuel properties. The calculation of the burning rate therefore requires the knowledge of these parameters over the whole range of operating condition of the motor. The material property estimation of the homologous series of normal alkanes $(C_n H_{2n+2})$ has been object of the work of Karabeyoglu and coworkers, resulting in a good matching of theory and experiment for n varying between 5 and 100000[22]. The high heat of combustion, due to the high hydrogen to carbon ratio, low cost, availability and chemical inertness characteristics of these materials designate them as ideal fuels for hybrid rockets. The components of interest are methane, pentane, paraffin waxes and high-density polyethylene; paraffin waxes especially show a trade-off between entrainment realization and structural properties, also avoiding the use of cryogenic fuel.

2.3 Numerical analysis for hybrid combustion

The classical and the extended hybrid combustion theory have been object of various experimental tests. These lead to the validation of the theory and the characterisation

of the fuel, rocket geometry and operational parameters, with the goal of enhancing hybrid engines performances. A potential tool for the investigation of the phenomenon and the study of the possible improvements is represented by the numerical analysis. By means of CFD software, the comparison among different configurations could be made inexpensively and the numerical results could be easily recorded. The difficulty in the set-up of a numerical simulation for hybrid rocket engines arises from the multiple complex phenomena that characterize their combustion model, especially the coupling with the two-phase reacting flow-field and the fuel consumption mechanism[14]. Some steps have been already taken in the effort of characterise the entrainment phenomenon in a turbulent boundary layer at ambient condition, the temperature evolution across the different phases and the regression rate of the slab.

2.3.1   Numerical simulation of the entrainment

The combustion of liquefying fuels is taken in consideration by Di Martino et al.[13], when investigating the computational thermo-fluid-dynamic model of the internal ballistics of hybrid rockets burning gaseous oxygen and paraffin-based fuel. The interface between the gas and the fuel surface is treated with local mass, energy and mean mixture fraction balances; an analytical expression is added for the calculation of the entrainment fraction of the fuel consumption rate, considering the correlation $\dot{r}_{\text{ent}} \propto a_{\text{ent}}G^{2\alpha}/\dot{r}^{\beta}$. Their calculated regression rate is in good accordance with experimental results from laboratory-scale rocket. The influence of the entrainment parameter was studied and reported as in Figure 2.3.1. As a_{ent} increases, larger entrainment is produced; the parameter is inversely proportional to the viscosity of the melt layer and the gas density, thus the higher contribution of entrainment is obtained with lower viscosity and chamber pressure, implying less stabilization of the liquid film surface.
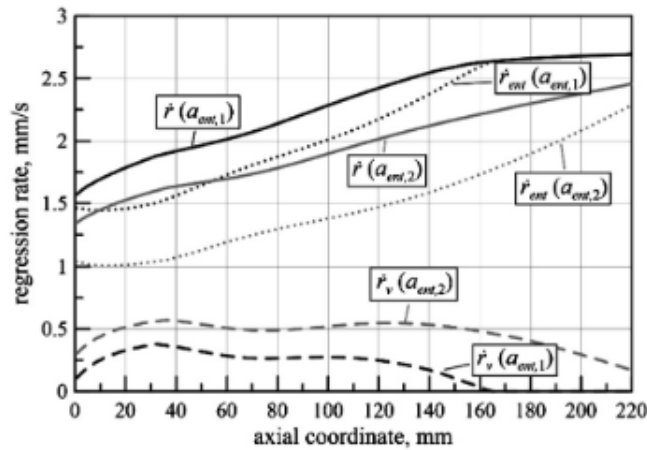
Figure 2.3.1: Effect of the entrainment parameter on the axial profiles of the regression rate, $a_{\text{ent},1}* = 2.1\text{x}10^{-13}$, $a_{\text{ent},2}* = 1.1\text{x}10^{-13}$[13]

In this computational analysis the prediction of the mechanical transferred mass of fuel is only performed analytical, which means that the spray characterisation is not performed. The results depend only on the modelling of the entrainment phenomenon.

Knol and Maicke[25] implemented a simulation with OpenFOAM, in order to study the behaviour of fuel liquid film under gas blowing. Since the focus is on the formation of the droplets, chemical reactions and heat transfer are not considered to reduce computational complexity and to focus on the fluid instability. They considered the case of liquid paraffin wax at rest subjected to a shear force caused by flowing air, with a sinusoidal inference between the two fluids. The wax-air interface is defined by the following function.

$$x = x_{mean} + A\sin(k_n z) \tag{2.3.1}$$

As the time runs, additional small-scale features are introduced in the initial perturbations, as the flow instability starts to develop; this effect becomes more and more significant as the simulation advances, leading to peaks elongation, and eventually, droplet detachment from the fuel surface. The evolution for the baseline case is reported in the following figure, where the red part is paraffin and the blue is air. Cyclic conditions are imposed on the lateral sides as a way to reduce the computational domain and to conserve the entrained mass flow.
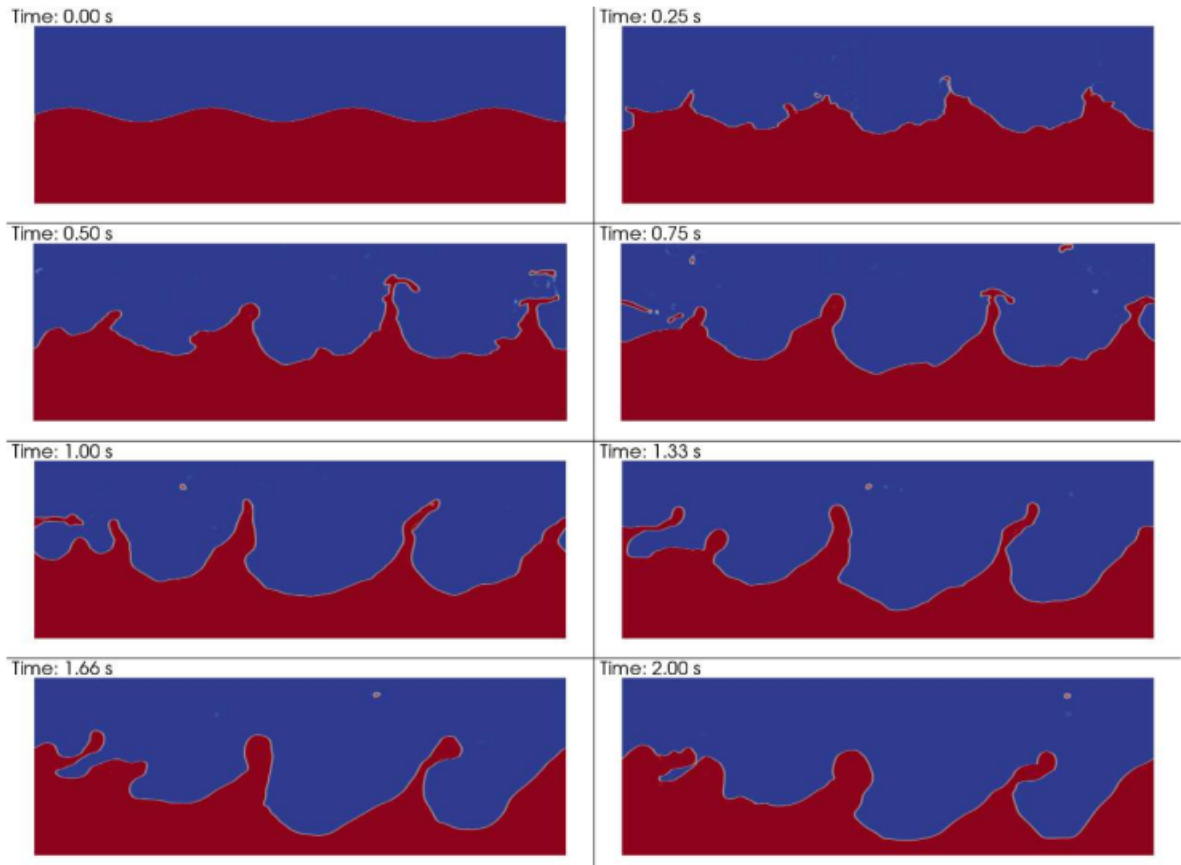
Figure 2.3.2: Paraffin distribution with $A = 0.01m$ and $k_n = 10\pi rad/m$[25]

The variation of operational parameters and interface geometry is analysed. They found that increasing amplitude can lead to significant increased entrainment over a certain threshold. Also velocity of the gas and chamber pressure have a positive effect

on the entrained mass transfer. Future work is identified in expanding the range of gas flow velocities, interface frequencies and investigating the impact of turbulence modeling on the entrainment rate of the liquid fuel droplets.

Following the work of Knol and Maicke, a simulation employing OpenFOAM multiphase solver `interIsoFoam` was implemented by Berniguad[6] at the SPlab. This solver allows the user to overcome the smearing of the interface caused by the Volume Of Fluid method, by sharpening the interface. The `isoAvector` algorithm for surface compressing uses the concept of isosurfaces to more accurately compute the face fluxes for the cells containing the interface. Thanks to this tool, not only the growth of instabilities, but also the single droplets can be detected, in order to measure their diameters and calculate the total entrained mass. This part was done thanks to the software ImageJ for image processing. The computational analysis involved a geometry corresponding to a test chamber for entrainment visualization present at the SPLab. The results are in good agreement with previously performed tests with this experimental set-up; the mechanically transferred mass is proportional to $\mu_l^{-0.191}$ and $P_d^{1.60}$.
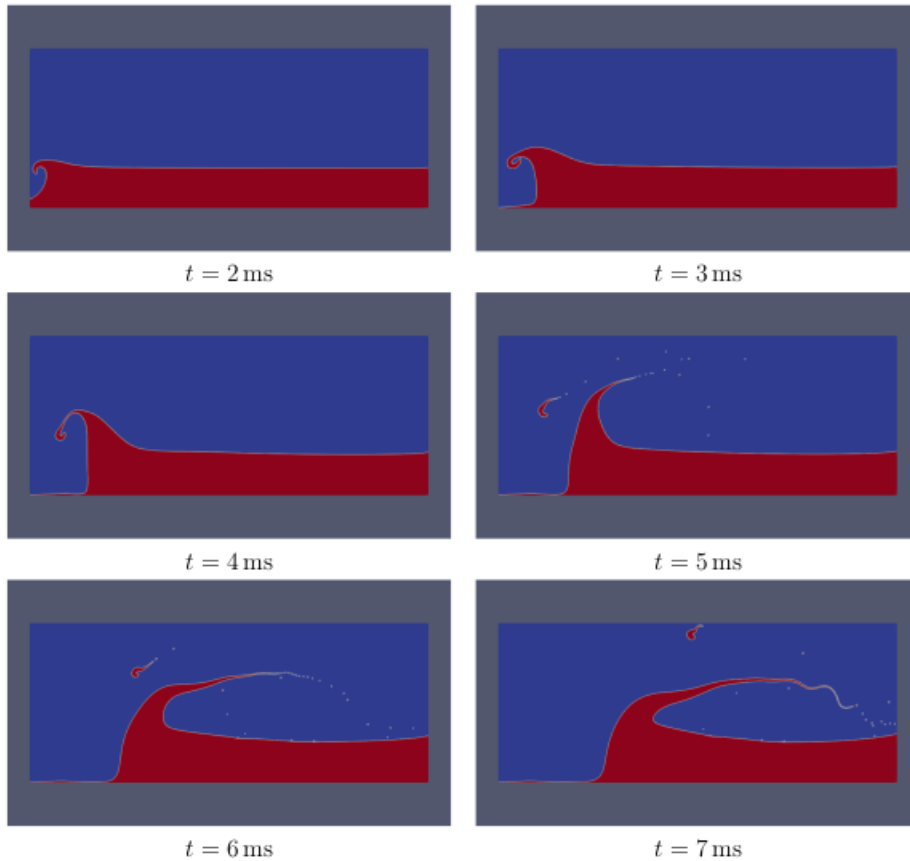
Figure 2.3.3: Entrainment of paraffin Sasol Wax 0907 $u_g = 35m/s$, $h = 2mm$ [6]

As it can be observed in Figure 2.3.3, the initial interface is plane and a rolling wave is forming once the velocity starts to flow from the inlet port on the left. A $k - \varepsilon$ model is implemented, so that the turbulence effects are modeled. As for Figure 2.3.2, the red part corresponds to liquid paraffin wax and the blue one is air.

2.3.2 Temperature and regression rate evaluation

A simulation for the flame structure typical of hybrid rockets was implemented with OpenFOAM by Gariani et al.[18]. First a case involving solid HTPB and gaseous oxygen is considered. The computational domain is split into a solid phase region, where only conductive heat transfer is considered, and a gas phase region, with fluid dynamics and combustion reaction equations. The conservation of mass and energy at the interface is imposed and the surface pyrolysis is treated by Arrhenius law. The wall effects are considered, and RANS equations with $k - \varepsilon$ model closure are used. The values derived from the code are representative for steady-state behavior. A macroscopically diffusive flame in the turbulent, reactive boundary layer stabilizes above the solid fuel due to the interaction between fuel blown from the solid phase and axial oxidizer injection. The temperature profile at the mid point of the fuel slab, in Figure 2.3.4, shows a maximum temperature of $3500K$ about $2mm$ from the solid surface. The evolution of temperature is in good agreement with the classical diffusion flame theory, with typical turbulent temperature boundary layer and diffusive flame structure. The model is also in good agreement with experimental results on the regression rate by Chiaverini[11].
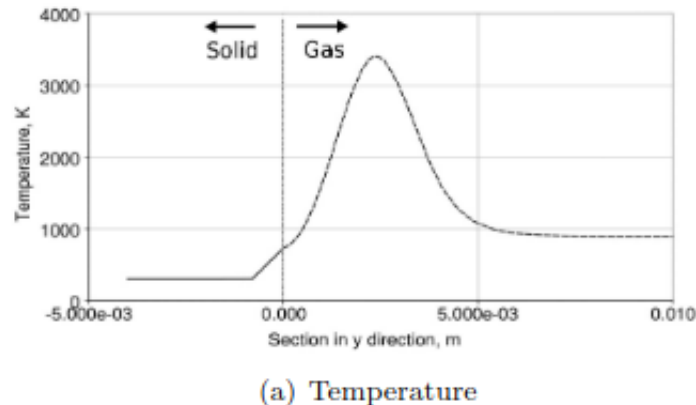
(a) Temperature

Figure 2.3.4: Temperature profile at mid point of the slab for $u_{inlet} = 60m/s$, $P = 1.3bar$, $t = 1s$, normally to the oxidizer injection [18]

A two-phase flow model is also implemented, considering the combustion of aluminum droplets in the core flow. They are inserted with zero velocity inside the gas dynamic field just above the burning surface, simulating the release of metal from the fuel surface. Initial locations vary along the slab, then particles are trailed by blowing fuel gases and mix with oxidisers. The temperature evolution in the chamber strongly depends on the injection location of the droplets, which is represented by p in Figure 2.3.5, from the closest to the farthest from the leading edge.

15
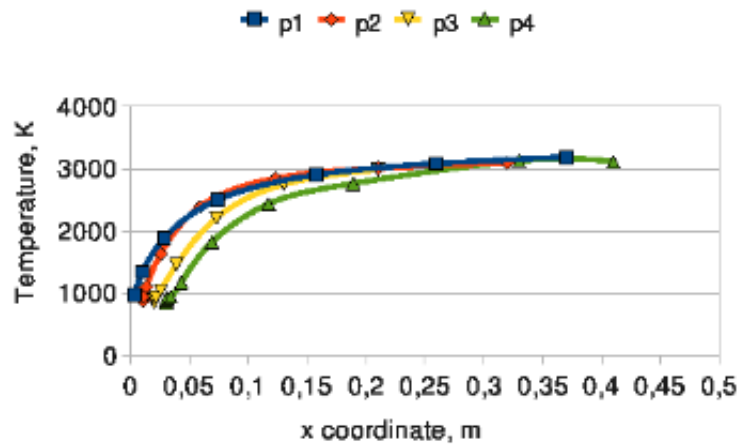
Figure 2.3.5: Temperature profile at mid point of the slab for aluminium particles, $u_{inlet} = 60m/s$, $P = 1.3bar$, parallel to the oxidizer injection[18]

Chapter 3

Physical and mathematical modeling of the liquefying fuels behaviour

The modeling of combustion of liquefying hybrid propellant and the main corrections with respect to the classical theory of Marxman are here further analysed. The focus is mainly on the entrainment behaviour and the temperature evaluation through the three different phase of the fuel, that will be part of numerical analysis.

3.1   Classical regression rate

Starting from the hypothesis of convective heat transfer $\dot{Q}_c$ being largely dominant with respect to radiation, the expression of the heat flux per unit area can be written as:

$$\dot{Q}_w = \dot{Q}_c = \rho_f \dot{r} h_v \qquad (3.1.1)$$

The effective heat of gasification h_v is the heat required to produce unit mass of volatile products from unit mass of solid, initially at standard temperature and pressure[52]. Thus, it includes the heat of sublimation (or melting and vaporisation for liquefying fuels) and the heat of reaction for polymers degradation into volatile products. Its value and the density of the fuel ρ_f depends on the chosen propellant, while the convective heat flux at the wall has to be determined to get the regression rate.

The Stanton number is introduced for this purpose. It measures the ratio of heat transferred into a fluid to the thermal capacity of the fluid, and it can be expressed in terms of the Nusselt, Reynolds, and Prandtl numbers.

$$St = \frac{\dot{Q}_c}{\rho_b u_b \Delta h_{bw}} = \frac{Nu}{PrRe} \qquad (3.1.2)$$

The difference in gas-sensible enthalpy Δh_{bw} is calculated between the flame zone and the gas at the wall, the density ρ_b and the velocity u_b are evaluated at the flame zone.

In a turbulent flow, the Reynolds analogy can be used to link the convective heat flux and the shear stress inside the boundary layer. It states that there is an analogy between

energy and transport momentum, since they both depend on turbulent eddies. Assuming unity of Lewis and Prandtl numbers, the expression of Stanton number becomes:

$$St = \frac{1}{2}C_f \left(\frac{\rho_e u_e^2}{\rho_b u_b^2} \right) \tag{3.1.3}$$

The velocity u_e and density ρ_e are related to the main stream flow, and they can be rewritten as the oxidiser mass flow G. The equation 3.1.1 can be rewritten, linking the regression rate with the skin friction coefficient.

$$\rho_f \dot{r} = \frac{1}{2}C_f G \left(\frac{u_e \Delta h_{bw}}{u_b h_v} \right) \tag{3.1.4}$$

The term in the brackets characterize the blowing parameter B, evaluating the relevance of the unit mass flow rate injected transversely into the boundary layer with respect to the corresponding axial quantity in the free stream. The skin friction coefficient can also be written as a function of this parameter. The value of C_f for turbulent flows over a flat plate needs indeed to be modified as follows, due to the flowing fuel from the surface towards the flame zone.

$$\frac{1}{2}C_f = \frac{1}{2}C_{f0}f(B) = 0.036Re_z^{-0.2}f(B) \tag{3.1.5}$$

The dependency on the blowing parameter in literature has been defined as an exponential relation, the exponent being 0.77 in Marxman theory[37] or 0.68 in more recent work of Altman[5]. The resulting regression rate according to Marxman model is then:

$$\rho_f \dot{r} = 0.036G \left(\frac{z\rho_e u_e}{\mu_e} \right)^{-0.2} Bf(B) \tag{3.1.6}$$

$$\dot{r} = 0.036\frac{G^{0.8}}{\rho_f} \left(\frac{z}{\mu_e} \right)^{-0.2} B^{0.23} \tag{3.1.7}$$

Once the propellant is determined, the regression rate in flight operation depends on the oxidiser mass flow and on the axial location along the grain. As this increases, the skin friction reduces, also decreasing the local regression rate.

$$\dot{r} \propto G^{0.8}z^{-0.2} \tag{3.1.8}$$

3.1.1 Influence of radiation

In order to include the contribution of radiative heat transfer, equation 3.1.7 is modified, adding a a gray-body radiation term.

$$\dot{r} = 0.036\frac{G^{0.8}}{\rho_f} \left(\frac{z}{\mu_e} \right)^{-0.2} B^{0.23} + \frac{\hat{\sigma}\varepsilon_w \left(\varepsilon_g T_b^4 - \hat{\alpha}_g T_w^4 \right)}{h_v \rho_f} \tag{3.1.9}$$

The temperatures are respectively the flame and wall temperature, and the coefficients corresponds to the emissivity of the wall ε_w, emissivity of the gas ε_g and absorptivity of gas $\hat{\alpha}_g$.

For this expression to be valid, the coupling between radiative heat transfer and convective blockage has to be considered, by applying a corrective factor to the blowing parameter B. This happens because the energy of radiation tends to increase the rate of fuel vaporization, and this increase, in turn, tends to decrease the rate of convective heat transfer to the wall[37]. The expression connecting the corrected blowing parameter to the convective and radiative heat transfer is:

$$\frac{B_{rad}}{B} = 1 + \frac{\dot{Q}_r}{\dot{Q}_c}\left(\frac{B_{rad}}{B}\right)^{0.77} \tag{3.1.10}$$

Over a wide range of values of $\dot{Q}_r/\dot{Q}_c$ the solution can be approximated by this relation:

$$\frac{B_{rad}}{B} = \exp\left(1.3\frac{\dot{Q}_r}{\dot{Q}_c}\right) \tag{3.1.11}$$

A simple close form formulation for the diffusion-limited regression rate, including radiation, is then yelded by:

$$\dot{r} = \frac{\dot{Q}_c \exp(-\frac{\dot{Q}_r}{\dot{Q}_c}) + \dot{Q}_r}{h_v \rho_f} \tag{3.1.12}$$

3.1.2 Influence of pressure

Some experiments conducted in the '60s by Smoot and Price[51] showed a variation of regression rate with pressure, when in presence of high mass flow rate. Also the dependency on G was lacking in the cases with $G > 70 kg/(m^2 s)$. Other experiments by Chiaverini et al. in 2007[29] confirmed this fact; in these cases the higher pressures cause higher regression rate due to larger overall heat flux to the fuel surface. It was also shown that for low mass flow rate the influence of radiative heat transfer becomes more important as pressure increases. The Figure 3.1.1 shows the effects of pressure.
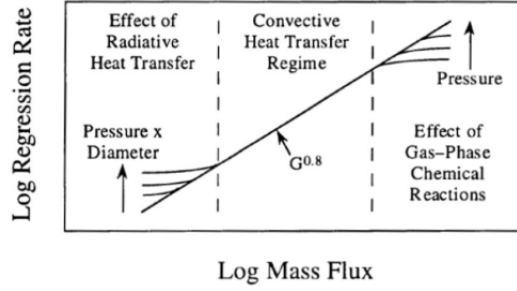
Figure 3.1.1: Effect of pressure, radiation heat transfer and total mass flux on the regression rate[29].

However, equation 3.1.12 does not have explicit dependence on pressure. Some modifications were proposed by Wooldrige et al.[57] and Muzzy[40], to take into account the pressure-dependent correlation concerning gas-phase kinetics. For low pressure cases, the kinematics influence is more and more significant with respect to convection.

$$\dot{r} \propto P_c^{0.5} G^{0.3} z^{-0.2} \tag{3.1.13}$$

The presence of radiative particles, like soot, is also strongly affected by pressure, since it modifies their density. This case was analysed by Strand et al.[53], who proposed to explicitate the relation of radiant heat transfer to the presence of soot.

$$\dot{Q}_r = \hat{\sigma} \varepsilon_g T_b^4 \left(1 - e^{-a_p N_p} \right) \tag{3.1.14}$$

$$a_p N_p = 0.134 \cdot \frac{\alpha_p P_c}{1 + O/F - \alpha_p} \tag{3.1.15}$$

This model shows the influence of pressure on the radiative heat transfer, that can dominates on convection when the contribution radiative particles is not negligible. α_p is the soot particle weight fraction and is dependent on the chosen propellant.

3.2   Extended hybrid theory

Karabeyoglu et al. developed an extended hybrid theory that considers also the case of a liquid film formation before the gasification of the fuel. This is the model currently considered, especially when referring to liquefying fuels, like paraffin wax.

There are three main parts in the development of this model:

- The requirements for the formation of the liquid film, its thickness and thermal characteristics.

- The onset and the transferred mass of the entrainment, through the study of the linear stability of the liquid layer.

20

• The correction of the classical formulation of the regression rate, to consider the contribution of the entrainment.

3.2.1   Liquid layer thickness and thermal analysis

Under the combined effect of convection and radiation, a melted layer of is formed on the solid surface of liquefying fuels. The energy transfer in the gaseous, liquid and solid phase determines the thickness of this layer. A one-dimensional model is considered, schematized in Figure 3.2.1. The following assumption are considered for the development of the theory:

• The liquid-gas interface and the solid-liquid interface are assumed equal and constant, since the steady-state regression rate is investigated; the melt layer thickness is constant as a consequence.

• The thermophysical properties of the material are uniform.

• The conduction heat transfer is dominant in the liquid layer, because the small thickness allows for small Reynolds numbers and large temperature gradients; the convective heat transfer is neglected in the melted layer, while the penetration of radiative heat transfer is considered.

• The radiation contribution from the slab is negligible with respect to the thermal radiation of the flame, as well as the incoming radiation's non collimated effects; the liquid and the solid fuel are assumed to be grey bodies, so that the absorption coefficients are independent of the frequency of radiation.
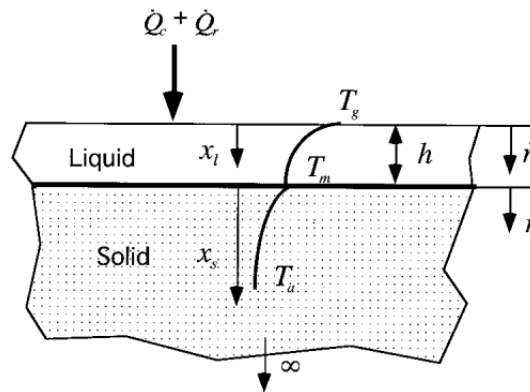
Figure 3.2.1: Schematic of the thermal model for the melt layer thickness estimation[23].

The radiative energy flux is written as follows, where x_l and x_s are the local coordinates for the liquid and solid phase respectively, $\dot{Q}_r$ is the total heat flux at the surface and a is the absorption coefficient.

21

$$q_r\left(x_l\right) = \dot{Q}_r e^{-a_l x_l} \tag{3.2.1}$$

$$q_r\left(x_s\right) = q_r(x_l = h)e^{-a_s x_s} = \dot{Q}_r e^{-a_l h}e^{-a_s x_s} \tag{3.2.2}$$

The radiative heating of material can be then expressed as the divergence of the radiative flux, mono-dimensional in this model; the integration of this expressions shows that the total heating of the fuel by radiation matches the radiative heat input.

$$\int_0^h a_l\dot{Q}_r e^{-a_l x_l}\mathrm{d}x_l + \int_0^\infty a_s\dot{Q}_r e^{-a_l h}e^{-a_s x_s}\mathrm{d}x_s = \dot{Q}_r \tag{3.2.3}$$

Energy equation

When writing the energy equation for the liquid layer, a finite velocity of the liquid particles has to be considered. The density difference between the two phases causes this vertical velocity component, that can be written as a mass balance across the liquid-solid interface $u_l = (\rho_s/\rho_l - 1)\,\dot{r}$. In the reference frame of the regressing surface the net liquid velocity is $(\rho_s/\rho_l)\,\dot{r}$. The characteristic thermal thickness of the liquid layer can then be expressed as $\delta_l = \kappa_l\rho_l/\dot{r}\rho_s$, from which the energy equation results:

$$\frac{\mathrm{d}^2 T}{\mathrm{d}x_l^2} + \frac{1}{\delta_l}\frac{\mathrm{d}T}{\mathrm{d}x_l} = -\frac{a_l\dot{Q}_r}{\kappa_l\rho_l C_l}e^{-a_l x_l} \tag{3.2.4}$$

The general solution for this linear ordinary differential equation and the boundary conditions are as follows.

$$\begin{cases} T\left(x_l\right) = c_1 e^{-x_l/\delta_l} + c_2 - \frac{\dot{Q}_r}{\rho_l C_l\dot{r}(a_l\delta_l-1)}e^{-a_l x_l} \\ T(x_l = 0) = T_v \\ T(x_l = h) = T_m \end{cases} \tag{3.2.5}$$

A similar procedure is applied to the solid phase, with a different definition of the thermal thickness $\delta_s = \kappa_s/\rho_s$.

$$\frac{\mathrm{d}^2 T}{\mathrm{d}x_s^2} + \frac{1}{\delta_s}\frac{\mathrm{d}T}{\mathrm{d}x_s} = -\frac{a_s\dot{Q}_r}{\kappa_s\rho_s C_s}e^{-a_s x_s} \tag{3.2.6}$$

$$\begin{cases} T\left(x_s\right) = c_1 e^{-x_s/\delta_s} + c_2 - \frac{\dot{Q}_r e^{-a_l h}}{\rho_s C_s\dot{r}(a_s\delta_s-1)}e^{-a_s x_s} \\ T(x_s = 0) = T_m \\ T(x_s \to +\infty) = T_a \end{cases} \tag{3.2.7}$$

Considering the liquid-solid interface, the energy balance can be written by matching the heat conducted into the solid and the latent heat of fusion to the energy transfer from the liquid layer to the interface.

$$- \lambda_l \frac{\mathrm{d}T}{\mathrm{d}x_l}\bigg|_{x_l=h} + \lambda_s \frac{\mathrm{d}T}{\mathrm{d}x_s}\bigg|_{x_s=0} - L_m \rho_s \dot{r} = 0 \qquad (3.2.8)$$

The gradients can be derived from equations 3.2.5 and 3.2.7. Also the liquid-gas interface energy balance equation is formulated, having convective heat transfer from the gas phase matching the conductive heat transfer into the liquid and the latent heat of vaporization.

$$\dot{Q}_c + \lambda_l \frac{\mathrm{d}T}{\mathrm{d}x_l}\bigg|_{x_l=0} - L_v \rho_s \dot{r}_v = 0 \qquad (3.2.9)$$

By adding the equations 3.2.8 and 3.2.9 together and operating the proper substitutions, the expression of the total energy absorbed in the fuel slab is found to be equal to the energy required to heat the liquid and solid phases and the latent heat for phase transformations.

$$\dot{Q}_w = \dot{Q}_c + \dot{Q}_r = h_e \rho_s \dot{r} + L_v \rho_s \dot{r}_v \qquad (3.2.10)$$

The formulations of the total effective heats are as follows, where $\Delta T_1 = T_v - T_m$ and $\Delta T_2 = T_m - T_a$.

$$\begin{aligned} h_m &= L_m + C_s \Delta T_2 \\ h_e &= h_m + C_l \Delta T_1 \end{aligned} \qquad (3.2.11)$$

The effective heat of gasification can be then calculated from the classical expression 3.1.1. The importance of this new formulation is that it takes into account the effects of entrainment; thus only contribution of the evaporating liquid to h_v is considered, and not the one of the entrained droplet, which are not vaporized at the surface. Indeed, $\dot{r}_v$ is the component of the regression rate solely due to the vaporisation of the solid fuel.

$$h_v \equiv \dot{Q}_w / \rho_f \dot{r} = C_l \Delta T_1 + C_s \Delta T_2 + L_m + L_v (\dot{r}_v / \dot{r}) \qquad (3.2.12)$$

Thickness of the melt layer

Two parameters related to the thickness h of the liquid layer can be defined.

$$\phi = e^{-h/\delta_l} \qquad (3.2.13)$$

$$\varphi = e^{-a_l h} \qquad (3.2.14)$$

By inserting the temperature derivative expressions in the equation 3.2.8 and performing several simplifications, the following relation between ϕ and φ is obtained.

$$\phi = \frac{h_m \rho_s \dot{r} (a_l \delta_l - 1) + \dot{Q}_r \varphi}{h_e \rho_s \dot{r} (a_l \delta_l - 1) + \dot{Q}_r} \qquad (3.2.15)$$

23

The dependence on the regression rate can be replaced by the effective heat of gasification obtain with the expression 3.2.12. Also, the parameter $R_l = a_l \delta_l$, which express the ratio of the thermal thickness to the radiative thickness in the liquid layer, is introduced; by expressing the relation $\varphi = \phi^{R_l}$, a non-linear equation for the thickness parameter ϕ as function of the effective heats is obtained.

$$\phi = \frac{h_m \left(R_l - 1\right) + h_v \left(\dot{Q}_r/\dot{Q}_w\right) \phi^{R_l}}{h_e \left(R_l - 1\right) + h_v \left(\dot{Q}_r/\dot{Q}_w\right)} \tag{3.2.16}$$

The melt layer thickness is independent of the absorptivity of the solid material, since the contribution of the solid phase is expressed through the heat transfer from the solid to the interface, namely h_m and h_e. The thickness of the liquid layer should then be found by inverting the definition of ϕ and obtaining its value from equation 3.2.16.

$$h = \delta_l \ln\left(\frac{1}{\phi}\right) \tag{3.2.17}$$

An explicit solution for the non-linear equation 3.2.16, yielding the expression of h, could not be achieved for a general case. Therefore, two limiting cases for R_l are considered.

- $R_l >> 1$, which is the extreme case of opaque liquid layer, with the radiative heat all absorbed at the liquid-gas interface. This case is of importance for strongly absorbing propellants, like the ones with additive carbon black.

$$h = \delta_l \ln\left(1 + \frac{C_l \Delta T_1}{h_m}\right) \tag{3.2.18}$$

  The ratio of radiative and convective heat transfer and the one of the total regression rate and its vaporisation component do not affect the previous equation. Thus, for absorption happening in the liquid phase the entrainment factor is not fundamental in the determination of the thickness of the liquid layer.

- $R_l << 1$, which is the case of all the radiative flux absorbed in the solid

$$h = \delta_l \ln\left[1 + \frac{C_l \Delta T_1}{h_m - h_v \left(\dot{Q}_r/\dot{Q}_w\right)}\right] \tag{3.2.19}$$

  The effect of the entrainment mass transfer on the thickness is important in this case, as well as the ratio of the radiative heat flux to the convective heat flux.

In both cases the thickness of the melt layer is directly dependent on δ_l, thus inversely dependent on the total regression rate. As this increases, the liquid phase becomes thinner. Another significant parameter is the ambient temperature of the slab, which determines h_m, since the film thickness increases with it.

3.2.2   Stability of the liquid layer

The hydrodynamic instability of the liquid film, generated by the velocity difference between the gas and liquid phase, is an essential condition for the entrainment phenomenon. Karabeyouglu et al. analysed the stability of the liquid layer subjected to blowing and large shear forces, showing that the layer can be unstable over a wide range of parameters[24]. To derive an expression for the entrained mass flow rate and the onset conditions for droplet detachment, a fully nonlinear investigation would be required; this study is avoided, by using previous experimental study and the linear stability results to develop some empirical relations. The experiments of Gater and L'Ecuyer[19], concerning thin films of various liquids under strong blowing, also with hot gas flow, lead to relate the entrainment conditions and mass trasnfer to the liquid mass flow rate.

Entrainment onset

The main results of the linear stability analysis are:

- The melt layer is unstable over a finite range of wave numbers, even at low values for the film thickness. These kind of instabilities are generated by the interaction of the gas phase shear stresses acting on the liquid surface with the slope of the liquid layer surface.

- The amplification rate and the most amplified wave number increase with the Reynolds number of the gas flow. Thus, at higher velocity of the oxidiser mass flow, the wavelength of the instabilities are expected to be smaller.

- A stabilising effect is brought to the liquid by increasing viscosity and surface tension.

Also, in many experimental studies a roll wave mechanism for the liquid entrainment is reported at high Reynolds numbers. The droplets can detach from the tips of the nonlinear waves due to the stresses exerted by the local gas flow.

The necessary condition for the onset of the entrainment is then present, but it is not sufficient to determine that detachment of droplets happens. This results when harmonic waves conforms into a non-harmonic waveform. The estimation for the verification of this condition is obtained through empirical correlations, derived by the experiments of Gater and L'Ecuyer. A dimensional proportionality function $e_0(X_e)$ is defined, that measures the part of liquid mass flow rate that is entrained into the gas flow. The correlation for this term and the entrainment parameter X_e are as follows:

$$e_0\left(X_e\right) = 1 - \exp\left[-1.06 \times 10^{-4}\left(X_e - 2109\right)\right] \tag{3.2.20}$$

$$X_e = \frac{P_d^{0.5}}{\sigma}\left(\frac{T_g}{T_v}\right)^{0.25} \tag{3.2.21}$$

If the entrainment parameter is lower than the critical value $2109N^{-0.5}$, the entrainment phenomenon does not happen. Below this critical value, the requirement of a minimum

amplification rate of the interface disturbance is not met. The realization of the entrainment therefore depends on the dynamic pressure P_d, the surface tension σ, and the difference between the average gas phase temperature T_g and the vaporisation temperature of the liquid layer T_v. This temperature ratio actually accounts for the density variation in the gas. Another empirical correlation is developed, that relates the critical conditions for the onset to more practical engine parameters, such as the oxidiser mass flow and the liquid layer film thickness[41]. This expression is only valid for a laminar liquid film, with $Re_l < 300$.

$$G^{1.6}h^{0.6} \geq 2.5 \times 10^{-3} \frac{1}{C_f^{0.8}} \frac{\rho_g^{1.3}}{\rho_l^{0.3}} \frac{\mu_l^{0.6}\sigma}{\mu_g} \qquad (3.2.22)$$

Entrained mass

According to the work of Gater and L'Ecuyer, the entrained mass flow rate per unit area is proportional to the dimensional proportionality function and the liquid mass flow rate per unit width of the test section. The following empirical correlation is considered.

$$\dot{m}_{\text{ent}} = 13.3 e_0 \left(X_e \right) \dot{m}_l \qquad (3.2.23)$$

The function $e_0(X_e)$ is obtained through the expression 3.2.20, while the mass flow rate within the melt layer is related to the properties of the gas flow and the liquid film, by using the shear force balance at the liquid gas interface.

$$\dot{m}_l = \frac{P_d C_f h^2 \rho_l}{2\mu_l} \qquad (3.2.24)$$

Karabeyouglu et al. modify this expression in order to consider the reduction of the liquid mass flow rate in the axial direction. The corrected correlation is as follows:

$$\dot{m}_{\text{ent}} = -13.3 \ln \left(1 - e_0 \right) \dot{m}_l \qquad (3.2.25)$$

There is anyway no global agreement on this reference, and multiple other experimental correlations were proposed by other researcher. Karabeyouglu et al. suggest an expression for condition far from the critical level for entrainment onset, that makes explicit the dependence on the relevant parameters of the hybrid engine:

$$\dot{m}_{\text{ent}} \propto \frac{P_d^\alpha h^\beta}{\mu_l^\gamma \sigma^\pi} \qquad (3.2.26)$$

The exponents for the dynamic pressure and the film thickness are suggested to be $\alpha = 1.5$ and $\beta = 2$ by Gater and L'Ecuyer[19], and $\alpha = 1$ and $\beta = 1$ by Nigmatulin et al.[42]. It is suggested $\gamma > \pi$, since at the near critical conditions operation of hybrid engines there is no sharp interface separating the liquid from the gas phase, and the surface

tension plays a less stabilising role compared to the viscosity. In following work[22], the distinction of supercritical and subcritical conditions is considered. In supercritical cases the surface tension dependency is dropped and the following form for the scaling law for the entertainment mass transfer is defined. Here the empirical entrainment parameter constants are collected as K and the dependence on the dynamic pressure is related to local mass flux in the fuel port as $P_d = G^2/2\rho_g$. For convenience, the thickness parameter $a_t = h\dot{r}$ is introduced.

$$\dot{m}_{\text{ent}} = K \frac{C_f \rho_l G^{2\alpha} h^\beta}{\mu_l} = K \frac{C_f a_t^\beta \rho_l}{\mu_l} \frac{G^{2\alpha}}{\dot{r}^\beta} \qquad (3.2.27)$$

Once the expression for the entrained mass flow rate is defined, the regression rate due to the entrainment phenomenon can be obtained considering the following relation.

$$\dot{m}_{\text{ent}} = \rho_l \dot{r_{\text{ent}}} \qquad (3.2.28)$$

3.2.3   Modification of the classical theory

The regression rate $\dot{r_{\text{cl}}}$ of the diffusion-limited model is taken as a reference for the non-dimensionalisation. The entrainment phenomenon requires to modify three major parameters with respect to the classical theory of Marxman:

- **Effective heat of gasification:** the mechanical entrained fuel is not vaporised at the surface, therefore the evaporation energy is lower. The presence of reactants in liquid phase also reduces the enthalpy difference between the flame and the surface, but this modification is negligible with respect to the previous one. Thus, the ratio of enthalpy difference to the effective heat of gasification increases in the case of entrainment, affecting the blowing parameter B.

- **Blocking factor:** the presence of two-phase flow modifies the convective heat flux to the surface, and thus, the blocking factor. This is then expressed as a function of B_g, which is the blowing parameter including only gaseous phase mass transfer from the surface.

$$\frac{C_f}{C_{f0}} \cong \frac{2}{2 + 1.25 B_g^{0.75}} = \frac{C_{B1}}{C_{B1} + C_{B2} \left(\dot{r}_v / \dot{r}_{\text{cl}}\right)^{0.75}} \qquad (3.2.29)$$

The coefficients are defined as follows.

$$C_{B1} \equiv \frac{2}{2 + 1.25 B^{0.75}}, \quad C_{B2} \equiv \frac{1.25 B^{0.75}}{2 + 1.25 B^{0.75}} \qquad (3.2.30)$$

- **Surface area:** the wrinkling of the liquid surface increase the surface roughness and consequently, the liquid area exposed to the heat transfer from the flame. A roughness correction parameter F_r is introduced to model this phenomenon. Gater and L'Ecuyer suggested an empirical formulation for the correction factor, that can

be expressed in terms of the operational motor parameters.

$$F_r = 1 + \frac{14.1\rho_g^{0.4}}{G^{0.8}\left(T_g/T_v\right)^{0.2}} \tag{3.2.31}$$

The experimental tests lead to observe an inverse proportionality between the surface roughness and the dynamic pressure of the gas flow. The linear theory, which shows decreasing wave length with increasing gas mass flux, confirms this phenomenon.

The classical regression rate is obtained as follows:

$$\dot{r}_{\mathrm{cl}} = \frac{0.03\mu_g^{0.2}}{\rho_s}\left(1 + \frac{\dot{Q}_r}{\dot{Q}_c}\right)BC_{B1}G^{0.8}z^{-0.2} \tag{3.2.32}$$

The total regression rate can be written as the sum of the classical regression rate that is generated by the vaporization of the fuel at the liquid surface and the entrainment regression rate due to the liquid droplet detachment from the surface.

$$\dot{r} = \dot{r}_v + \dot{r}_{\mathrm{ent}} \tag{3.2.33}$$

The contribution of the entrainment can be expressed as a function of the mass flux in the port, using the equation 3.2.27 developed in the previous section. The dependence on the thickness h is neglected, which is a good approximation for cases of large absorptivity in the liquid phase and acceptable for the other cases.

$$\dot{r}_{\mathrm{ent}} = a_{\mathrm{ent}}\frac{G^{2\alpha}}{\dot{r}^{\beta}} \tag{3.2.34}$$

The entrainment coefficient is mainly a function of the selected propellant.

$$a_{\mathrm{ent}} = K\frac{C_f a_t^{\beta}\rho_l}{\mu_l\rho_s} \tag{3.2.35}$$

In order to express a relation between $\dot{r}_v$ and $\dot{r}_{\mathrm{ent}}$, the energy balance at the liquid gas interface is introduced.

$$\dot{r}_v + \left[R_{\mathrm{he}} + R_{\mathrm{hv}}\left(\dot{r}_v/\dot{r}\right)\right]\dot{r}_{\mathrm{ent}} = F_r\frac{0.03\mu_g^{0.2}}{\rho_s}\left(1 + \dot{Q}_r/\dot{Q}_c\right)B\frac{C_f}{C_{fo}}G^{0.8}z^{-0.2} \tag{3.2.36}$$

The non-dimensional energy parameters for entrainment R_{he} and vaporization R_{hv} are introduced to take into account the different heating histories of the transferred mass through the two mechanisms.

$$R_{\text{hv}} = \frac{C_l(T_s - T_m)}{h_v}, \quad R_{\text{he}} = \frac{h_m}{h_v} \tag{3.2.37}$$

An assumption is made, that as the vaporization component of the regression rate decreases, the required effective heating for the liquid entrained material is reduced. In this way the asymptotic behavior of regression rate in the entrainment-dominated operations is captured.

A nonlinear set of algebraic equations is obtained considering equations 3.2.33, 3.2.34, and 3.2.36. These equations can be conveniently recast in non-dimensional, nonlinear form, by normalising for the classical regression rate 3.2.32.

$$\psi = \frac{\dot{r}}{\dot{r}_{\text{cl}}}, \quad \psi_v = \frac{\dot{r}_v}{\dot{r}_{\text{cl}}}, \quad \psi_{\text{ent}} = \frac{\dot{r}_{\text{ent}}}{\dot{r}_{\text{cl}}} \tag{3.2.38}$$

$$\begin{aligned} \psi &= \psi_v + \psi_{\text{ent}} \\ \psi_v + \left(R_{\text{he}} + R_{\text{hv}}\frac{\psi_v}{\psi} \right)\psi_{\text{ent}} &= \frac{Fr}{C_{B1}+C_{B2}\psi_v} \\ \psi_{\text{ent}} &= \frac{R_{\text{ent}}}{\psi^\beta} \end{aligned} \tag{3.2.39}$$

Where $R_{\text{ent}} = a_{\text{ent}}(G^{2\alpha})/(\dot{r}_{cl}^{\beta+1})$. The system 3.2.39 can be solved for given fuel and oxidiser to obtain the regression rate in the case of entrainment as a function of the axial location and local mass flux.

29

Chapter 4

Investigated paraffin-based formulations

4.1 Paraffin-based fuels

Among liquefying fuels, paraffin-based fuels exhibit the optimal properties of low viscosity and surface tensions, and they are at solid state at ambient temperature. These two characteristics allows them to have good regression rate, thanks to the entrained mass transfer, and avoid the difficulties in handling cryogenic propellants. The current study is then focused on the behaviour of paraffin fuel formulations, whose properties will be reported in this chapter.

4.1.1 General properties of paraffin

Paraffin wax is a colorless or white solid at room temperature, which is extracted from petroleum by removing the oil from raw products of oil refineries, containing mixture of oil and wax. It consists of a mixture of normal alkanes, that are a group of fully saturated, straight chain hydrocarbon, with general molecular structure $C_n H_{2n+2}$[22]. They form only $C-H$ and $C-C$ single bonds, resulting from overlap of sp^3 orbital of carbon with $1s$ orbital of hydrogen or adjacent sp^3 orbital of carbon atom. For paraffin waxes the number of carbon atoms range from 20 to 60 in most cases[8]. The physical and chemical properties of paraffin wax derives from the molecular structure of the alkane.

The melting point is between 47 to 65 °C (320 to 338 K), while the boiling point is above 370 °C (643 K)[2]. The temperatures for the phases transition are determined by the intermolecular Van der Waals forces that increase with the value of molecular weight[39]. For the carbon atoms range of paraffin wax, high boiling points are observed, which is a good quality for storage and handling of the propellant. Also, it has good thermal stability, and it is inherent. Having a high hydrogen to carbon atoms ratio, other optimal properties such as high heat of combustion and low smoke production and carbon deposits are reported.

The main characteristics are summarized in the following table.

Property	Symbol	Value
Melting temperature	T_m	$> 325\ K$
Vaporization temperature	T_v	$> 645\ K$
Heat of fusion	L_m	$200\text{x}10^3\ J/kg$
Solid Phase		
Density	ρ_s	$913\ kg/m^3$
Thermal conductivity	λ_s	$0.36\ W/m/K$
Specific heat	C_s	$2604\ J/kg/K$
Absorption coefficient	a_s	$1620\ 1/m$
Liquid Phase		
Density	ρ_l	$766\ kg/m^3$
Thermal conductivity	λ_l	$0.25\ W/m/K$
Specific heat	C_l	$2981\ J/kg/K$
Absorption coefficient	a_l	$860\ 1/m$
Surface tension	σ	$33\text{x}10^{-3}\ N/m$
Kinematic viscosity	ν	$10\text{x}10^{-6}\ m^2/s$

Table 4.1.1: General properties of paraffin wax

Classification of paraffin

Among the wax derived from petroleum, there is a major classification between macro-crystalline waxes (pure-paraffin waxes), and micro-crystalline waxes. The former has large, clearly defined crystalline structures and high proportion of normal carbon chains, while the latter has finer, irregular crystals and contains a higher percentage of branched hydrocarbons.

Micro-crystalline types have higher density, viscosity, and melting point (62 to 102 °C) than pure paraffin waxes. They are usually darker and opaque, while the macro-crystalline are white and translucent. The non-straight chain components confer elastic and adhesive characteristics, and the thin crystal structure leads to more flexibility[3]. Thus, micro-crystalline waxes are easily processable and have higher fracture toughness; this property increases the tolerance of surface or internal micro-cracks and other microstructural defects of increased radius, keeping constant at the same time the applied thermo-mechanical stress level during operations[46].

4.1.2   Sasol Wax formulations

The paraffin waxes considered in this analysis are manufactured by an integrated energy and chemical company Sasolwax GmbH. Both micro-crystalline and pure paraffin crystalline are analysed. Coatings manufactured with these waxes exhibit higher strength, and hence abrasion resistance as well as an improved gloss impression[27].

The main properties of the formulations without additives are reported. The congealing point is also reported, which is the temperature at which molten petroleum wax, when allowed to cool under prescribed conditions, ceases to flow[1]. Some of the parameters are given by the manufacturer. Where there is no reference for some properties, either from the manufacturer or from experimental research, the values for the general properties of paraffin wax are used as reference. Also, some scaling is possible by establishing a relation

between the properties and the molecular weight of the material, hence the carbon number n. Even if these paraffins are mixtures of alkane, it is a good estimation to evaluate the characteristics at an averaged carbon number[7]. Especially, viscosity,surface tension and density for the liquid phase need to be evaluated in function of temperature, since they characterize the transport properties for the numerical simulations. The asymptotic behavior correlations (ABCs) developed by Marano et al.[35] are employed to predict these terms, as suggested by Karabeyoglu et al. in the evaluation of materials properties for $n-$alkane[22]. The methods for ABCs is summarized by the following expressions and tables:

$$Y = Y_{\infty,0} + \Delta Y_\infty \left(n - n_0\right) - \Delta Y_0 \exp\left(-\hat{\beta}\left(n \pm n_0\right)^{\hat{\gamma}}\right) \qquad (4.1.1)$$

$$
\begin{aligned}
\Delta Y &= A + B/T + C\ln T + DT^2 + E/T^2, \ n - n_0 \text{ for } \ln\mu_l \\
\Delta Y \text{ or } Y &= A + BT + CT^2, \ n - n_0 \text{ for } \sigma \\
\Delta Y &= A + BT + CT^2 + DT^3, \ n + n_0 \text{ for } V_l
\end{aligned}
\qquad (4.1.2)
$$

	$\ln\mu_l \ (g/m/s)$		$\sigma \ (mN/m)$	
	ΔY_0	ΔY_∞	ΔY_0	$Y_{\infty,0}$
A	-602.688	0.0290196	627.213	73.8715
B	77866.8	-241.023	-0.882888	-0.177123
C	198.006	0.0440959	0.00268188	1.54517×10^{-4}
D	-4.18077×10^{-5}	-1.84891×10^{-7}	—	—
E	-2.49477×10^6	56561.7	—	—

Table 4.1.2: Temperature-dependent ABC parameters for liquid viscosity and surface tension

	$V_l \ (cm^3/g/mol)$	
	ΔY_0	ΔY_∞
A	8592.30	12.7924
B	-85.7292	0.0150627
C	0.280284	-1.30794×10^{-5}
D	-4.48451×10^{-4}	1.59611×10^{-8}
E	—	—

Table 4.1.3: Temperature-dependent ABC parameters for density

	$\ln\mu_l \ (g/m/s)$	$\sigma \ (mN/m)$	$V_l \ (cm^3/g/mol)$
n_0	-2.293981	0.264870	-1.388524
$Y_{\infty,0}$	57.8516	see Table 4.1.3	0
ΔY_∞	see Table 4.1.3	0	see Table 4.1.3
ΔY_0	see Table 4.1.3	see Table 4.1.3	see Table 4.1.3
$\hat{\beta}$	2.476409	2.511846	5.519846
$\hat{\gamma}$	0.0112117	0.201325	0.0570632

Table 4.1.4: ABC parameters for liquid viscosity and surface tension of $n-$Paraffins

The dynamic and kinemtic viscosity for the liquid layer are then obtained as $\mu_l = \exp(Y)$ and $\nu_l = \mu_l/\rho_l$, the surface tension as $\sigma = Y$, where Y is obtained accordingly to equation 4.1.1. The density is evaluated as the molecular weight over the liquid molar volume $V_l = Y$. The range of validity of this model has been tested for a range of carbon numbers of 3 to 94 and a range of temperatures of 0 to 300° C for viscosity and density; a range of carbon numbers 3 to 20 and a range of temperatures of 0 to 150° C for surface tension. Thus, a cross-reference with other experimental values from literature was performed. Figure show the results obtaines through a rheometer and a tensiometer by Kobald et al. with paraffin-based fuels[28]. Values of density for the paraffin have been obtained experimentally at the SPLab and reported in the master thesis of Garg[17], as $787.81 kg/m^3$ for Sasol 0907, $764.32 kg/m^3$ for Sasol 6805, $793.68 kg/m^3$ for Sasol 6003.

(a) Dynamic viscosity ($kg/m/s$)

(b) Surface tension (mN/m)
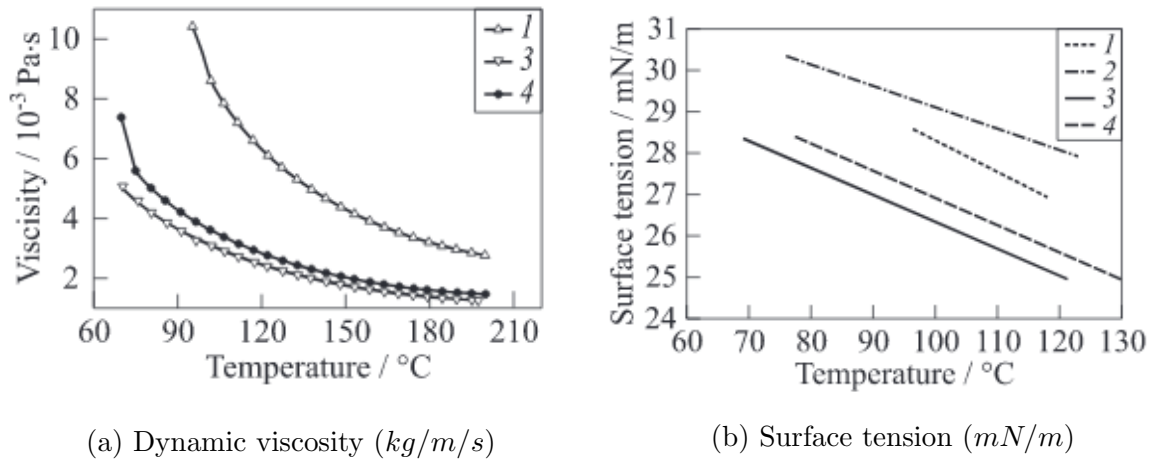
Figure 4.1.1: Properties in function of temperature of 1-Sasol wax 0907; 2-Sasol wax 1276; 3-Sasol wax 6003; 4-Sasol wax 6805[28]

Sasol Wax 6003(W3)

Sasol Wax 6003 is a macro-crystalline wax, thus it has more linear carbon chains than branched alkane. Its average chemical composition can be expressed as $C_{32}H_{66}$. The dynamic viscosity obtained with ABCs is in good relation with the experimental results reported in Figure 4.1.1a. The kinematic viscosity at the temperature of 150° C is reported in the table. On the other hand, the value for the surface tension with the correlations at $T = 100°$ C is 24.9 mN/m, lower than the one reported by Kobald. For the reasons explained in the previous section about the validity range of carbon numbers for ABCs, the results obtained with the tensometer are taken as reference, according to the linear trend shown in Figure 4.1.1b. The liquid density is in the range of the one obtained through the experiments; the advantage of the ABCs model is that a parametric variation with temperature can be obtained, which is useful for the simulation purposes.

Property	Symbol	Value
Melting temperature	T_m	333.15 K
Vaporization temperature	T_v	661.17 K
Congealing point	T_{cp}	$333 - 335\ K$
Heat of fusion	L_m	200x10^3 J/kg
Solid Phase		
Density	ρ_s	946 kg/m^3
Thermal conductivity	λ_s	0.326 $W/m/K$
Specific heat	C_s	2509.87 $J/kg/K$
Absorption coefficient	a_s	2000 $1/m$
Liquid Phase		
Density (at $T = 150°C$)	ρ_l	730.4 kg/m^3
Thermal conductivity	λ_l	0.160 $W/m/K$
Specific heat	C_l	2873.25 $J/kg/K$
Absorption coefficient	a_l	1000 $1/m$
Surface tension (at $T = 150°C$)	σ	23x10^{-3} N/m
Kinematic viscosity (at $T = 150°C$)	ν	2.41x10^{-6} m^2/s

Table 4.1.5: Main properties of Sasol Wax 6003

Sasol Wax 0907(W1)

Sasol Wax 0907 is a micro-crystalline wax with low oil content; it is composed by 36% linear alkanes and 64% branched alkanes. Its average chemical composition is $C_{50}H_{102}$. As in the previous case, the value obtained through asymptotic behaviour correlations for the viscosity is in good agreement with the experimental rheological results, while the surface tensions results to be a bit lower. Another reference for σ is given by Piscitelli et al.[46], employing the Owens-Wendt approach for surface free energy; the surface tension is predicted to follow the trend as in Figure 4.1.2. These results are similar to experimental ones obtained by Kobald.
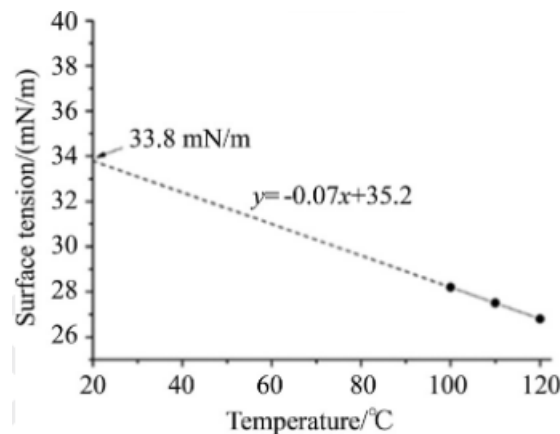

Figure 4.1.2: Surface tension as a function of the temperature for Sasol Wax 0907[46].

Property	Symbol	Value
Melting temperature	T_m	363.15 K
Vaporization temperature	T_v	720.71 K
Congealing point	T_{cp}	$356 - 367\ K$
Heat of fusion	L_m	200x10^3 J/kg
Solid Phase		
Density	ρ_s	939 kg/m^3
Thermal conductivity	λ_s	0.329 $W/m/K$
Specific heat	C_s	2529.84 $J/kg/K$
Absorption coefficient	a_s	1000 $1/m$
Liquid Phase		
Density (at $T = 150°C$)	ρ_l	748 kg/m^3
Thermal conductivity	λ_l	0.162 $W/m/K$
Specific heat	C_l	2896.10 $J/kg/K$
Absorption coefficient	a_l	500 $1/m$
Surface tension (at $T = 150°C$)	σ	24.7x10^{-3} N/m
Kinematic viscosity (at $T = 150°C$)	ν	5.57x10^{-6} m^2/s

Table 4.1.6: Main properties of Sasol Wax 0907

The density derived from ABCs model is acceptable also in this case. As it is predictable from its micro-crystalline nature, this wax has highest melting point and vaporization point among the other considered paraffins. Its surface tension and viscosity are also bigger than the other ones; thus, it can be predicted that the entrainment phenomenon will be of less importance than for Sasol Wax 6003 and 6805. On the other hand, as previously explained, micro-crystalline waxes such as Sasol Wax 0907 are more resilient in case of imperfect manufacturing process, like in the presence of micro-fractures or structural defects. This paraffin is then of interest despite the high viscosity and surface tension, since it could assure good structural properties with less need of additives, that would modify the entrainment anyway.

Sasol Wax 6805(W2)

Sasol Wax 6805 is a pure paraffin wax, which shows good mechanical properties. To derive its chemical formulation, the direct proportionality between viscosity and carbon atoms is considered. In this case the value for the kinematic viscosity given by the manufacturer is in the range $6 - 8mm^2/s$ at $T = 100°\ C$. The obtained average composition is $C_{40}H_{82}$; the carbon number, as well as the viscosity, is in-between the other two paraffin waxes[17]. Once n is determined, the ABCs correlations can be employed as for the other two paraffin waxes. Also in this case, the difference between the calculated surface tension and the experiments from Kobald is about 1 mN/m. Therefore, the negative linear trends with temperature is considered as in Figure 4.1.1b. The density and viscosity variation with temperature, predicted by the empirical correlations, are considered reliable.

This paraffin has the lowest density among the three, and the highest thermal conductivity and the specific heat, both in solid and liquid phase.

Property	Symbol	Value
Melting temperature	T_m	$343.15\ K$
Vaporization temperature	T_v	$681.02\ K$
Congealing point	T_{cp}	$339 - 343\ K$
Heat of fusion	L_m	$200\text{x}10^3\ J/kg$
Solid Phase		
Density	ρ_s	$911\ kg/m^3$
Thermal conductivity	λ_s	$0.339\ W/m/K$
Specific heat	C_s	$2609.70\ J/kg/K$
Absorption coefficient	a_s	$1600\ 1/m$
Liquid Phase		
Density (at $T = 150°C$)	ρ_l	$740.3\ kg/m^3$
Thermal conductivity	λ_l	$0.167\ W/m/K$
Specific heat	C_l	$2987.53\ J/kg/K$
Absorption coefficient	a_l	$800\ 1/m$
Surface tension (at $T = 150°C$)	σ	$23.58\text{x}10^{-3}\ N/m$
Kinematic viscosity (at $T = 150°C$)	ν	$3.63\text{x}10^{-6}\ m^2/s$

Table 4.1.7: Main properties of Sasol Wax 6805

Properties variation with temperature

From the cross references analysed before, it is possible to state that the ABCs model gives a good estimation of the density and viscosity variation with temperature. Thus, the correlations are implemented in Matlab and the trend are plotted as in the following figures.
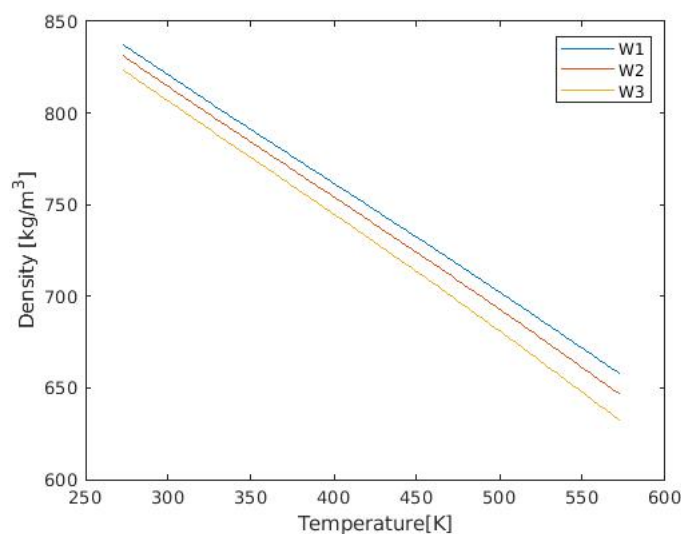
Figure 4.1.3: Density for W1,W2,W3 obtained with ABCs
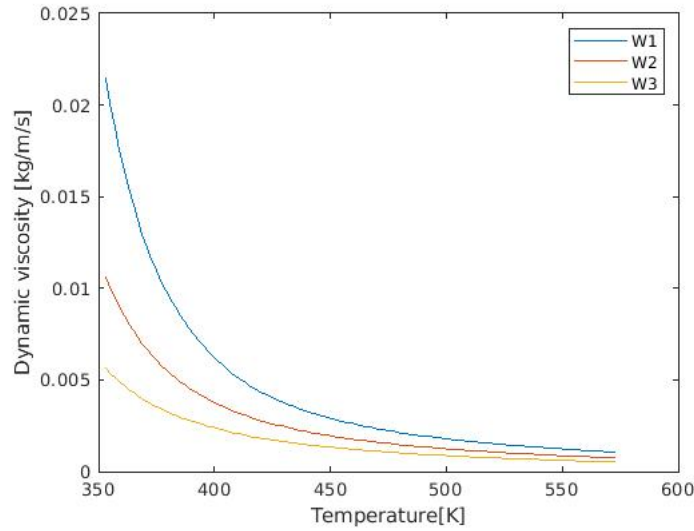
Figure 4.1.4: Dynamic viscosity for W1,W2,W3 obtained with ABCs.
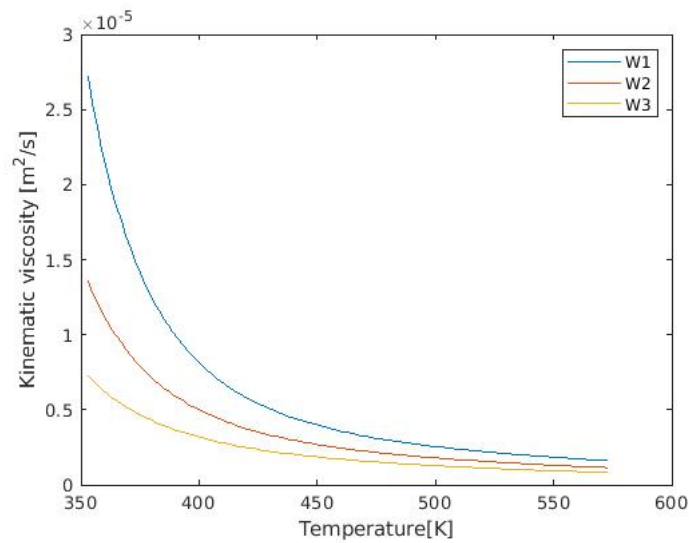
Figure 4.1.5: Kinematic viscosity for W1,W2,W3 obtained as μ/ρ for ABCs

On the other hand, the surface tension predicted by Marano et al.[35] are generally lower than the experimental values obtained by Kobald and Piscitelli. Thus, these last results are considered to set a law for σ in function of temperature. Both cases report a linear trend, with inverse proportionality to temperature. Choosing two different values, the equation for the straight line is defined; again, it is implemented in Matlab and the graph is obtained as in Figure 4.1.6.
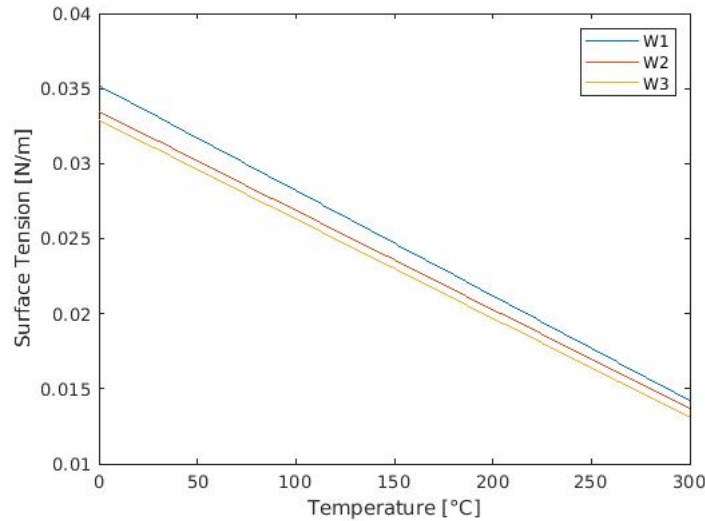
Figure 4.1.6: Surface tension for W1,W2,W3 obtained from Kobald[28]'s data

4.1.3   Additives

In order to improve the performance of the paraffin-based fuels controlled amount of other substances, mechanically or energetically enhancing, can be added.

Besides the enhancement of regression rate due to the entrainment, the performance of hybrid engines can be improved by loading the solid fuel with energetic additives such as metal powders and hydrides. Metal additives increase both the flame temperature, hence the heat transfer to the fuel, and the density of the propellant. The most common is aluminium, thanks to its non-toxic and inexpensive characteristics. Also, the presence of agglomerates in molten state of aluminum oxide in the combustion chamber is beneficial to dampen out the combustion instabilities caused by acoustic waves. In case of entrainment, paraffin droplets containing Aluminum particles ignite more easily and more complete combustion happens at the detachment location.

Another additive often used to control the radiative properties of the fuel salab is carbon black. By preventing thermal penetration into the bulk fuel, the mechanical strength of the solid part is preserved[45]. It also increases the radiative heat transfer from the flame.

The predominant additive for paraffin matrix reinforcement is the styrene-ethylene-butylene-styrene (SEBS), because of its chemical compatibility and miscibility with alkanes. It is a thermoplastic elastomer, which exhibits balanced elasticity and processibility, and good thermal stability[30]. The styrene-blocks at the extremes of the SEBS macromolecule provide the thermoplastic behavior to the material[45]. The aim of this additive is to increase the paraffin elasticity without highly affecting the regression rate value and ensuring isotropic mechanical properties[16]. It avoids the formation of critical defects due to the volumetric shrinkage during the cooling of the melted paraffin, thus, the structural integrity of the fuel grain is kept. The higher melting point, decomposition temperature and viscosity of SEBS may have a negative effect on the regression rate, according to the liquefying hybrid theory of Karabeyoglu et al.[23].

Properties of formulations with SEBS additives

In previous work by Garg[17], the thermophysical properties of 6 paraffin waxes with addition of SEBS are evaluated. One formulation is with Sasol Wax 6003, the others with the micro-crystalline wax Sasol Wax 0907. The nomenclature for these compounds is SXWY, where X is the mass fraction of the additive and WY stands for the previous discussed paraffins, being Sasol Wax 0907 W1, Sasol Wax 6805 W2, Sasol Wax 6003 W2. The reinforcing polymer mass fractions range from 5% to 40%.

It is assumed that the addition of SEBS has a negligible effect on phase transition, absorption coefficient and surface tension. The liquid density has been obtained experimentally at SPLab. The properties of these new formulations are enlisted in the following table.

Property	S5W1	S7.5W1	S15W1	S20W1	S40W1	S5W3
SEBS mass fraction	5%	7.5%	15%	20%	40%	5%
$T_m\ [K]$	363.15	363.15	363.15	363.15	363.15	333.15
$T_v\ [K]$	720.71	720.71	720.71	720.71	720.71	661.17
Solid Phase						
$\rho_s\ [kg/m^3]$	938	928	929	931	914	932
$\lambda_s\ [W/m/K]$	0.342	0.3485	0.37	0.382	0.444	0.3395
$C_s\ [J/kg/K]$	2472.1	2443.30	2356.76	2299.07	2068.30	2453.18
$a_s\ [1/m]$	500	500	500	500	500	1000
Liquid Phase						
$\rho_l\ [kg/m^3]$	786.97	778.58	779.42	781.10	766.83	781.94
$\lambda_l\ [W/m/K]$	0.1718	0.1766	0.1923	0.205	0.255	0.1705
$C_l\ [J/kg/K]$	2846.3	2821.40	2746.69	2696.88	2497.66	2824.59
$a_l\ [1/m]$	1000	1000	1000	1000	1000	2000
$\sigma\ [N/m]$	$24.7\mathrm{x}10^{-3}$	$24.7\mathrm{x}10^{-3}$	$24.7\mathrm{x}10^{-3}$	$24.7\mathrm{x}10^{-3}$	$24.7\mathrm{x}10^{-3}$	$23\mathrm{x}10^{-3}$
$\nu\ [m^2/s]\ (T{=}150°C)$	$1.78\mathrm{x}10^{-5}$	$4.23\mathrm{x}10^{-5}$	$7.18\mathrm{x}10^{-5}$	$1\mathrm{x}10^{-4}$	$3.63\mathrm{x}10^{-3}$	$5.12\mathrm{x}10^{-6}$

Table 4.1.8: Main properties of paraffin with SEBS additives

The rheological behavior characterization of Sasol Wax with SEBS has been performed by Paravan et al.[45] The rheological investigation has been performed in a plate-plate configuration, over the shear rate range $10\text{-}1000 s^{-1}$, with furnace temperature of 150°C. The insurgence of shear thinning behaviors possibly encountered for S20W1 and S40W1 due to the non-complete fusion of the tested specimen lead to difficulty in the determination of the viscosity. The value for S20W1 is taken considering the trend of increasing viscosity with SEBS mass fraction. The main drawback of SEBS is indeed the high melt layer viscosity with respect to pure paraffin and micro-crystalline paraffin.The chemical formula for SEBS is $C_8H_8 \cdot C_4H_6 = C_{12}H_{14}$[4].

4.2   Oxidisers

The majorly tested oxidisers with paraffin-based fuels are oxygen, HTP, and nitrous oxide. For the current study, oxygen has been considered.

4.2.1 Oxygen

Oxygen, O_2, is commonly used because of its large availability; the main issues regards the cryogenic conditions for LOX and the low density for the GOX.

In the simulations the oxidiser is considered already flowing through the port in gaseous phase. Oxygen can be modeled as an ideal gas, therefore the transport properties are obtained using the properties of the ideal gas. A script is written in Matlab to evaluate the variation of density and viscosity with temperature. The results are reported in the following graphs.
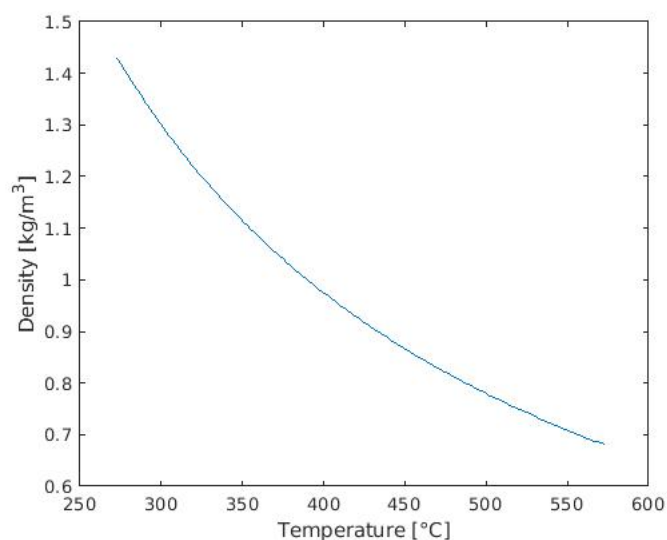

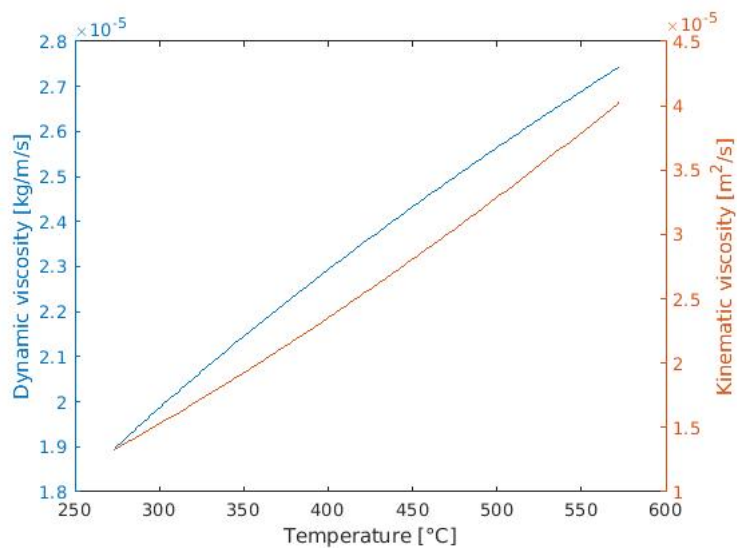Figure 4.2.1: Density of molecular oxygen from ideal gas law

Figure 4.2.2: Viscosity of molecular oxygen from ideal gas properties

Chapter 5

Numerical simulation of the entrainment

The numerical simulation is performed with OpenFOAM; the work of Knol and Maicke[25] is taken as reference, in continuation with the master thesis of Bernigaud[6].

5.1 Computational model for the interface with VOF

There are two main computational methods for two-phase flows: Eulerian and Lagrangian. The former attributes varying properties across the cells and performs the calculation for the entire flow; the latter tracks the individual particles with the corresponding properties. For the Volume Of Fluid method, the Eulerian approach is employed through an indicator function, that indicates the phase present in a cell. This is defined as:

$$\alpha_{\text{phase1}} = \begin{cases} 0 & \text{In phase 2} \\ 0 < \alpha_{\text{phase1}} < 1 & \text{At the interface} \\ 1 & \text{In phase 1} \end{cases} \tag{5.1.1}$$

In the folder `constant/transportProperties`, the transport properties μ, ρ and σ for phase1 and phase 2 are defined. At the interface location these parameters are evaluated considering the value of α_{phase1} as follows:

$$\begin{cases} \rho = \alpha_{\text{phase1}}\rho_{\text{phase1}} + (1 - \alpha_{\text{phase1}})\rho_{\text{phase2}} \\ \mu = \alpha_{\text{phase1}}\mu_{\text{phase1}} + (1 - \alpha_{\text{phase1}})\mu_{\text{phase2}} \end{cases} \tag{5.1.2}$$

The issue with this approach is the presence of a phase gradient, due to the continuous nature of the indicator function; the cells containing volume fractions of both phases will be filled with a uniform mixture of the two phases. This causes a not physical smearing of the interface, that can be limited only with very fine meshing or with specific algorithms that help determining where the cells are cut by the surface. These schemes are described by Olsson in reference [43].

5.1.1   interFoam

To overcome this issue the solver `interFoam` has been introduced by OpenCFD
to sharpen the interface for cases of two incompressible, isothermal immiscible fluids
phase-fraction based. The solver uses the numerical scheme Multidimensional Universal
Limiter for Explicit Solution (*MULES*), which consists in a modification of the convective
term for the following transport equation of the indicator function.

$$\frac{\partial \alpha_{\text{phase1}}}{\partial t} + \nabla \cdot (\alpha_{\text{phase1}} \mathbf{u}) = 0 \tag{5.1.3}$$

This rewritten in integral form for each cell becomes:

$$\int_{\Omega_i} \frac{\partial \alpha_{\text{phase1}}}{\partial t} dV + \int_{\partial \Omega_i} \alpha_{\text{phase1}} \mathbf{u} \cdot \mathbf{n} dS = 0 \tag{5.1.4}$$

The discretization of the equation is then performed, using any time scheme for the
first term, the Euler implicit in this case, and writing the second term as a sum over each
face of the cell.

$$\frac{\alpha_i(t + \Delta t) - \alpha_i(t)}{\Delta t} = -\frac{1}{|\Omega_i|} \sum_{f \in \partial \Omega_i} (F_u + \lambda_M F_c)^n \tag{5.1.5}$$

The term F_u is the advective flux, using an upwind scheme. The term F_c is represented
by an higher order scheme for the advection and a compressive flux term. This gives a
more accurate advection at the surface and reduces the smearing. The delimiter λ_M
is equal to 1 at the interface location and to 0 for the rest of the domain, thus, the
computational effort is reduced away from the surface. The expressions for the advective
fluxes are as follows:

$$F_u = \Phi_f \alpha_f \tag{5.1.6}$$

$$F_c = \Phi_f \alpha_f + \Phi_{rf} \alpha_{rf}(1 - \alpha)_{rf} - F_u \tag{5.1.7}$$

$$\Phi_{rf} = \min \left(C_\alpha \frac{|\Phi_f|}{|\mathbf{S_f}|}, \max \left[\frac{|\Phi_f|}{|\mathbf{S_f}|} \right] \right) (\mathbf{n_f} \cdot \mathbf{S_f}) \tag{5.1.8}$$

$$\alpha_{rf} = \alpha_P + \frac{\alpha_N - \alpha_P}{2} [1 - \chi (\Phi_f) (1 - \lambda_{\alpha r})] \tag{5.1.9}$$

$\mathbf{S_f}$ is the cell face area vector, and $\mathbf{n_f}$ the face centered interface normal vector. C_α is
specified by the user in the file `fvSolution`. N and P denotes the upwind and downwind
neighbour respectively, $\lambda_{\alpha r}$ is a limiter, and χ is a step function taking the value 1 where
volumetric face flux Φ_f is positive and -1 where it is negative.

5.1.2 interIsoFoam

With OpenFoam v1706 the variant `interIsoFoam` has been introduced, which uses *IsoAdvector* algorithm. Tests have shown that the method generally offers more accurate interface advection and a sharper interface representation than the previously existing *MULES* method. The novelty of the new scheme consists of two parts: the use of isosurface concept for modelling the interface inside cells in a geometric surface reconstruction step; the model of the motion for the face-interface intersection line to obtain the time evolution within a time step of the submerged face area. Integrating this submerged area over the time step leads to an accurate estimate for the total volume of fluid transported across the face[48]. The values for the phase fraction in a cell at a specific time is calculated from a function $H(x, t)$ describing the continuous phase fraction field.

$$H(\mathbf{x}, t) \equiv \frac{\rho(\mathbf{x}, t) - \rho_{\text{phase2}}}{\rho_{\text{phase1}} - \rho_{\text{phase2}}} \tag{5.1.10}$$

$$\alpha_i = \frac{1}{V_i} \int_{\Omega_i} H(\mathbf{x}, t) dV \tag{5.1.11}$$

To calculate the phase fractions at the next time step, the following equation is used, where the flux of α over each cell face is integrated in time and added together.

$$\alpha_i(t + \Delta t) = \alpha_i(t) - \frac{1}{V_i} \sum_{j \in B_i} s_{ij} \int_t^{t+\Delta t} \int_{F_j} H(\mathbf{x}, \tau) \mathbf{u}(\mathbf{x}, \tau) d\mathbf{S} d\tau \tag{5.1.12}$$

B_i is the list of all faces F_j belonging to cell i, s_{ij} is either $+1$ or -1 to ensure that the orientation of the flux is going out from the cell. The integrals inside the sum describe the total volume of fluid transported across F_j during one time step.

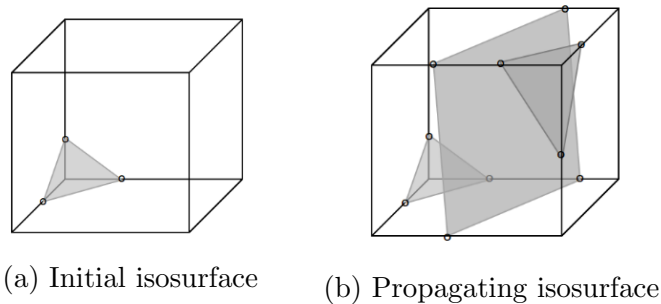(a) Initial isosurface   (b) Propagating isosurface

Figure 5.1.1: Isosurface in a hexahedral cell where one corner is submerged in the tracked phase; the edges are cut in circles location in figure[43]

5.2 Two-Phase flow simulation

Initially, the case studied by Bernigaud[6] is considered. The geometry of the domain is a rectangle, with the dimension adapted to simulate the test chamber for entrainment

visualization present at SPLab; the model is reported in Figure 5.2.1. For sake of simplicity a 2D case is analysed. This is also compatible with the images obtained with the experimental set-up. These simulations account for a non-reactive case, with the sole scope of investigating the liquid layer instabilities and the main factors affecting the entrainment phenomenon.
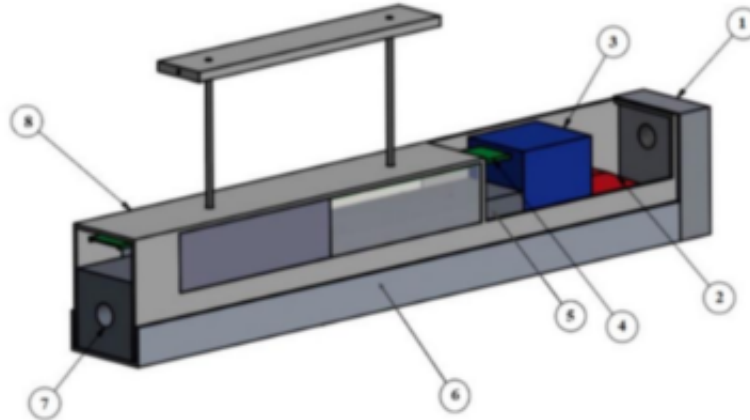
Figure 5.2.1: Test chamber for entrainment visualization: (1) oxidizer flow injector, (2) converging section (flow acceleration), (3) honeycomb for flow stabilization, (4) melted paraffin cover, (5) sample-holder, (6) external case, (7) heater housing, (8) windowed case [44]

5.2.1   Plane interface

The initial condition for the location of the two phases is assessed with the dictionary `setFieldsDict` in the `System` folder. This dictionary allows the user to set the default value for α_{phase1} in the domain, and to identify one or more regions where its value is different. Not only the indicator function, but also all the other calculated fields, like velocity and pressure, can be set initially on a selected set of cells. The options for the definition of the regions are those of `topoSetDict`; in this case the option `boxToCell` is used to select all cells whose cell centre is inside a given bounding box of height $h = 2mm$. Once the mesh is defined, the command *setFields* is run, and the resulting domain at $t = 0$ is visualized with ParaView as in Figure 5.2.2. The red part corresponds to parffin wax, that is $\alpha_{\mathrm{paraffin}} = 1$, the blue to the oxidiser, in this case air. The same would apply for all the other simulation of the entrainment. The cells at the interface have a value of $\alpha_{\mathrm{paraffin}}$ between 0 and 1.

The experiment conducted by Paravan et al. in reference [44] considers a u_{inlet} ranging from $25m/s$ to $50m/s$. Thus an inlet velocity of $35m/s$ is used in the following simulations. The chamber is taken at ambient pressure, with $P_0 = 10^5 Pa$. A hexaedral mesh with cubes of side $50\mu m$ is used for all simulations of entrainment visualization. The condition for the Courant number lower than unity is imposed, and the time step is adjusted accordingly.
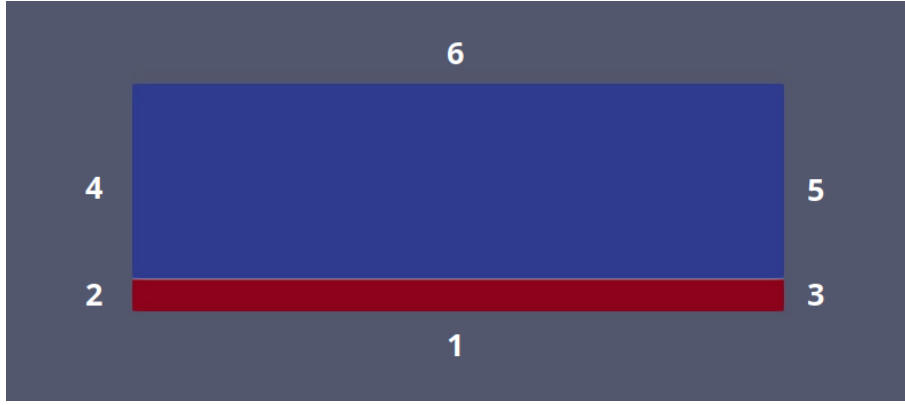
Figure 5.2.2: Domain for plane interface

The imposed boundary conditions on the domain are summarized in Table 5.2.1. On the front and back of the geometry, the *empty* condition is imposed to have a two-dimensional case. The *noSlip* condition is imposed at the walls.

Variable	Bottom wall(1)	Side walls (2−3)	Inlet(4)	Outlet(5)	Top boundary(6)
u	0	0	u_{inlet}	$\nabla \cdot u = 0$	$\nabla \cdot u = 0$
P	$\nabla \cdot P = 0$	$\nabla \cdot P = 0$	P_0	P_0	P_0
k	$\nabla \cdot k = 0$	$\nabla \cdot k = 0$	k_0	$\nabla \cdot k = 0$	$\nabla \cdot k = 0$
ε	$\nabla \cdot \varepsilon = 0$	$\nabla \cdot \varepsilon = 0$	ε_0	$\nabla \cdot \varepsilon = 0$	$\nabla \cdot \varepsilon = 0$
α_{paraffin}	1	$\nabla \cdot \alpha = 0$	0	$\nabla \cdot \alpha = 0$	$\nabla \cdot \alpha = 0$

Table 5.2.1: Boundary conditions

A $k - \varepsilon$ turbulence model is employed; for the initial guess classical correlations are imposed as following, where C_μ is 0.09 and $L*$ is the characteristic length for the inlet.

$$\begin{cases} I = 0.16 Re^{-1/8} \\ l = 0.07 L^* \\ k_0 = \frac{3}{2}(u_g I)^2 \\ \varepsilon_0 = C_\mu^{3/4} \frac{k_0^{3/2}}{l} \end{cases} \tag{5.2.1}$$

The treated paraffin is W1 and the gaseous phase is air, with the paraffin in liquid phase and the air considered at ambient temperature; the data for transport properties are the following, as reported by Bernigaud[6].

Property	W1	Air
$\rho [kg/m^3]$	654.4	1.28
$\nu [m^2/s]$	7.64x10^{-6}	1.45x10^{-5}
$\sigma [N/m]$	7.1x10^{-3}	−

Table 5.2.2: Transport properties for W1 and air at ambient temperature

(a) $t = 2ms$ (b) $t = 4ms$

(c) $t = 6ms$ (d) $t = 8ms$

(e) $t = 10ms$ (f) $t = 12ms$

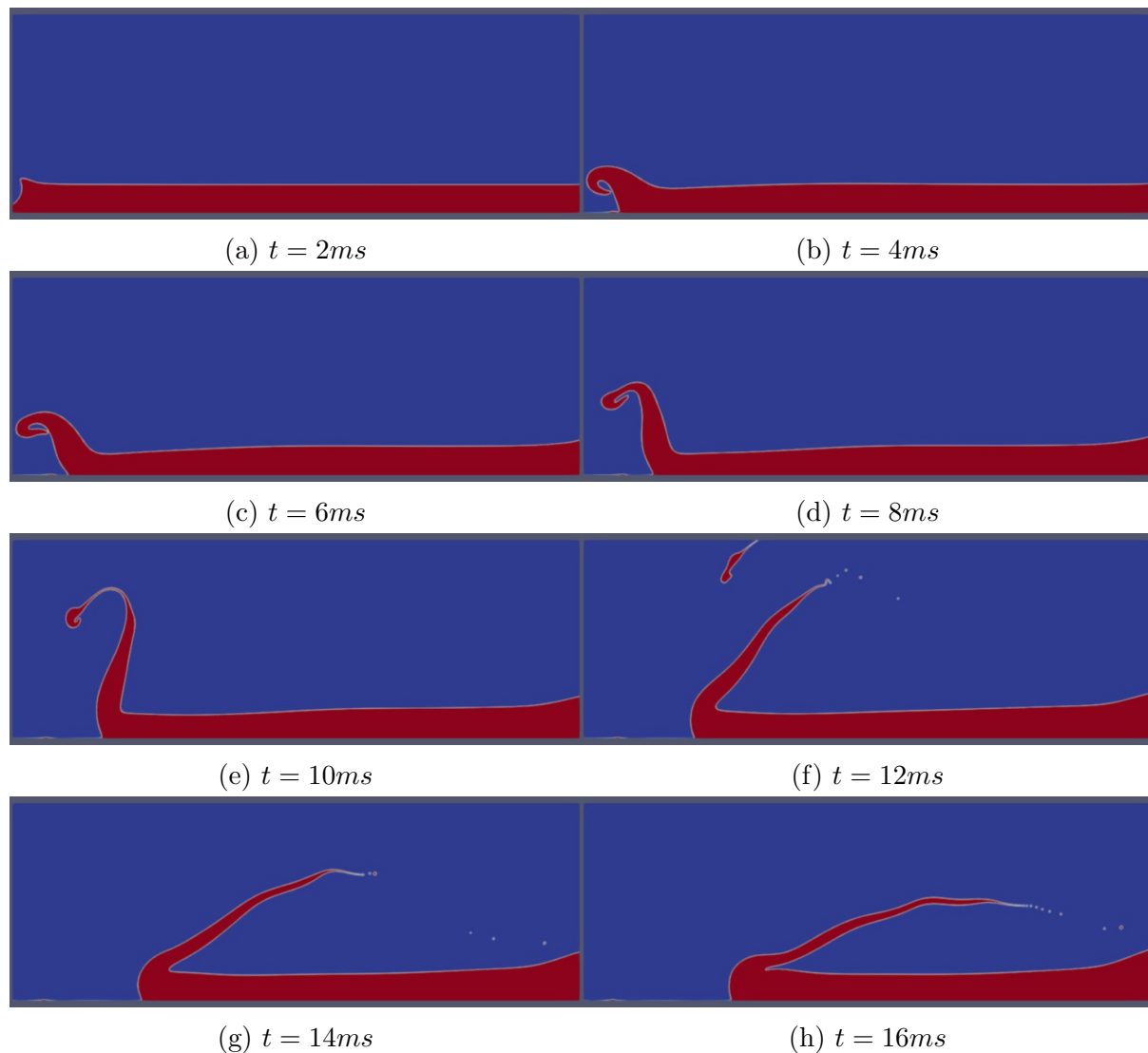(g) $t = 14ms$ (h) $t = 16ms$

Figure 5.2.3: Entrainment of liquid W1 in gaseous air at ambient temperature

The simulation successfully allows for the visualization of the phenomenon. A rolling wave is generated and then stretched by the passage of the air flow. The primary breakup takes place at the tip of the wave and the time of the event is recorded in the order of $10ms$, exactly between $10.4ms$ and $10.6ms$. The following figure shows the moment when the primary break-up is generated.

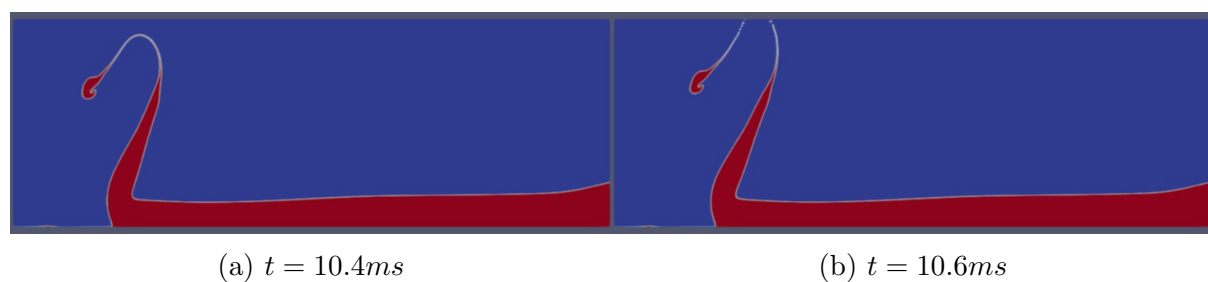(a) $t = 10.4ms$ (b) $t = 10.6ms$

Figure 5.2.4: Primary break-up for liquid W1 and gaseous air at ambient temperature

The droplet size distribution is in good agreement with experimental observations, as well as the dependence on the melt layer viscosity and the dynamic pressure of the gas phase, according to the results processed by Bernigaud. Thus, the numerical simulation can be a potential tool to compare the behaviour of the paraffins described in the previous chapter. Referring to the master thesis of Locca[32], the temperature for the transport properties is taken at $150°C$. This is a realistic condition considering the range of temperature for liquid paraffin. Also, for the oxidiser the gaseous oxygen is selected. The properties are reported in Table 5.2.3, following the model obtained from empirical correlations and the law of perfect gas for the oxidiser.

Property	W1	GOX
$\rho[kg/m^3]$	748	0.911
$\nu[m^2/s]$	$5.57\text{x}10^{-6}$	$26.65\text{x}10^{-6}$
$\sigma[N/m]$	$24.7\text{x}10^{-3}$	−

Table 5.2.3: Transport properties for W1 and GOX at $T = 423K$

(a) $t = 2ms$ (b) $t = 6ms$

(c) $t = 10ms$ (d) $t = 14ms$

(e) $t = 18ms$ (f) $t = 22ms$
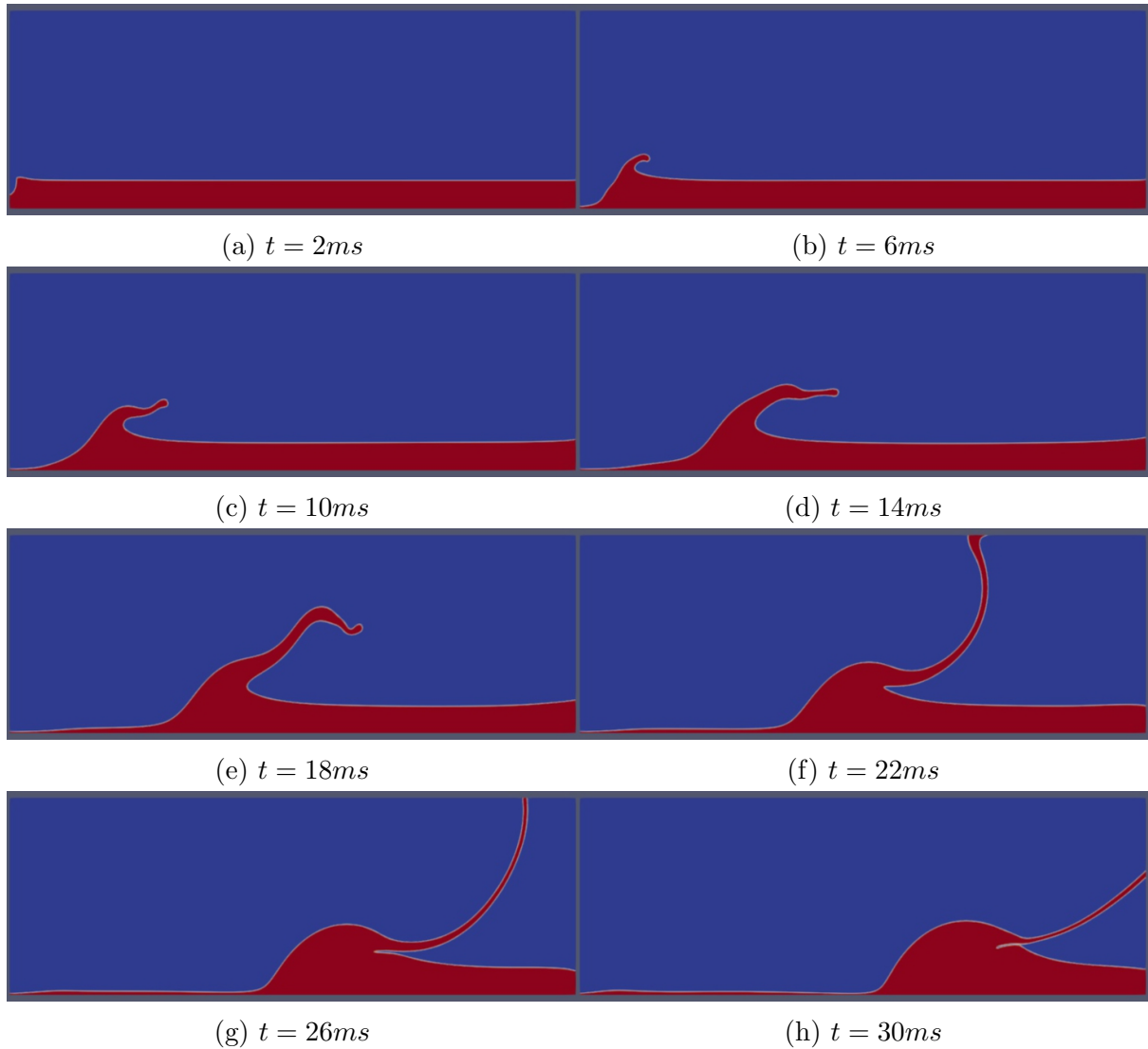
(g) $t = 26ms$ (h) $t = 30ms$

Figure 5.2.5: Entrainment of liquid W1 in gaseous oxygen at $T = 423K$

The Figure 5.2.5 shows the results for this set-up. Contrary to the previous case no entrainment is visualized within the chamber, even if the simulated time is longer of $10ms$. A rolling wave is generated, and stretched, showing the origination of instabilities under the effect of strong shear forces of the gas phase; no primary breakup happens, though. The reason can be found in the higher value of the surface tension, which is an order of magnitude larger than the one used in the first case. This directly influence the entrainment onset as described by equation 3.2.22. In the simulated time and in the confined geometry of the numerical study the onset with the actual surface tension value for paraffin is not verified.

5.2.2 Wave Interface

A major factor to investigate may be the geometry of the initial interface. As it can be observed in Figure 5.2.6, experimental evidence underlines the presence of waves typical of Kelvin-Helmoltz instabilities.

Figure 5.2.6: Instability of the liquid melt layer[32]

For this reason, a wave interface is imposed around the melt layer thickness of $h_{mean} = 2mm$, with equation 5.2.2. The plane wave `.stl` geometry is created and put in the simulation folder. The file `setFieldsDict` is modified, using the option `surfaceToCell` to select the cells inside the dictated geometry. The initial configuration is reported in Figure 5.2.7.
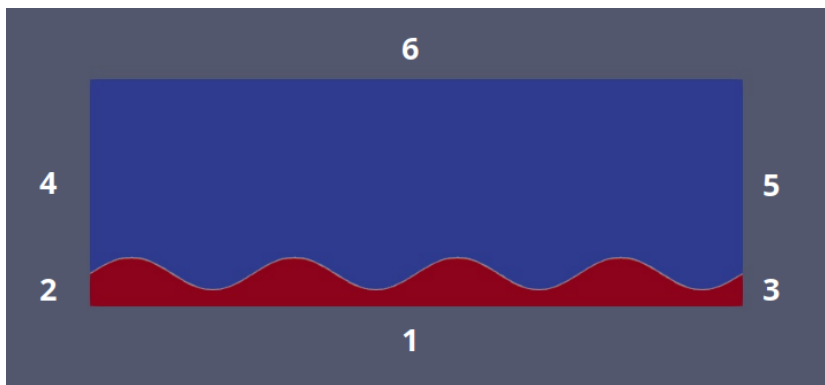
$$h = h_{mean} + A\sin(k_n z) \tag{5.2.2}$$

Figure 5.2.7: Domain for wave interface

The boundary conditions are the same as defined in Table 5.2.1 and the transport properties of the fluids are those in Table 5.2.3. The results of this simulation are reported in the following figure.

(a) $t = 2ms$ (b) $t = 6ms$

(c) $t = 10ms$ (d) $t = 14ms$

(e) $t = 18ms$ (f) $t = 22ms$

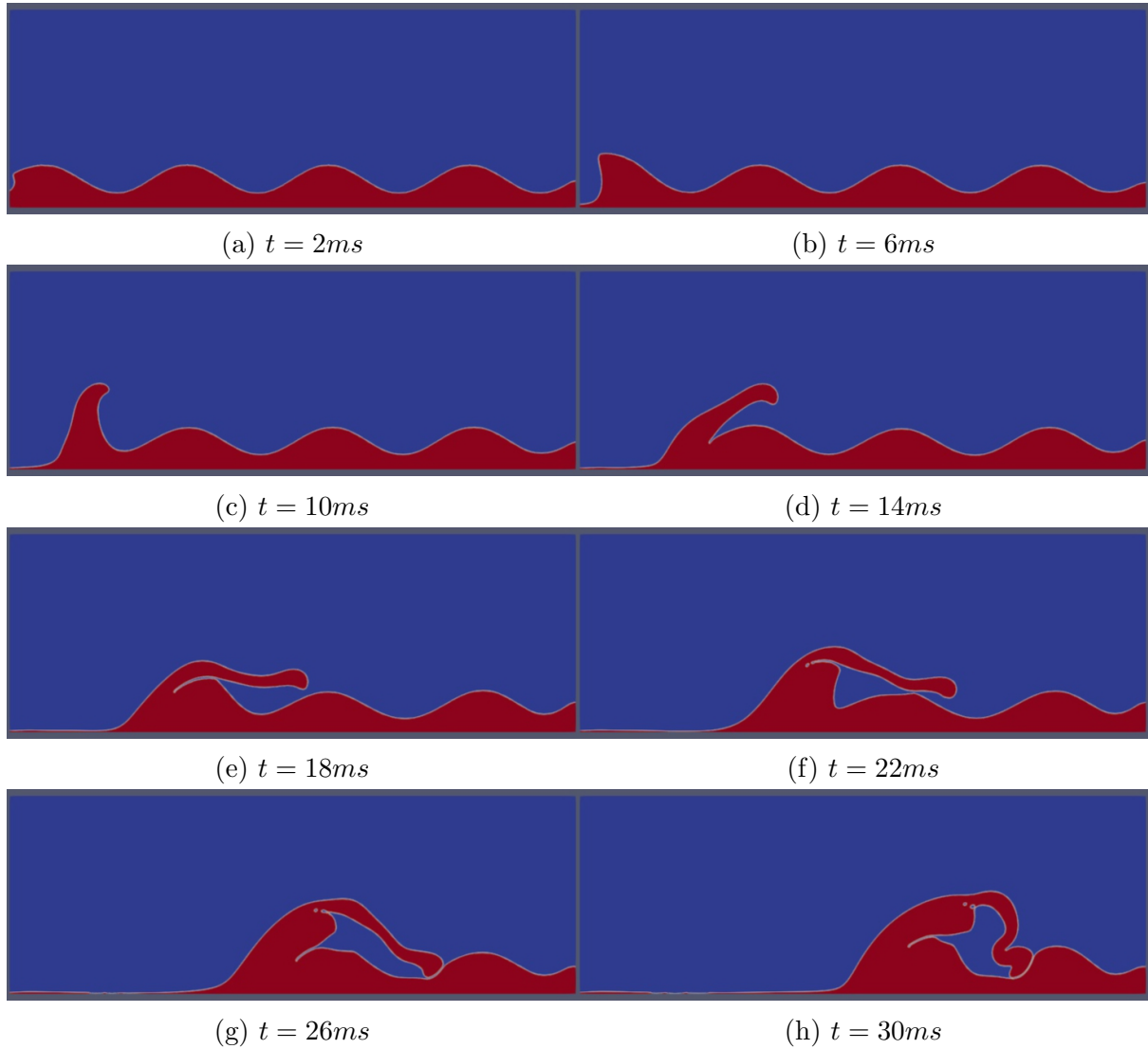(g) $t = 26ms$ (h) $t = 30ms$

Figure 5.2.8: Entrainment of liquid W1 in gaseous oxygen at $T = 423K$, with wave interface

Also in this case no droplet detachment is recorded. The limitation of this model are to be found in the dimension of the domain, that could be unable to capture entrainment phenomenon if this verifies more downstream. In Figure 5.2.8 it is possible to observe that only the first wave crest is disturbed by the gas flow and causes the deformation of the interface by impacting on the others, while the experiments show a deformation of all the wave crests. Thus, another issue can be related to the $k - \varepsilon$ model. In Figure 5.2.9 the velocity field at the last time step of the simulation is shown; the gas flow impact on the first wave and does reach the outlet only toward the end of the simulation. The reason behind this behaviour can be in the high values of the turbulence parameters for k_0 and ε_0 that result from the high Reynolds number in a chamber with inlet of the order of mm.
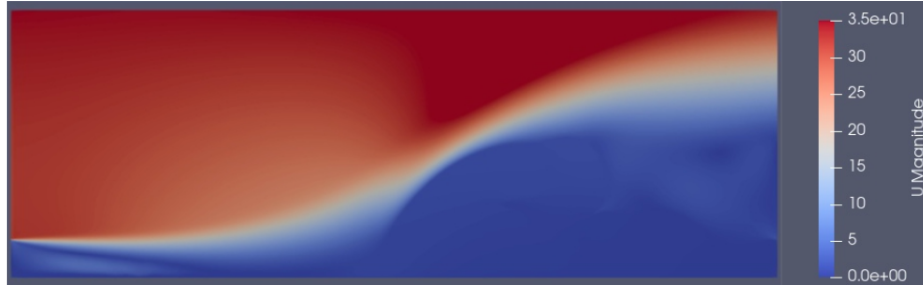
Figure 5.2.9: Velocity field at $t = 30ms$

5.2.3 Cyclic boundary condition

Since the focus is on the comparison of different paraffin formulations, the difficulties in the model limitations are overcome by introducing cyclic boundary conditions on the sides. This patch type allows two boundary regions to be treated as if they are physically connected. The presence of the inlet and outlet is removed, with the velocity initialized in the whole oxidiser region through `setFieldsDict`. The boundary conditions are defined as follows, with *noSlip* condition only at the bottom wall. The simulation is performed as DNS, since the visualization of the droplets requires a very fine mesh to be used anyway.
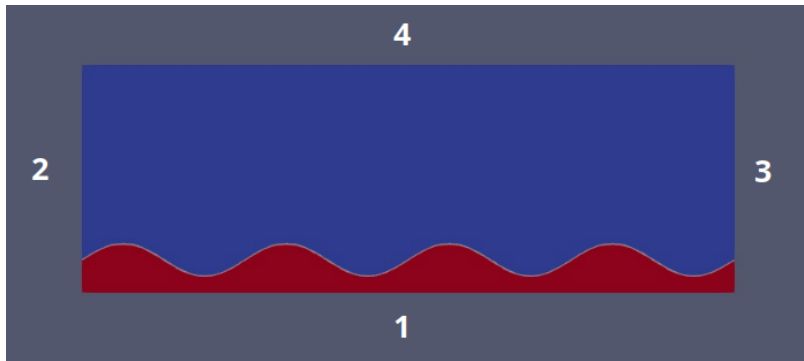
Figure 5.2.10: Domain for cyclic BC

Variable	Bottom wall	Top boundary	Left boundary	Right boundary
u	$u = 0$	$\nabla \cdot u = 0$	cyclic	cyclic
P	$\nabla \cdot P = 0$	$P = 10^5 \mathrm{Pa}$	cyclic	cyclic
$\alpha_{\mathrm{paraffin}}$	$\alpha = 1$	$\nabla \cdot \alpha = 0$	cyclic	cyclic

Table 5.2.4: Boundary conditions

W1+GOX

The properties for this case are the same described in table 5.2.3.

(a) $t = 2ms$ (b) $t = 6ms$

(c) $t = 10ms$ (d) $t = 14ms$

(e) $t = 18ms$ (f) $t = 22ms$

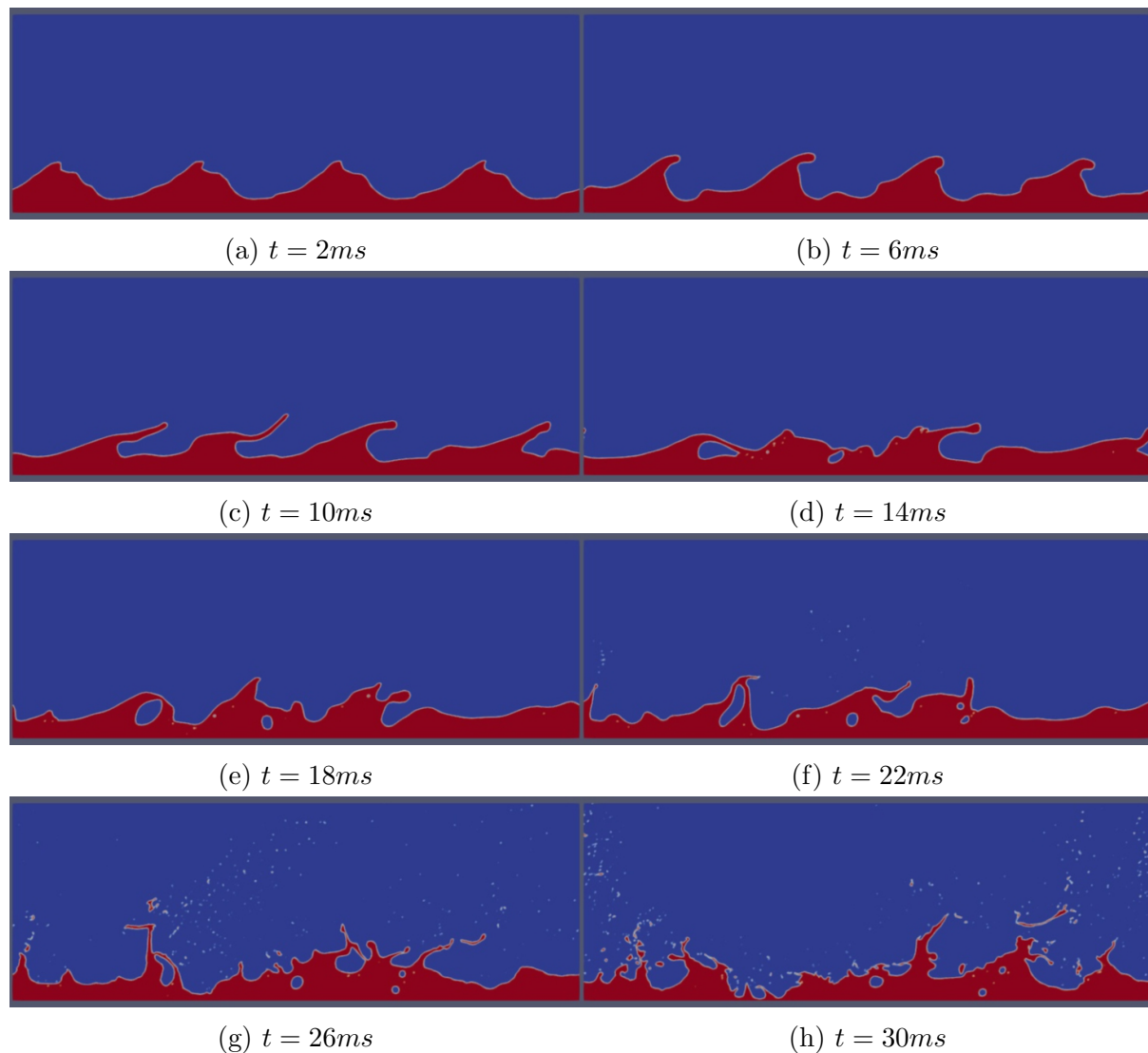(g) $t = 26ms$ (h) $t = 30ms$

Figure 5.2.11: Entrainment of liquid W1 in gaseous oxygen at $T = 423K$, with cyclic BC

As the simulation is started, the instabilities are amplified and the peaks are elongated, until some droplets are detached from the crests. By the end of the simulation it is quite difficult to visualize the initial wave form, with several features merged together and large amount of liquid paraffin entrained into the mean flow.
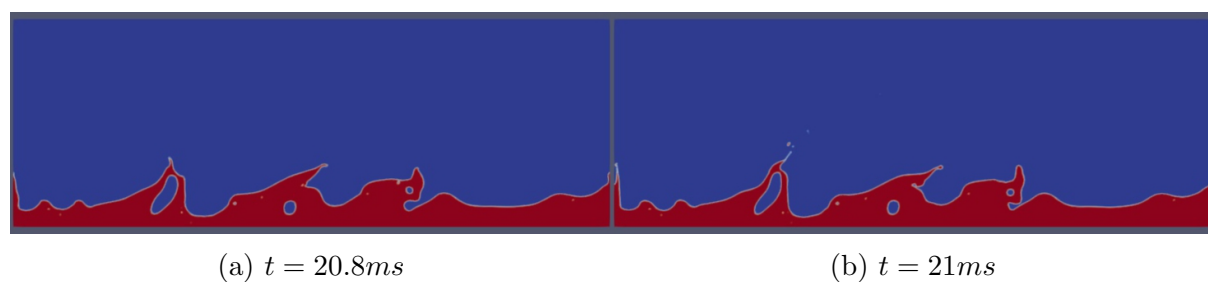

(a) $t = 20.8ms$ (b) $t = 21ms$

Figure 5.2.12: Primary break-up for liquid W1 and gaseous oxygen at $T = 423K$

The primary breakup happens between $t = 20.8ms$ and $t = 21ms$.

W2+GOX

The case with W2 paraffin is then performed, to identify the influence of different liquid viscosity and surface tension on the entrainment phenomenon.

Property	W2	GOX
$\rho[kg/m^3]$	740.3	0.911
$\nu[m^2/s]$	3.63x10^{-6}	26.65x10^{-6}
$\sigma[N/m]$	23.58x10^{-3}	−

Table 5.2.5: Transport properties for W2 and GOX at $T = 423K$

(a) $t = 2ms$ (b) $t = 6ms$

(c) $t = 10ms$ (d) $t = 14ms$

(e) $t = 18ms$ (f) $t = 22ms$

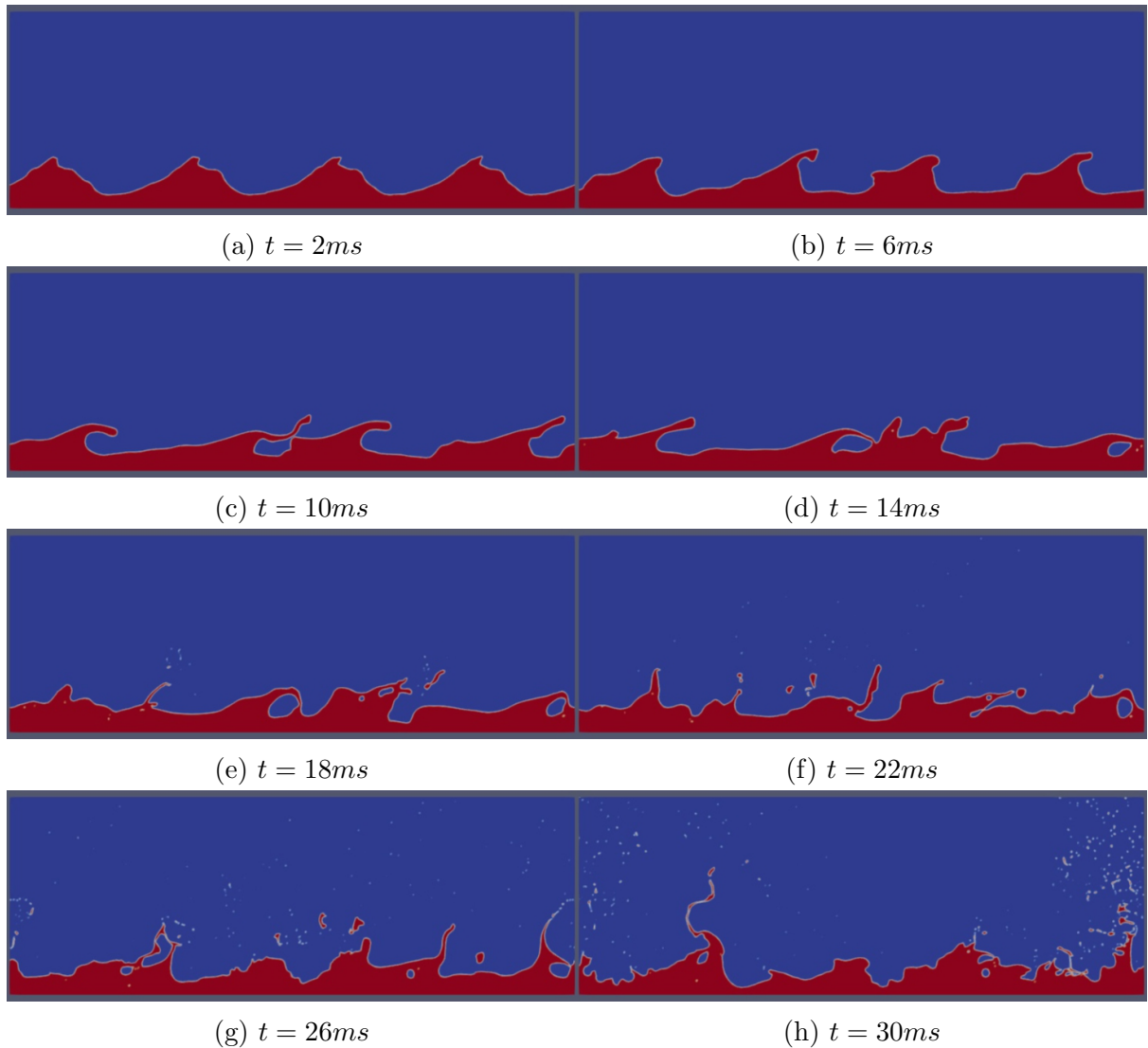(g) $t = 26ms$ (h) $t = 30ms$

Figure 5.2.13: Entrainment of liquid W2 in gaseous oxygen at $T = 423K$

With this paraffin the droplets start detaching earlier than in the previous case. The lower liquid layer viscosity and surface tension thus allow for a lower critical condition

for the entrainment onset. The primary break-up happens between $17.2\ ms$ and $17.4\ ms$, as shown in Figure 5.2.14.

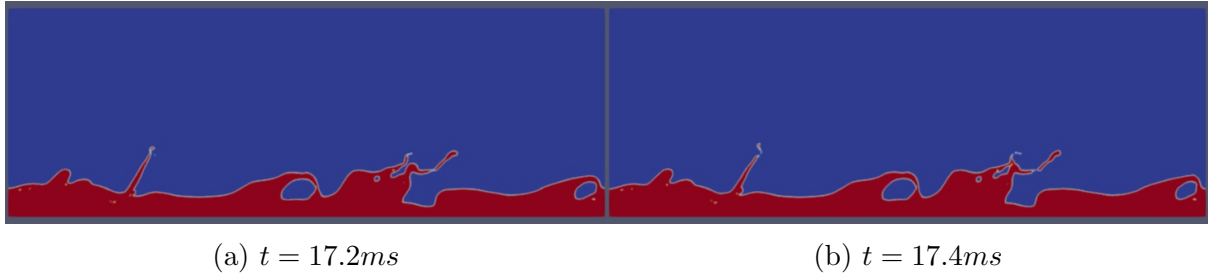(a) $t = 17.2ms$ (b) $t = 17.4ms$

Figure 5.2.14: Primary break-up for liquid W2 and gaseous oxygen at $T = 423K$

W3+GOX

The entrainment simulation for the W3 paraffin is performed, with the transport properties reported in the following table.

Property	W3	GOX
$\rho[kg/m^3]$	730.4	0.911
$\nu[m^2/s]$	2.41x10^{-6}	26.65x10^{-6}
$\sigma[N/m]$	23x10^{-3}	−

Table 5.2.6: Transport properties for W3 and GOX at $T = 423K$

This is the considered paraffin with the lowest viscosity and surface tension, thus the lowest critical condition for the entrainment onset. The results in Figure 5.2.15 and 5.2.16 confirm the prediction from the theoretical model. The primary break-up is realized in the order of $1ms$, an order of magnitude lower than for the other two cases. Also, the amount of generated droplets is more significant than for the other paraffins.
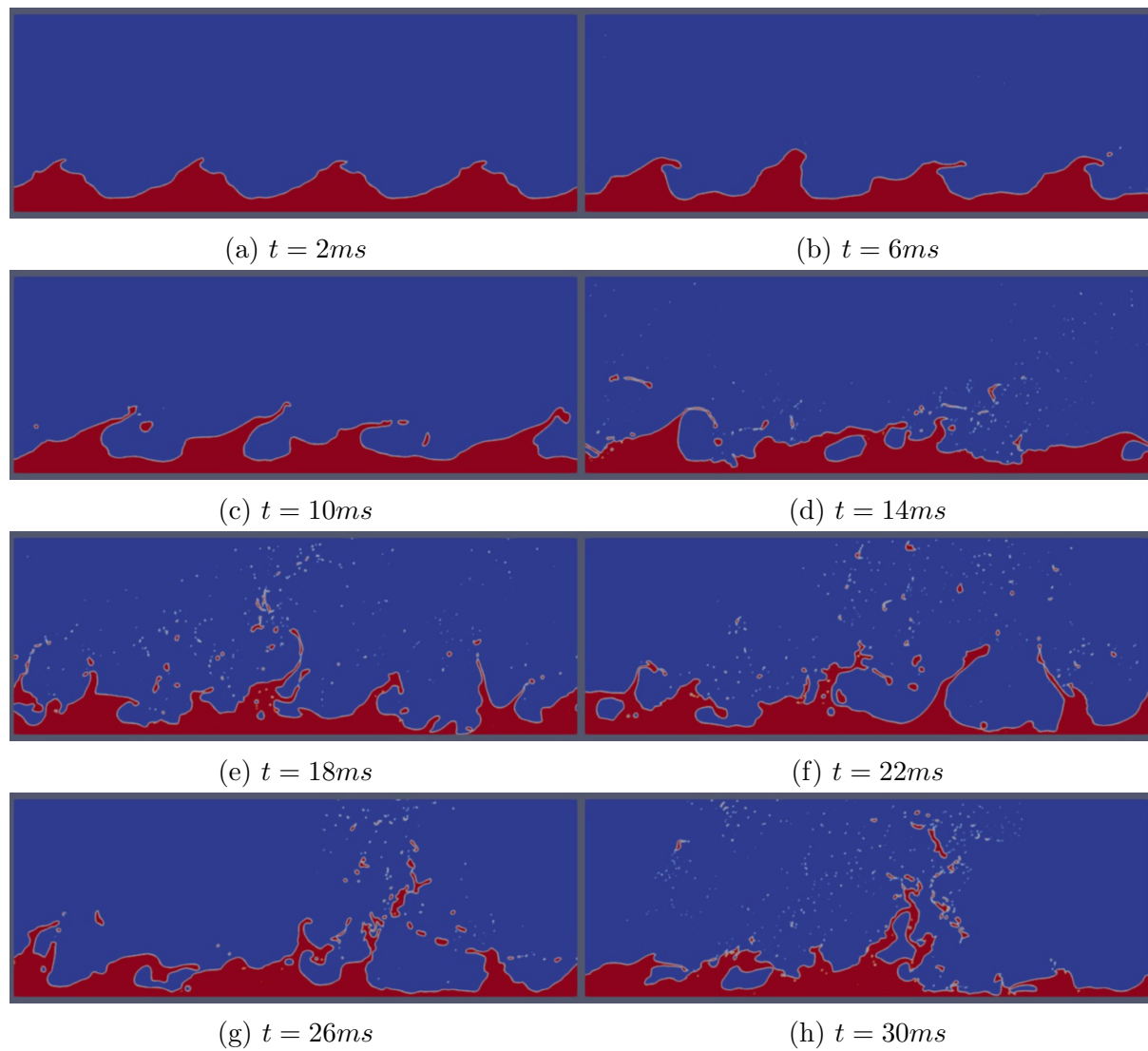
(a) $t = 2ms$ (b) $t = 6ms$

(c) $t = 10ms$ (d) $t = 14ms$

(e) $t = 18ms$ (f) $t = 22ms$

(g) $t = 26ms$ (h) $t = 30ms$

Figure 5.2.15: Entrainment of liquid W3 in gaseous oxygen at $T = 423K$

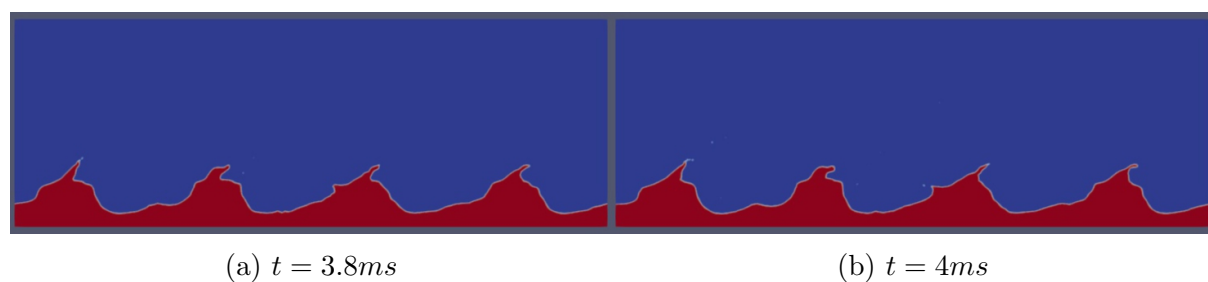
(a) $t = 3.8ms$ (b) $t = 4ms$

Figure 5.2.16: Primary break-up for liquid W3 and gaseous oxygen at $T = 423K$

Chapter 6

Numerical simulation of the temperature profile through the solid, liquid and gaseous phase

In the previous chapter a temperature of $150°C$ is employed, which is taken in reference with previous performed experiments on the entrainment phenomenon. An improvement in the study of the liquid mass transfer should be made considering the evolution of the temperature in the three phases once the flame is established.

While it was difficult to access the laboratory in this time, efforts were made to set up a numerical simulation for the heat transfer in a case with stationary boundary conditions. The basic simplified case considers three region: a solid part, a liquid part, and a gaseous phase with a mixture of fuel vapours and combustion products. Under the influence of the flame temperature, obtained with CEA software, the temperature in the liquid region is modified until convergence. The heat flux at the interfaces is also calculated through OpenFOAM utilities. While this system requires to be further modified, considering a multiphase flow solver for the fluid region, some early results can show the sensitivity to the liquid layer thickness and the height of the flame.

The information on the flame location and the boundary layer characterization are retrieved from ongoing work at the SPLab, which is focused on the Sasol Wax 6805. For this reason, this paraffin is considered for the computational model.

6.1 CEA calculations

Chemical Equilibrium and Applications is a program developed by NASA. It requires the reactants species and the combustion conditions as input and calculates chemical equilibrium product concentrations, determining also thermodynamic and transport properties for the product mixture. These properties would then be needed as a parameter in OpenFOAM.

Input

For sake of simplicity, the case is considered at ambient pressure, as for the previous simulations; also, the combustion efficiency is not taken into account and the flame is supposed to be generated at stoichiometric. Considering the following complete combustion reaction for W2 with oxygen, the oxidizer to fuel weight ratio is obtained.

$$C_{40}H_{82} + a\,O_2 \longrightarrow b\,CO_2 + c\,H_2O \qquad (6.1.1)$$
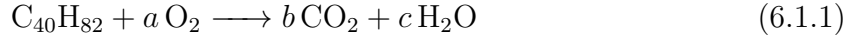
The mass balance leads to:

$$\begin{cases} a = \dfrac{121}{2} \\ b = 40 \\ c = 41 \end{cases} \qquad (6.1.2)$$

The stoichiometric oxidizer to fuel ratio is then retrieved.

$$\frac{aW_{O_2}}{W_{C_{40}H_{82}}} = 3.44 \qquad (6.1.3)$$

The CEA software allows the possibility to select paraffin as fuel, but request the enthalpy of formation, that needs to be calculated. This is done by subtracting the latent heat of fusion from the enthalpy of formation for the liquid paraffin, which leads to:

$$\Delta Hf^\circ(liquid) = \Delta Hf^\circ(at\,298K) - L_m = -1179.81\ kJ/mol \qquad (6.1.4)$$

Where the standard enthalpy of formation for paraffin at $298K$ is obtained as indicated in reference [47].

$$\Delta Hf^\circ(\text{at } 298.16K) = (-10.887 - 6.106 * n)\ kcal/mol \qquad (6.1.5)$$

The used inputs are summarized in the following table.

Property	Value	Unit
Pressure	1	bar
Oxidizer to fuel wt. ratio	3.44	$-$
Temperature of the fuel	298.16	K
Enthalpy of the fuel	-1179.851	kJ/mol

Table 6.1.1: Parameters for CEA calculation

Output

Selecting the *rocket* option among the chemical equilibrium problem types, the properties in the chamber, at the throat and at the nozzle exit are obtained. The condition in the

combustion chamber are those needed for the simulation of the temperature evolution; they would be reported in the Table 6.1.2. These parameters refer to the combustion products of paraffin Sasol Wax 6805 ($C_{40}H_{82}$) and oxygen (O_2).

Property	Value	Unit
Flame temperature	3105.11	K
Density	9.6304×10^{-2}	kg/m^3
Molar weight	24.863	g/mol
Specific heat	1.8065	$kJ/kg/K$
Dynamic viscosity	1.0186×10^{-4}	$kg/m/s$
Prandtl number	0.6641	−

Table 6.1.2: CEA output

6.2 Temperature profile

With the scope of calculating the temperature evolution in the different phases a two-dimensional simulation is set up with OpenFOAM. Following the model of Karabeyoglu[23], the heat transfer in the solid and liquid layer is considered solely due to conduction, while the heat is transferred convectively and conductively in the gas phase from the flame. Radiation is not implemented yet, since the study is focused on the feasibility of the model, but it would be possible to further add the radiation properties in this simulation.

The three regions are fixed in a domain of 10 cm in the axial direction, starting from the leading edge of the grain. The thickness of the solid layer is of 1 cm; the gas phase is flowing from an inlet on the left to an outlet on the right and is initialized at a velocity of 5 m/s. The temperature between the liquid and the solid phase is fixed at the melting temperature, and the one at the top boundary of the gas phase is set at the flame temperature. Considering an oxidiser velocity of 5 m/s, which roughly corresponds to an oxygen mass flow of 45 g/s, the height of the flame is set at 1.92 mm over the liquid fuel surface, according to an analysis proceeding at the SPLab on pure Sasol Wax 6805 paraffin. The height of the melt layer was calculated by Garg[17] in accordance with the theoretical model; for an average regression rate of 1 mm/s, a thickness of 0.1 mm was obtained. These two values would be firstly considered and then modified to account for the sensitivity of these parameters. Like in the model of Karabeyoglu, the domain is in the reference system of the liquid layer; thus as the fuel is regressing the geometry is moving with it. The temperature at the liquid-gas interface would be calculated by the software. Noticed the stationary boundary conditions, this value would converge after a certain time.

6.2.1 chtMultiRegionFoam

The solver employed for this simulation is `chtMultiRegionFoam`, which allows to work with different regions with different properties. Originally thought to solve heat transfer between solid and fluid, it is a solver for steady or transient fluid flow and solid heat conduction, with conjugate heat transfer (cht) between segregated regions, each one being a coherent continuum of the same phase. Separate governing equations for each continuum are solved, with the partitioned approach: solve separate matrix

equation systems, couple at the boundary interface, sub-iterate until coupled convergence is reached[50]. This means that the equations for each variable characterizing the system is solved sequentially and the solution of the preceding equations is inserted in the subsequent equation. The coupling between fluid and solid follows the same strategy: first the equations for the fluid are solved using the temperature of the solid of the preceding iteration to define the boundary conditions for the temperature in the fluid. After that, the equation for the solid is solved using the temperature of the fluid of the preceding iteration to define the boundary condition for the solid temperature. This iteration procedure is executed until convergence.

In the fluid region the compressible Navier-Stokes equation are solved. The solver is pressure based, thus the pressure equation is used to establish the connection between the momentum and the continuity equation. The steps followed from the algorithm are:

- Update the density from the continuity equation

- Solve the momentum equation, computing a velocity u^*

- Solve the energy equation, computing T at the new time step.

- Solve the pressure equation to solve mass conservation; velocity is corrected to satisfy the mass equation.

- Correct the density from the pressure and the temperature field through the equation of state.

For the solid regions only the energy equation has to be solved, which states that the temporal change of enthalpy of the solid is equal to the divergence of the heat conducted through the solid.

At the interface the temperature should match and the heat flux entering one region at one side of the interface should be equal to the heat flux leaving the other region on the other side of the domain. This coupling is reached through the mixed boundary condition *compressible::turbulentTemperatureCoupledBaffleMix*.

chtMultiRegionFoam case setup

Before running the solver, a preparatory phase needs to be done to set up the boundary conditions, the parameters and the schemes to be used for each region. This process is summarized in Figure 6.2.1.

First, it is required to generate the geometry and the mesh, through the `blockMesh` tool. The boundary conditions are required to be initialised; they are saved in a `0.origin` folder, which is copied to `0` folder. Then the domain is divided into regions through selection of cells subsets (*cellSet*) and their transformation into zone (*cellZoneSet*), a coherent subset of cells which can be used to define a region. For this goal, the `topoSet` utility uses as input a dictionary file in the `system` folder with the commands to be executed. In the current case the cells subsets are defined through `boxToCell` function. After all the regions are defined, the mesh of the domain has to be split into several disjoint meshes, through the command `splitMeshRegions`.

The properties of the different regions needs to be applied to the respective cell subsets. Thus, in the `constant` and `system` directories a folder for each region needs to be created. In the `constant` folder the thermophysical properties, radiation properties and turbulence model for each zone are defined; it also is necessary to build here a file called `regionProperties`, that assigns the physical phase to each region, either fluid or solid. In the `system` directory the `fvSchemes` and `fvSolution` are defined for each zone, by having one file in the respective folders; also in each region folder there should be a `changeDictionaryDict` file, which contains details about the necessary fields like temperature and velocity. The command line `changeDictionary` is used to specify appropriately the initial, boundary and coupling conditions for all fields.

Once this process is completed the command line `chtMultiRegionFoam` can be use correctly. In this case, the application is run in parallel to reduce the overall computational time.
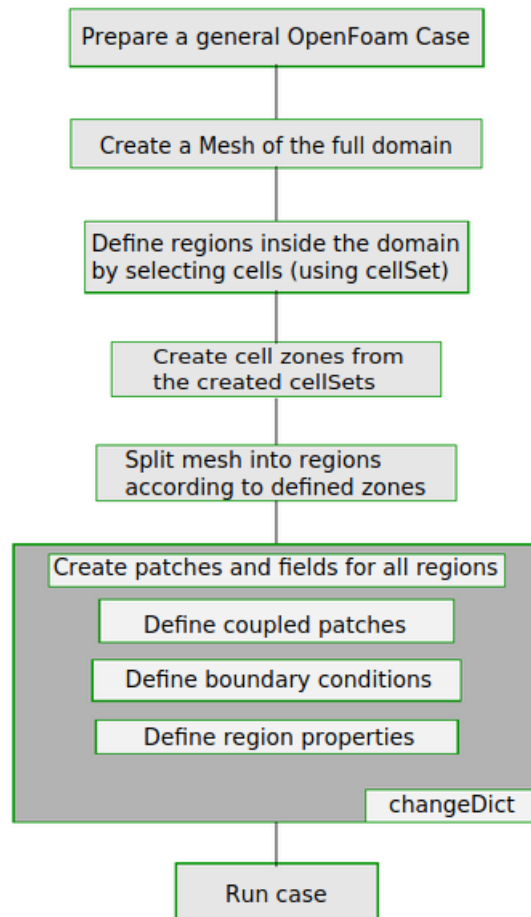

Figure 6.2.1: Basic work flow for chtMultiRegionFoam[50]

6.2.2   Simulation of the basic case

The basic case considers the height of the flame at 1.92 mm and the thickness of the melt layer as 0.1 mm from previous studies. The initial domain obtained with `splitMeshRegion` is shown in Figure 6.2.2.
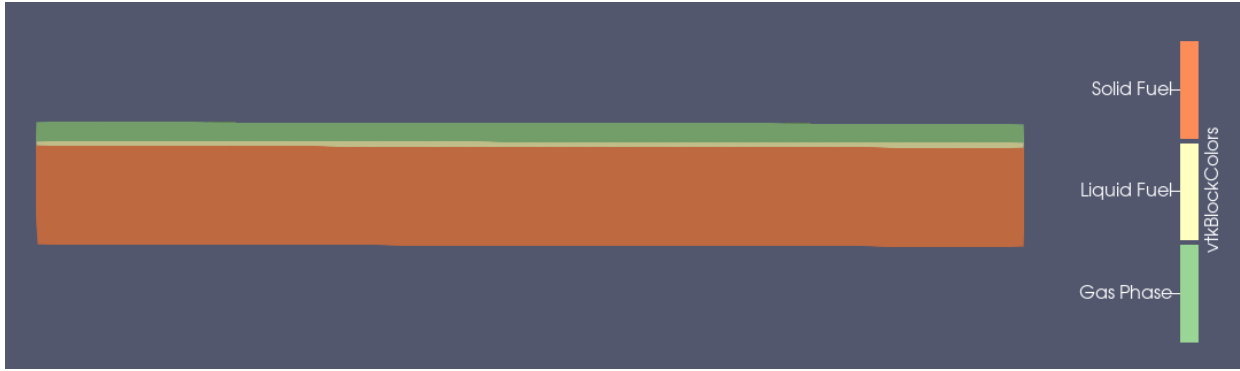
Figure 6.2.2: Domain for temperature profile evaluation

The region properties, written in the file `thermophysicalProperties`, are reported in Table 6.2.1 for each phase. The solid and liquid properties of the paraffin wax are those reported in Table 4.1.7. As anticipated, since only conduction is wanted to be solved for liquid phase, this region is defined as a solid region. Also, when inserting it in the fluid regions, the velocity field in this part results to be infinitesimal. The gas phase between the liquid layer and the flame is composed of combustion products and fuel vapours. The transport and thermophysical properties for this region are then an average of those obtained from CEA for the combustion products and butane (C_4H_{10}).

Solid Fuel		Liquid Fuel		Gas Phase	
W	562 g/mol	W	562 g/mol	W	41.43 g/mol
C_p	2529.84 $J/kg/K$	C_p	2987.53 $J/kg/K$	C_p	2397 $J/kg/K$
λ	0.329 $W/m/K$	λ	0.167 $W/m/K$	μ	5.7625x10^{-5} $kg/m/s$
ρ	939 kg/m^3	ρ	740.3 kg/m^3	Pr	0.692

Table 6.2.1: Thermophysical properties used for the simulations

The solid phase is initialised at 300 K, the liquid at 343 K, the gas phase at 1200 K. The temperature between the liquid and the solid is fixed at 343 K, at the bottom of the solid at 300 K, and at the top of the gas phase, where the flame would be located, at 3105.11 K. It is checked that the Courant number in the fluid region remains under 1 and that the diffusion number in the solid region is lower than 10. No turbulence model is applied, but a very fine mesh is considered for the gas phase and the liquid layer, 0.1x0.02 mm in the former and 0.1x0.025 mm in the latter. In the solid phase the mesh is graded of a factor of 10 from the interface with the liquid to the cold end.

After the simulation is started, the temperature profile in the regions evolves; it stabilises after 0.99 s of simulated time. The heat flux at the coupled boundaries is calculated through the post process utility *wallHeatFlux* of OpenFOAM. The results are as follows, with the gas to liquid heat flux actually oscillating around the listed values.

- **Liquid to solid:** Max/Min= -8.038x$10^3/-2.656$x10^5 W/m^2, Integral= -2.046 W

- **Gas to liquid:** Max/Min= -7.500x$10^3/= -2.690$x10^5 W/m^2, Integral= -2.067 W

In these pages the results of relevance about the temperature profile are reported; they refer to: the temperature field along the gas/liquid interface; the evolution in the three phases at the axial coordinate where the temperature of vaporization (or the closest one) is reached at the liquid surface; the evolution in the liquid layer at the same axial coordinate.
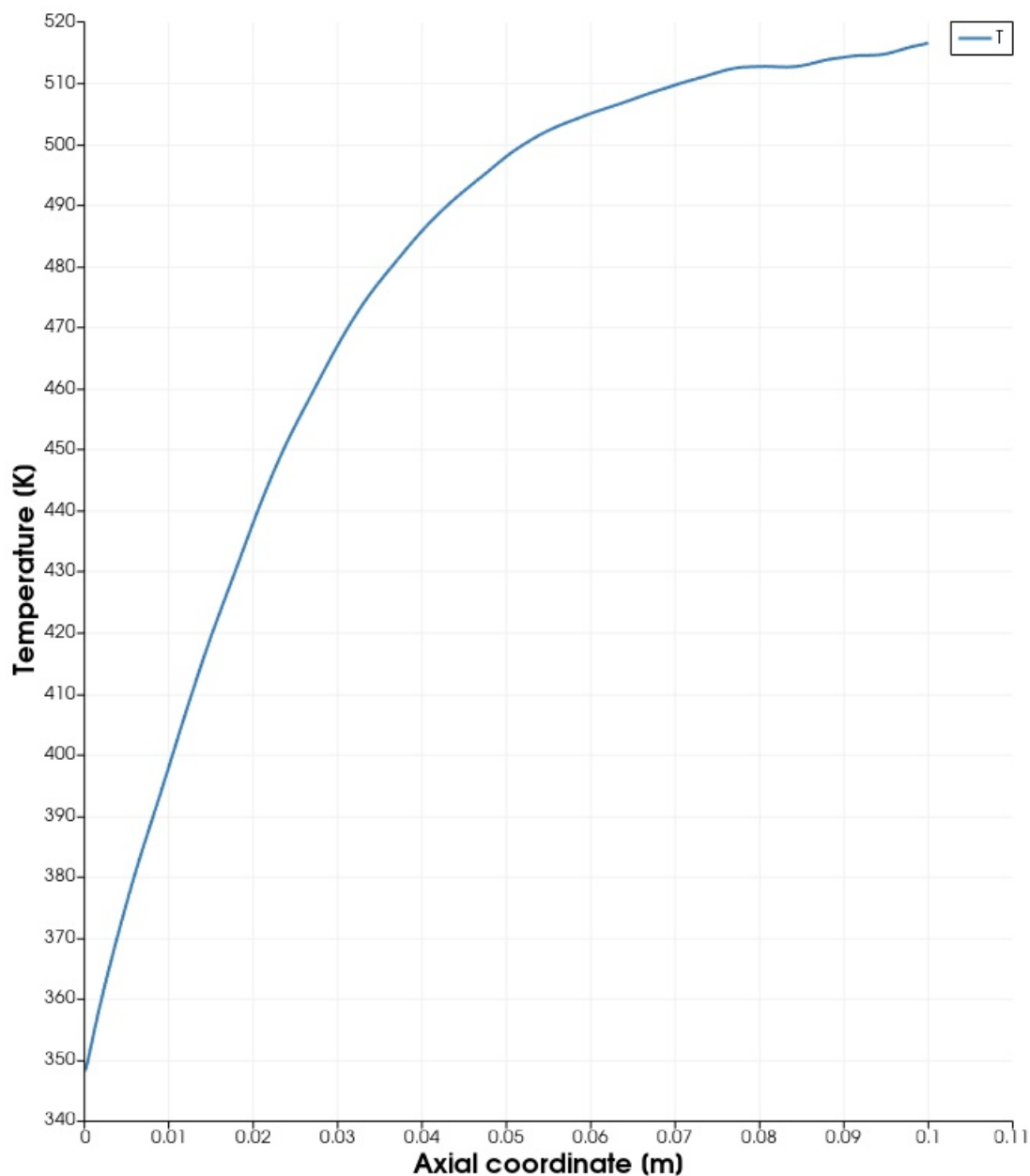

Figure 6.2.3: Temperature of the liquid fuel surface for $h = 0.1 \ mm$

From Figure 6.2.3 it is evinced that the temperature along the liquid surface is largely influenced by the axial position, especially when close to the leading edge of the grain. It arise from a value around the melting temperature to above $510 \ K$ at the end of the domain, with a logarithmic trend. The vaporization temperature is not reached within this domain.
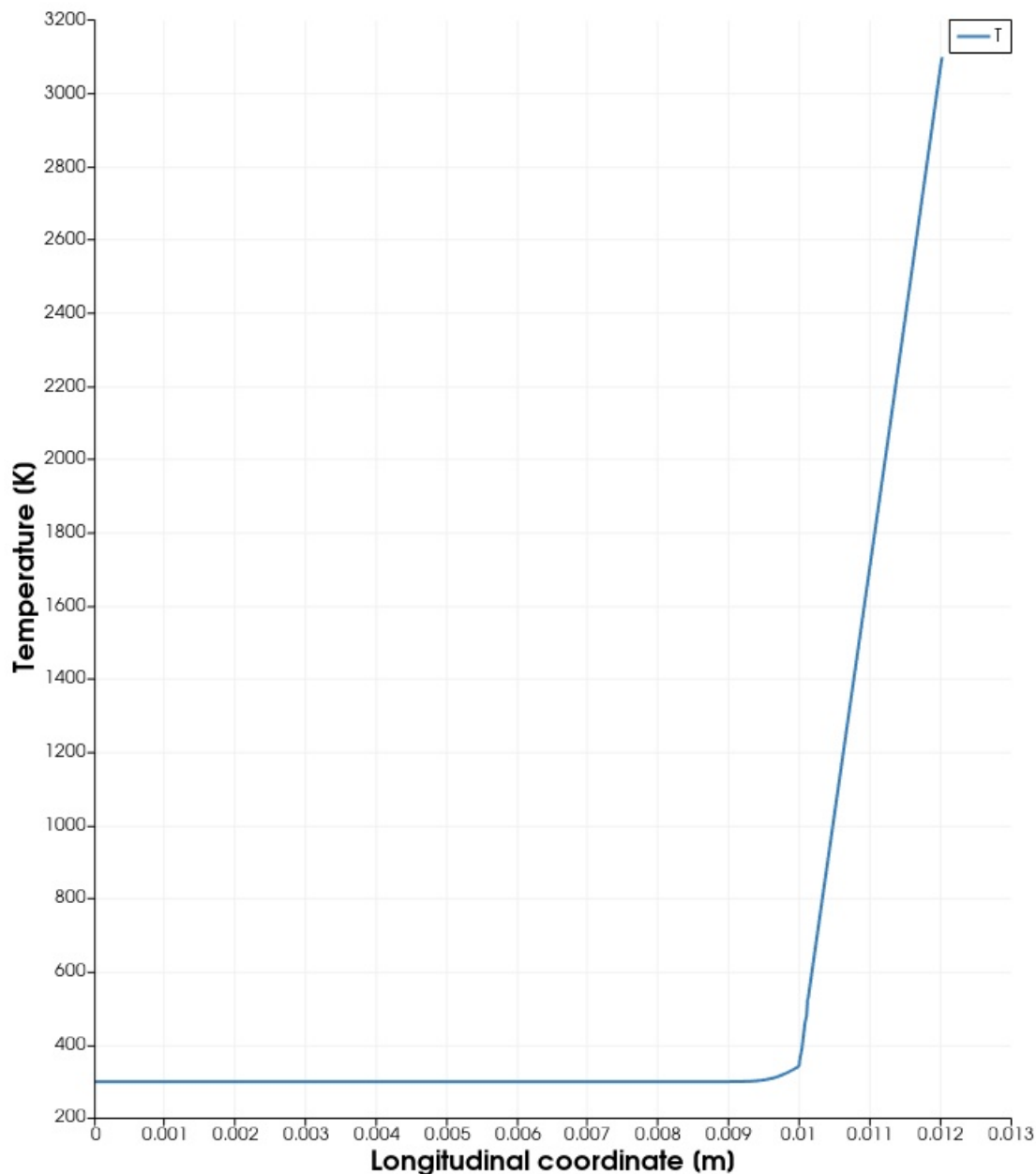
Figure 6.2.4: Temperature profile along the solid, liquid and gas phase for $h = 0.1\ mm$, at a distance from the leading edge of $0.1\ m$

The longitudinal evolution of temperature is reported at the axial position of $0.1\ m$, at which it reached the closest value to the vaporisation point. Figure 6.2.4 shows that the heat flux toward the solid phase affects only $1\ mm$ below the solid surface; then the temperature is constant at the ambient value. On the other hand, the temperature gradient in the liquid and gas phase is huge, passing from a value of $343\ K$ to $3105.11\ K$ in $2.02\ mm$. In Figure 6.2.5 the temperature profile in the solely liquid layer is reported. The fragmented feature of the graph is due to the presence of only four layer mesh into this region, since the considered melt layer thickness is very low. This issue may also be at the base of the oscillating heat flux values. The highest temperature reached in this case is between 510 and $520\ K$.
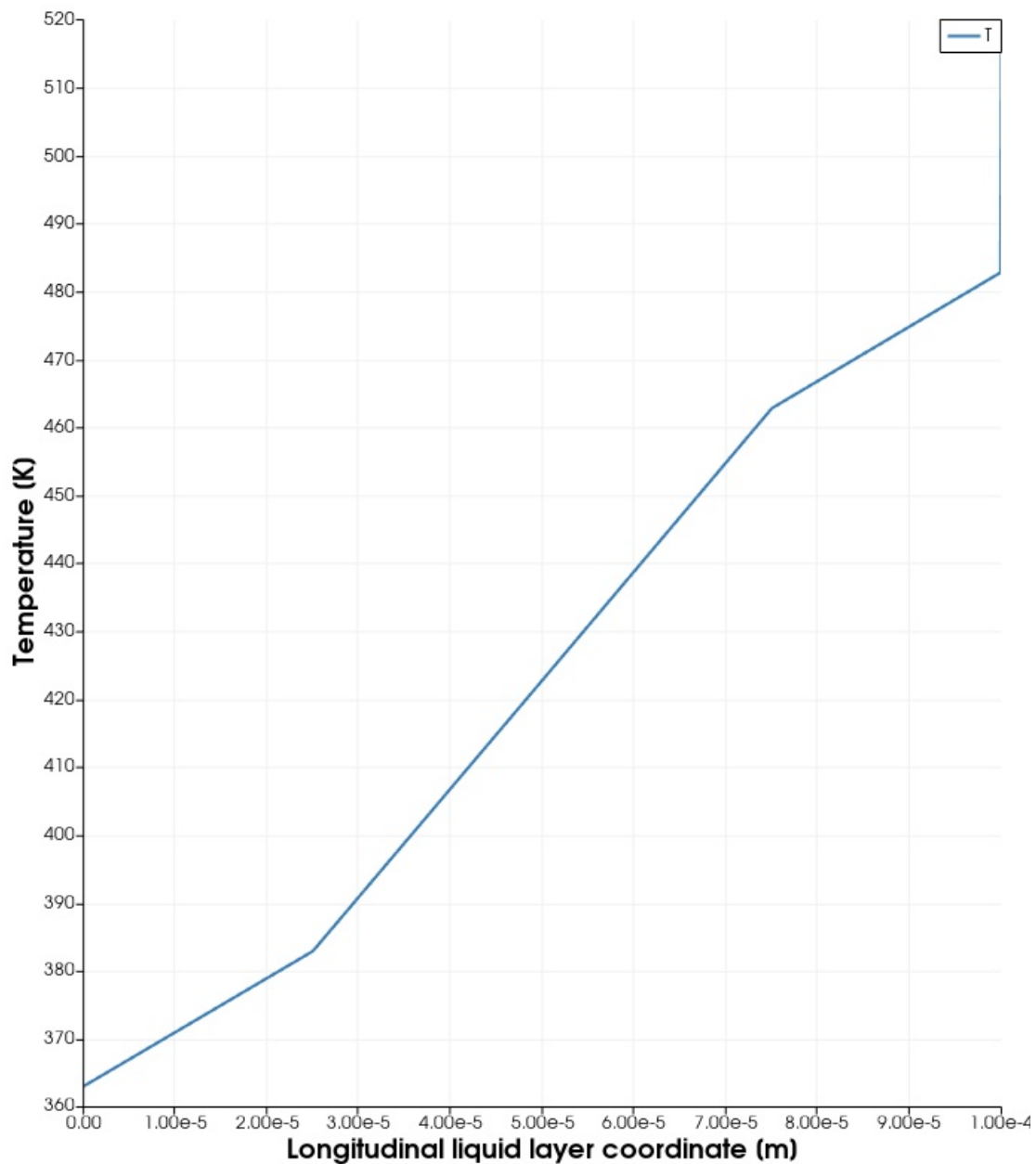
Figure 6.2.5: Temperature profile along the liquid layer for $h = 0.1\ mm$, at a distance from the leading edge of $0.1\ m$

6.2.3 Liquid layer thickness

Considering the flame fixed at $1.92\ mm$ over the liquid surface, the thickness of the melt layer is varied to the values of $0.5\ mm$ and $1.0\ mm$. The mesh definition is the same as for the basic case.

Melt layer of $0.5mm$

In this case, the convergence is reached later, at the time $1.72\ s$. The heat fluxes are here reported; they are in the same order of magnitude of the previous case, but both the integral values are lower.

- **Liquid to solid:** Max/Min= $-5.586\text{x}10^3/-1.554\text{x}10^5 \ W/m^2$, Integral= $-1.149 \ W$

- **Gas to liquid:** Max/Min= $-7.746\text{x}10^3/= -2.249\text{x}10^5 \ W/m^2$, Integral= $-1.627 \ W$

The following graphs are reported as the ones for the previous case. In Figure 6.2.6 the evolution along the liquid surface is shown; the trend is logarithmic as before, but the vaporization temperature is reached this time at the axial coordinate $0.028 \ m$. The highest value reached at the surface is of $885.81 \ K$.
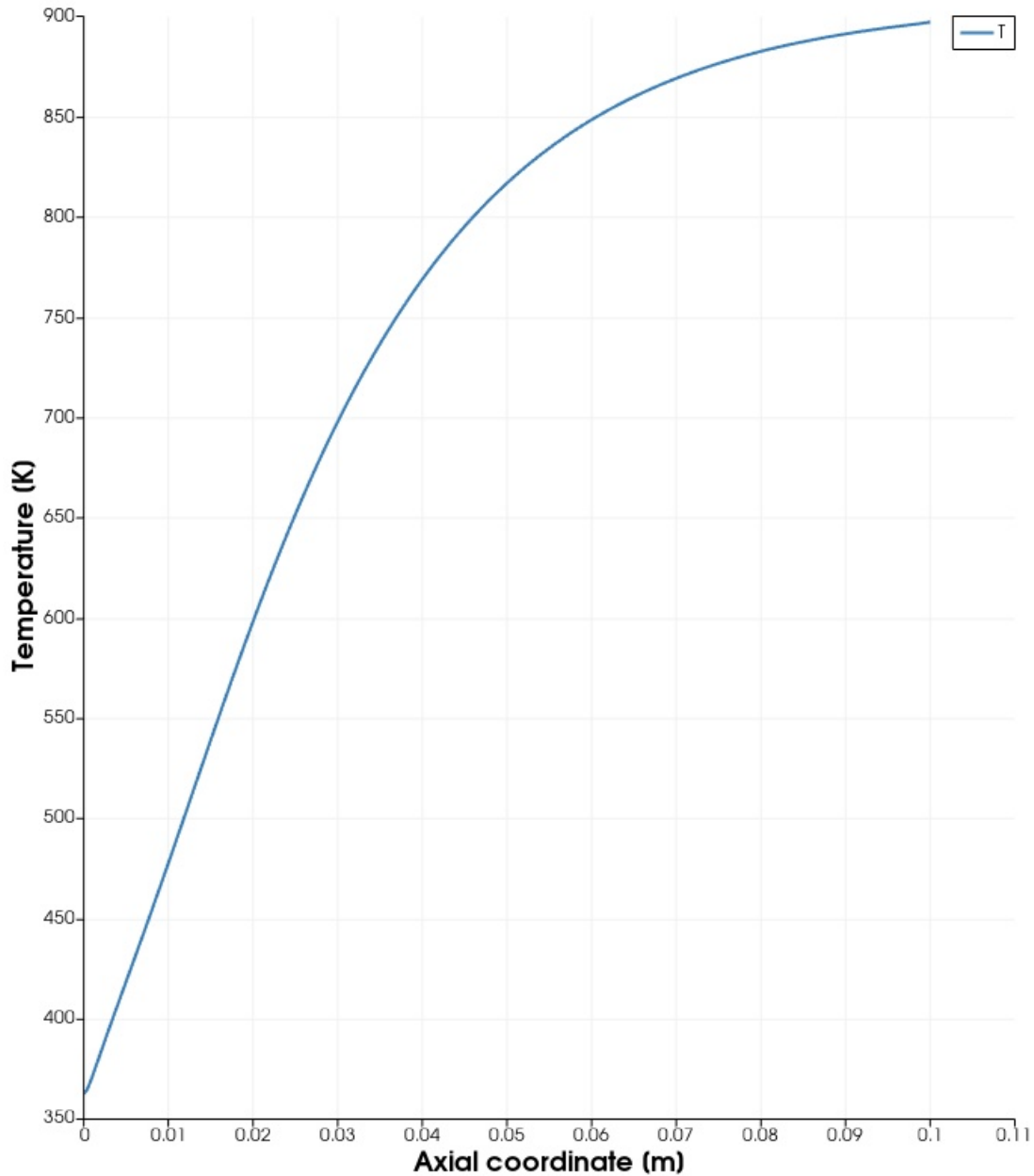

Figure 6.2.6: Temperature of the liquid fuel surface for $h = 0.5 \ mm$

The graphs of the temperature profile along the three phases (Figure 6.2.7) and in the liquid surface (Figure 6.2.8) are obtained at the axial coordinate where the vaporisation temperature of $681.02 \ K$ is reached.

66

In this case it is noticeable the exponential trend in all the three phases. As before, the temperature in the solid phase changes only in the last millimeter close to the solid/liquid interface. The longitudinal distance between the melt point an the flame temperature is this time of 2.42 mm; the gradients are still considerably high, especially in the liquid fuel, considering the higher temperatures reached in this case at the surface of the melt layer.
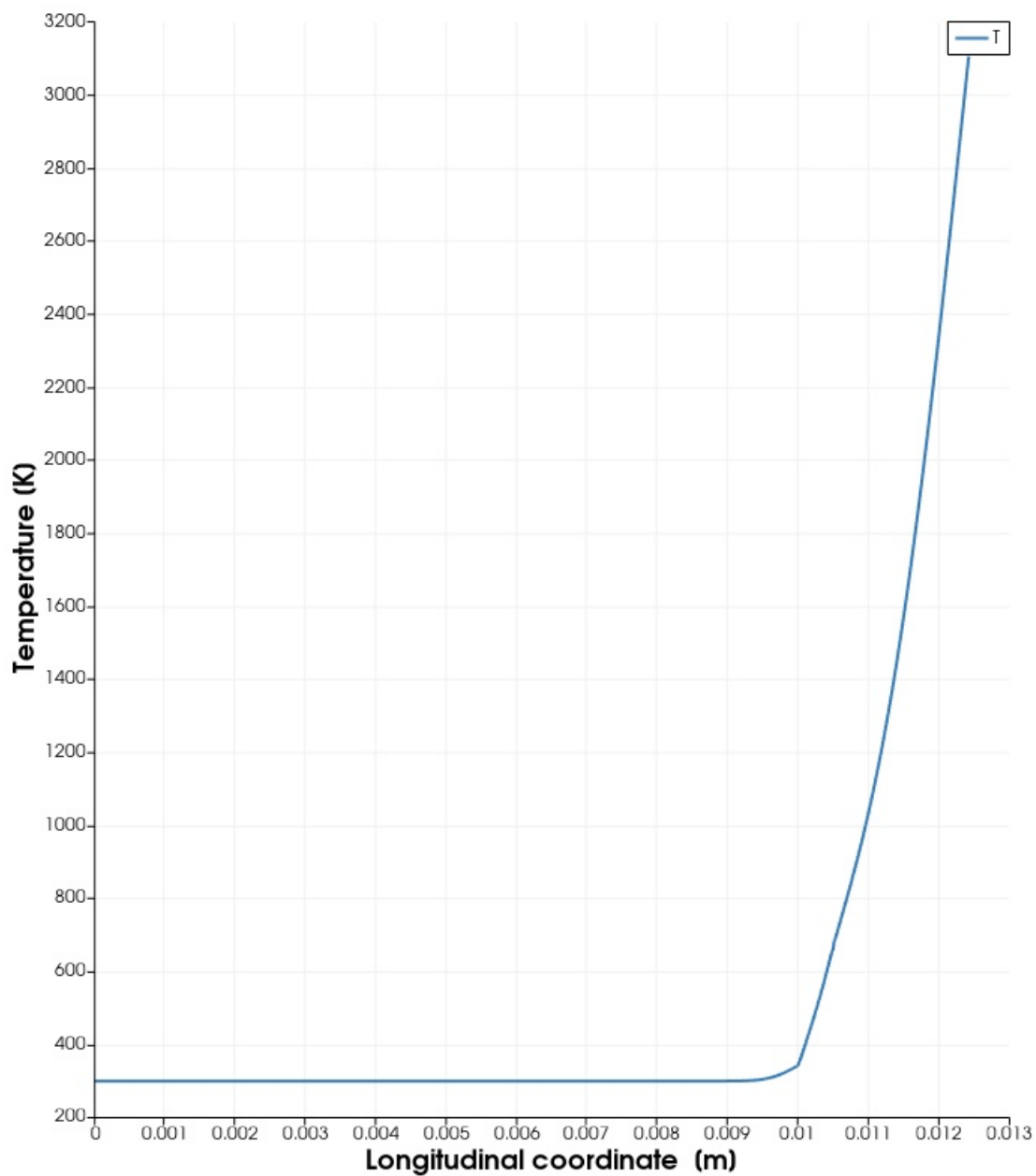

Figure 6.2.7: Temperature profile along the solid, liquid and gas phase for $h = 0.5\ mm$, at a distance from the leading edge of $0.028\ m$
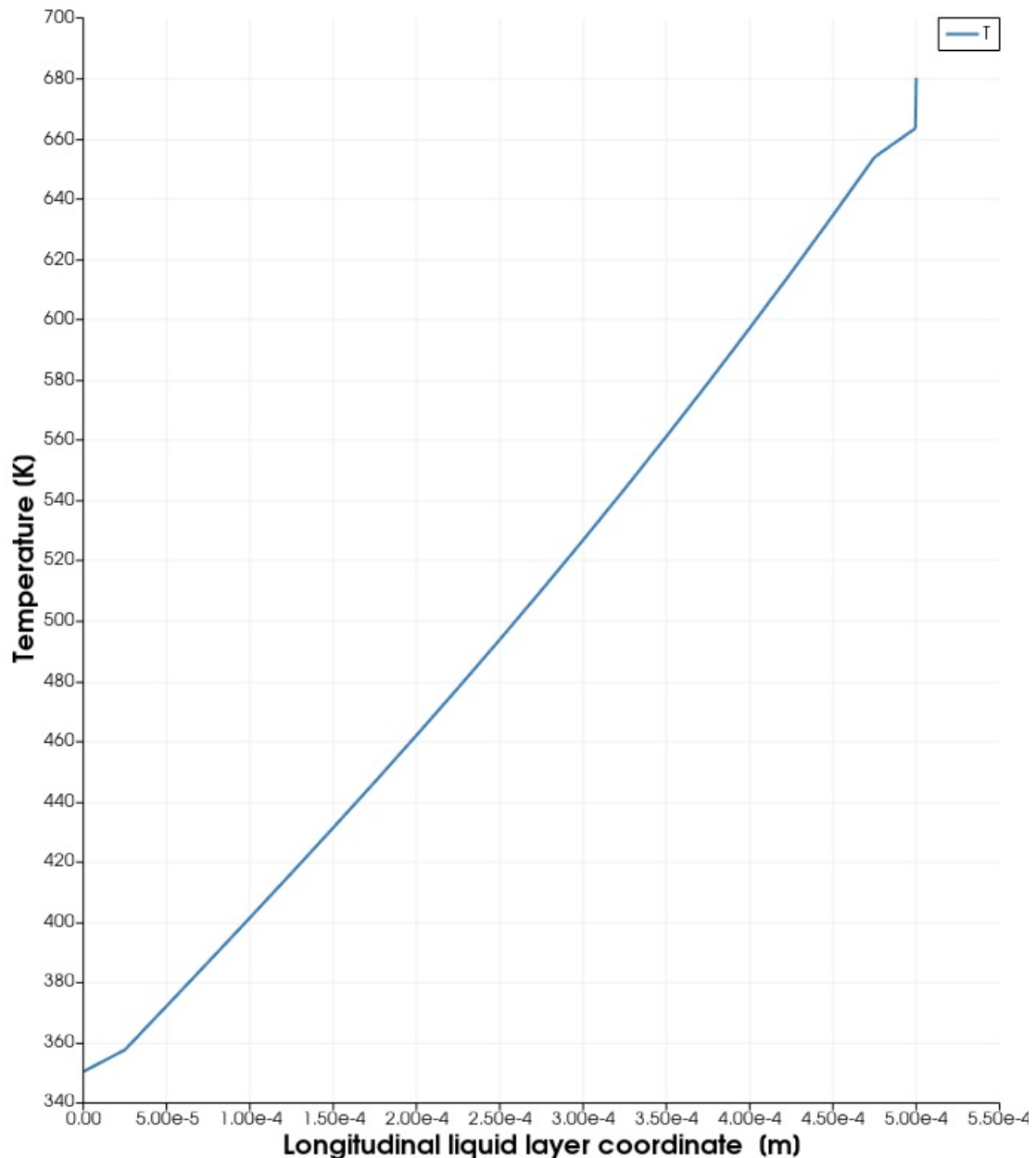
Figure 6.2.8: Temperature profile along the liquid layer for $h = 0.5\ mm$, at a distance from the leading edge of $0.028\ m$

Melt layer of $1.0mm$

The melt layer is increased to $1.0\ mm$ to see the variation in the heat fluxes and in the achievement of the vaporisation temperature. The convergence happens later also in this case. Also, both the heats transferred across the interfaces are lower, confirming the previous trend.

- **Liquid to solid:** Max/Min$= -2.075\mathrm{x}10^3/-5.321\mathrm{x}10^4\ W/m^2$, Integral$= -3.942\mathrm{x}10^{-1}\ W$

- **Gas to liquid:** Max/Min$= -7.983\mathrm{x}10^3/= -2.107\mathrm{x}10^5\ W/m^2$, Integral$= -1.502\ W$

Especially, at the liquid/solid interface the integral value is lower than one order of magnitude. The larger thickness of the melt layer, with the consequent lower temperature gradient is probably responsible for this fact.

In Figure 6.2.9 the temperature evolution at the liquid/gas interface is reported. The logarithmic trend from the leading edge to the end of the domain is confirmed. The highest value of temperature reached at the of the chamber is of 1013.76 K.
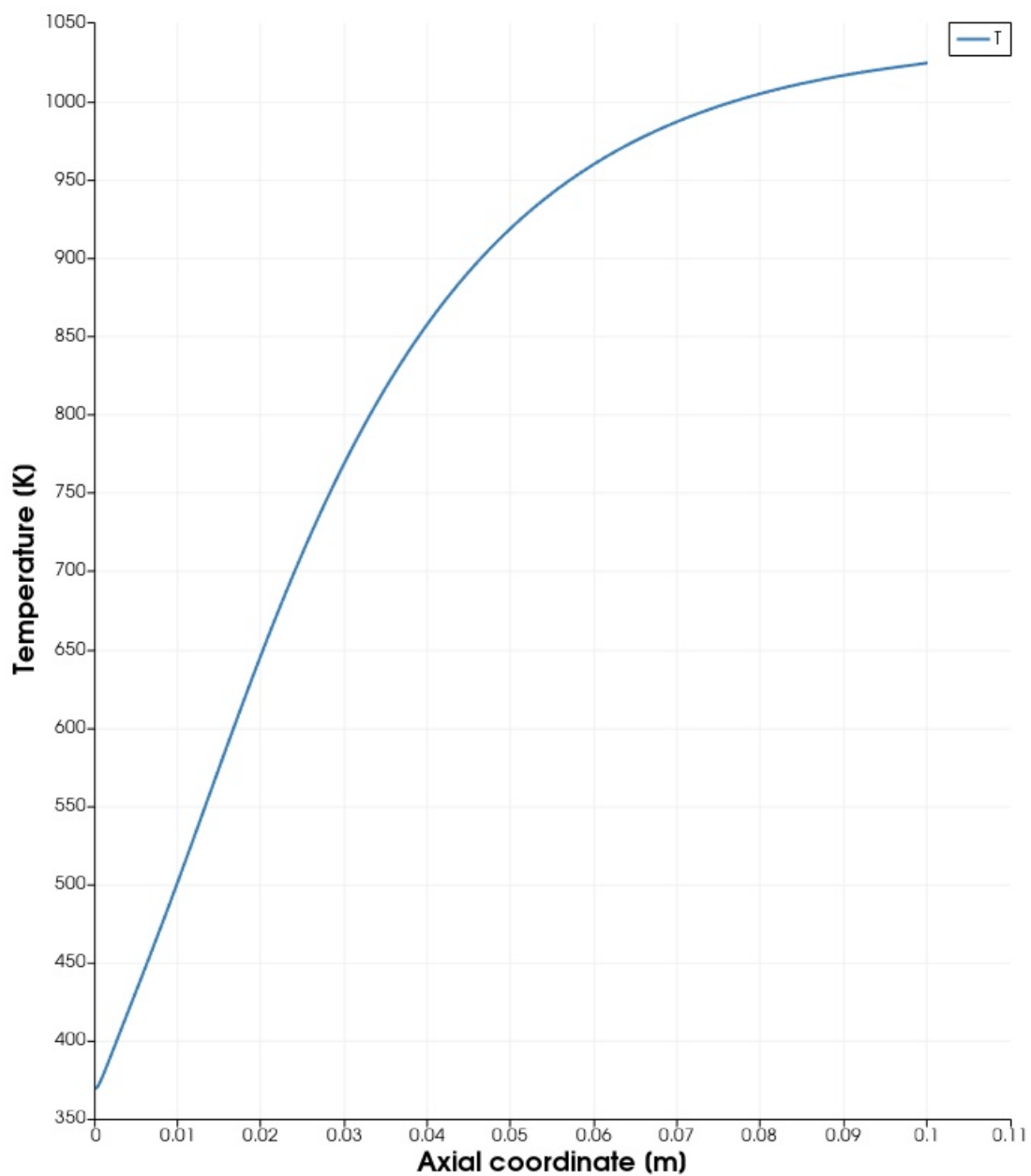

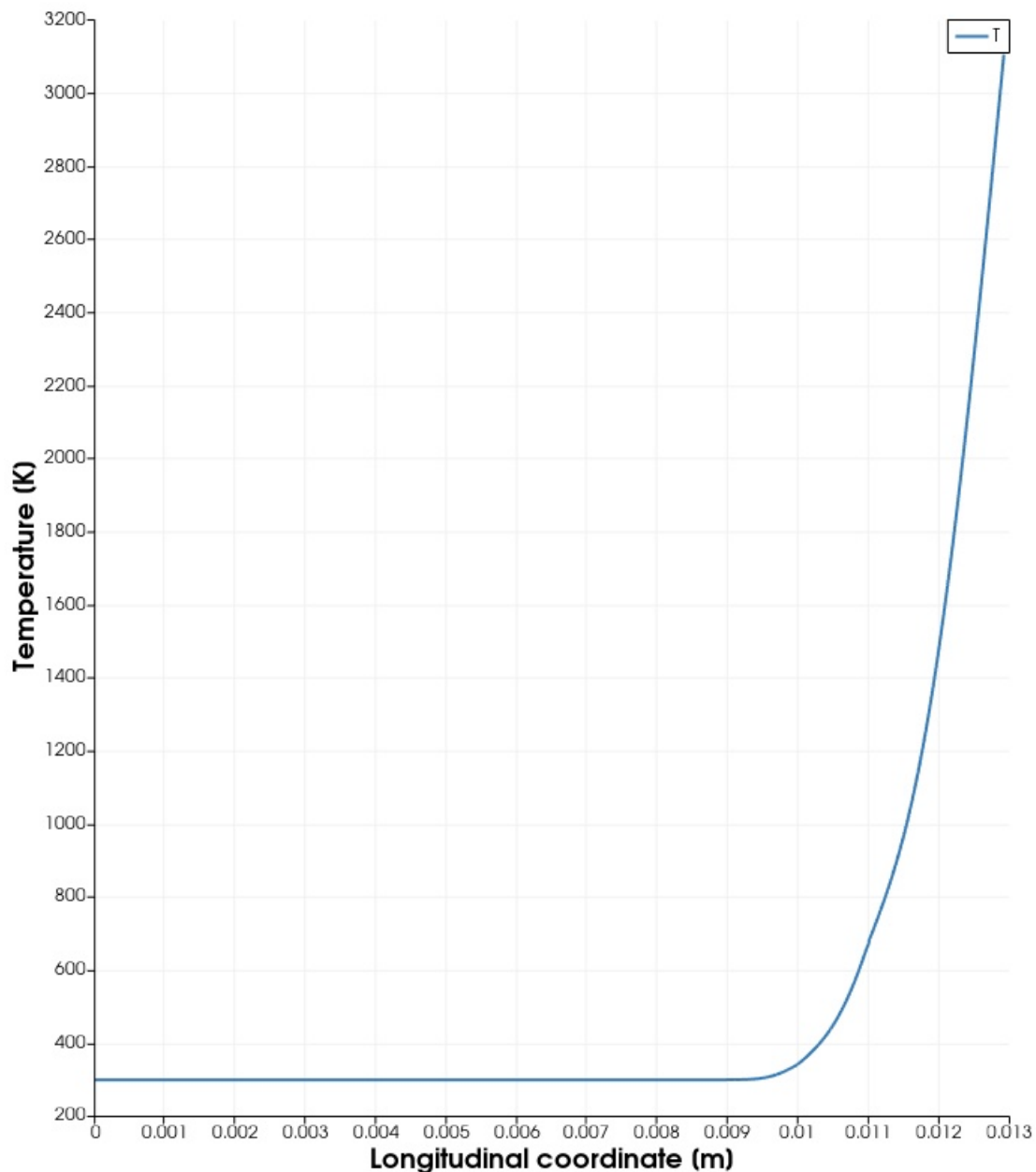Figure 6.2.9: Temperature of the liquid fuel surface for $h = 1\ mm$

Figure 6.2.10: Temperature profile along the solid, liquid and gas phase for $h = 1 \ mm$, at a distance from the leading edge of $0.0227 \ m$

In this case the vaporisation temperature is reached at a distance from the leading edge of $0.0227 \ m$. The temperature profile at this point is reported in the previous graph, Figure 6.2.10. The exponential trend is remarkable.

The same trend is recorded for the temperature profile in the solely liquid layer, in Figure 6.2.11. The gradient at this axial coordinate is lower than for the previous case, considered that the thickness is doubled. Anyhow at the end of the chamber, a temperature higher of about $130 \ K$ is reached, compared to the case with a liquid layer thickness of $0.5 \ mm$.
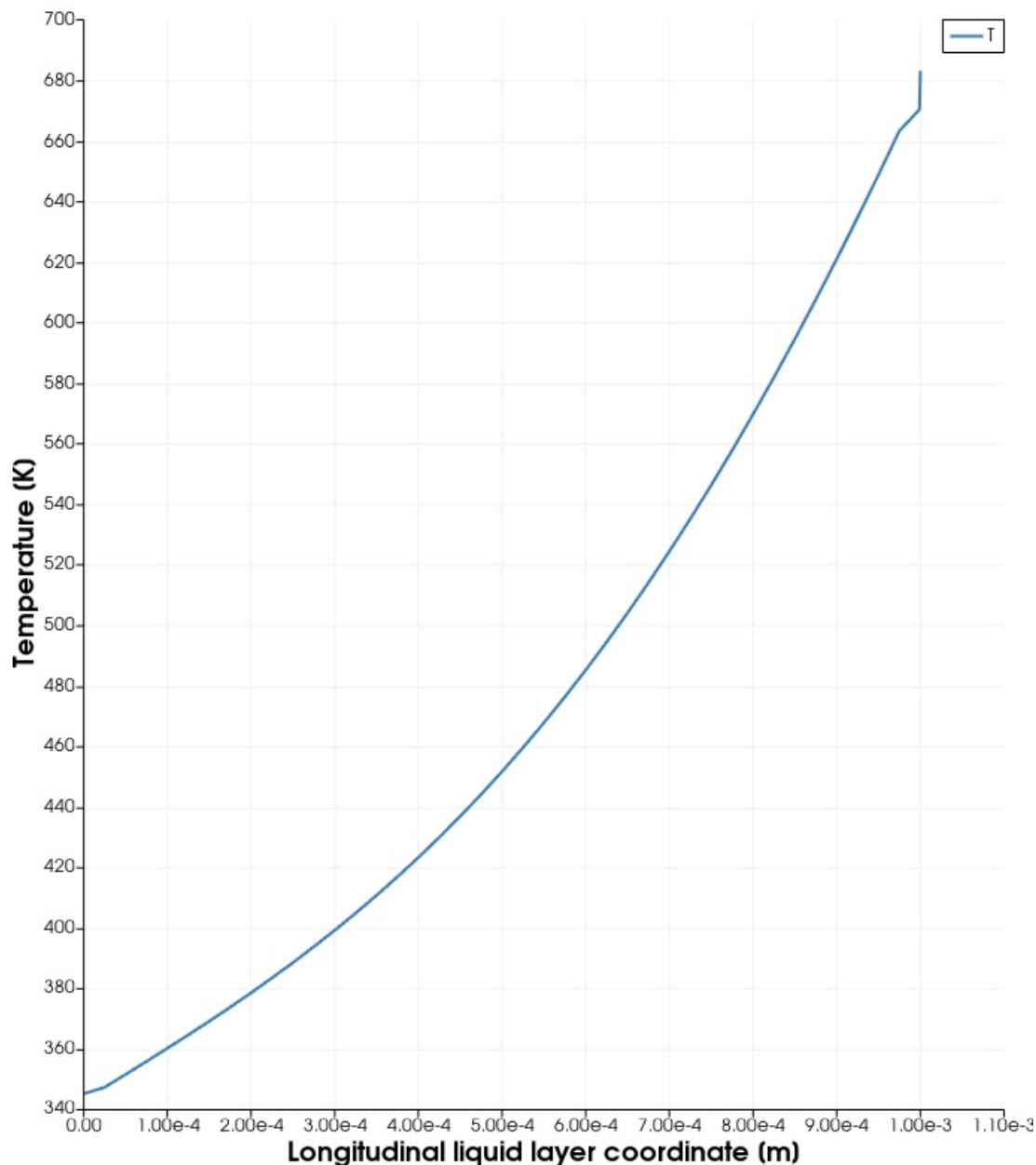
Figure 6.2.11: Temperature profile along the liquid layer for $h = 1$ mm, at a distance from the leading edge of 0.0227 m

6.2.4   Flame height

Considering the same mass flow rate, but a fuel formulation with 5% polymer additives, the flame height should shift upward. The study ongoing at SPLab on Sasol Wax 6805 indicates a flame location of 2.00 mm over the liquid surface in this case. This configuration has been tested with `chtMultiRegionFoam`, considering a melt layer thickness of 0.5 mm; a comparison on the reaching of the vaporization temperature and on the heat fluxes at the interfaces is here presented.

A convergence is reached after 1.73 s. The heat transferred at both interfaces results

71

to be lower of the order of 0.1 W compared to the case with pure paraffin. The values are reported as follows:

- **Liquid to solid:** Max/Min= -5.288x$10^3/-1.493$x10^5 W/m^2, Integral= -1.085 W

- **Gas to liquid:** Max/Min= -7.231x$10^3/= -2.161$x10^5 W/m^2, Integral= -1.533 W

The following graph shows the temperature at the liquid surface for the two different flame locations.
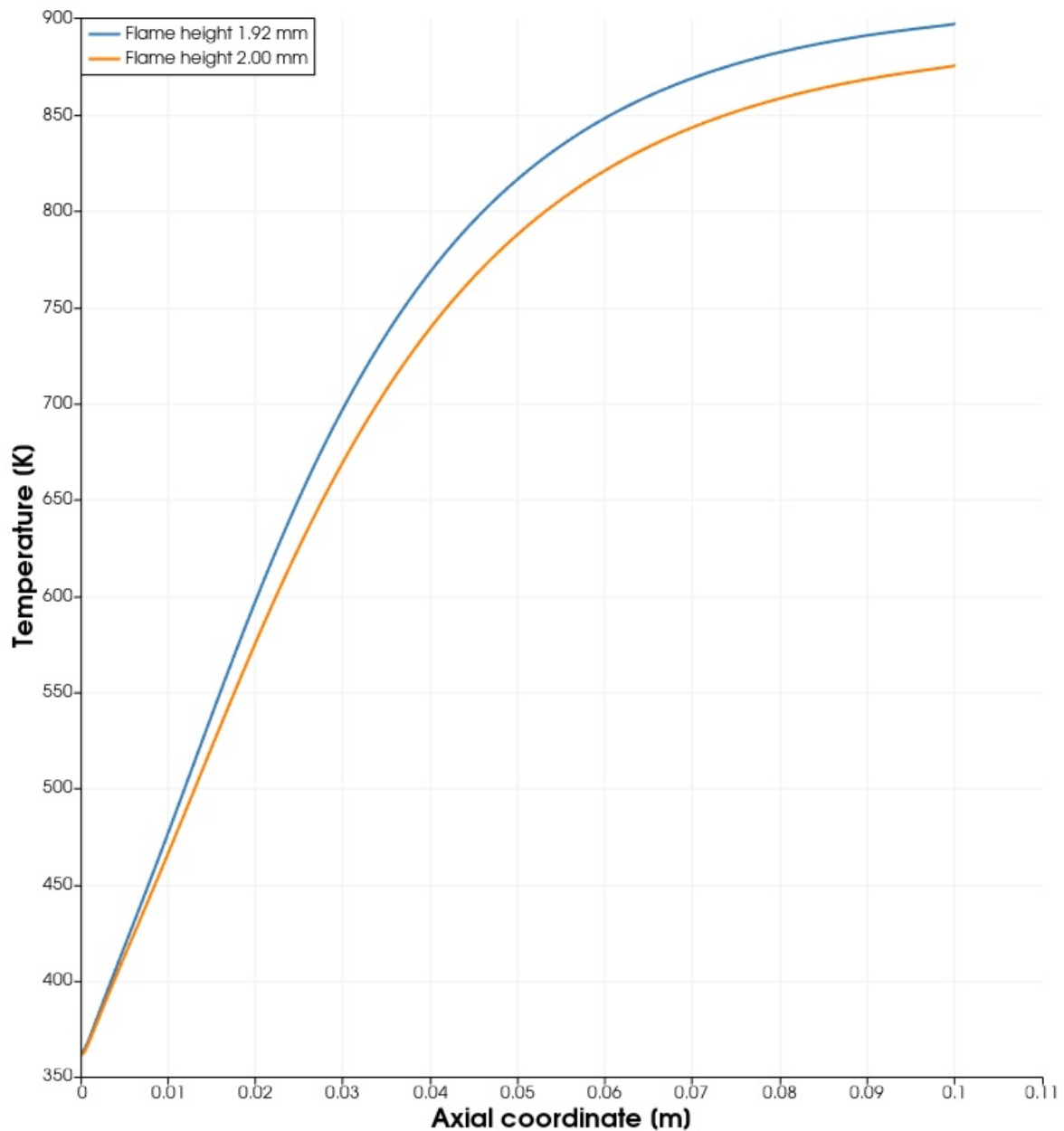

Figure 6.2.12: Temperature of the liquid fuel surface for $h = 0.5$ mm

As expected, the temperature at the same axial location results to be lower when the flame is located upwards. The difference is most significant far from the leading edge of

the grain. This also means that the vaporization condition for the fuel are reached more downstream, exactly at $0.0314\ m$; a difference of $8\text{x}10^{-5}m$ in the flame height results in a shift of $3.4\text{x}10^{-3}m$ of the vaporization temperature location. In Figure 6.2.13 the temperature profile in the liquid layer at the axial coordinate of $0.028\ m$ is reported for the two cases. It can be observed that, when the flame stands $2\ mm$ over the surface, the temperature is $24\ K$ lower than the vaporisation one.
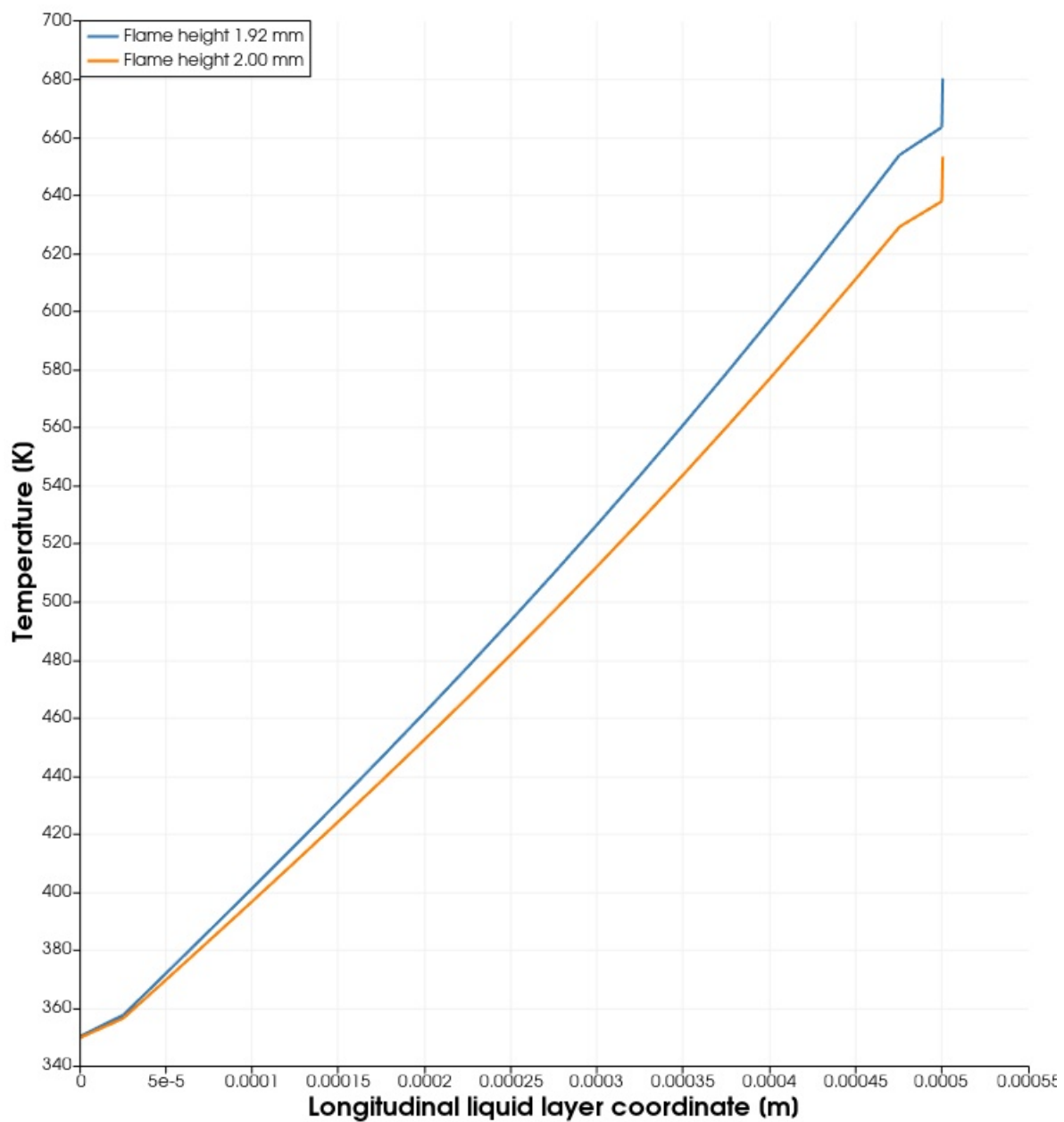

Figure 6.2.13: Temperature profile along the liquid layer for $h = 0.1\ mm$, at a distance from the leading edge of $0.028\ m$

6.2.5 Temperature profile up to the boundary layer

A last simulation is performed considering also the gas phase over the flame, up to the limit of the boundary layer. This region is composed of a mixture of combustion products and oxidiser. The average thickness of the boundary layer over the considered domain is of 5 mm, according to the ongoing study on Sasol Wax 6805. The new domain is then set as in Figure 6.2.14. The melt layer thickness of 0.5 mm and the flame height of 1.92 mm is imposed. The temperature between the two gas phase region, the fuel rich and the oxidiser rich, is the flame temperature. The top boundary condition for the oxidiser rich region is that of a fixed temperature of 512.085 K. This is an average value between the melting and the vaporisation temperature of the paraffin, which could represent a realistic value for the oxidiser free stream flow.

Figure 6.2.14: Domain for temperature profile evaluation up to the boundary layer

The thermophysical properties for each region are as follows. In the gas phase an average of combustion products and reactants is considered.

Solid Fuel		Liquid Fuel	
W	562 g/mol	W	562 g/mol
C_p	2529.84 $J/kg/K$	C_p	2987.53 $J/kg/K$
λ	0.329 $W/m/K$	λ	0.167 $W/m/K$
ρ	939 kg/m^3	ρ	740.3 kg/m^3
Fuel and products		**Oxidiser and products**	
W	41.43 g/mol	W	28.43 g/mol
C_p	2397 $J/kg/K$	C_p	1370 $J/kg/K$
μ	5.762x10^{-5} $kg/m/s$	μ	6.32x10^{-5} $W/m/K$
Pr	0.692	Pr	0.682

Table 6.2.2: Thermophysical properties used for the simulations

In Figure 6.2.15 the full temperature profile is reported, at the axial location at which the vaporization temperature is reached at the liquid surface.
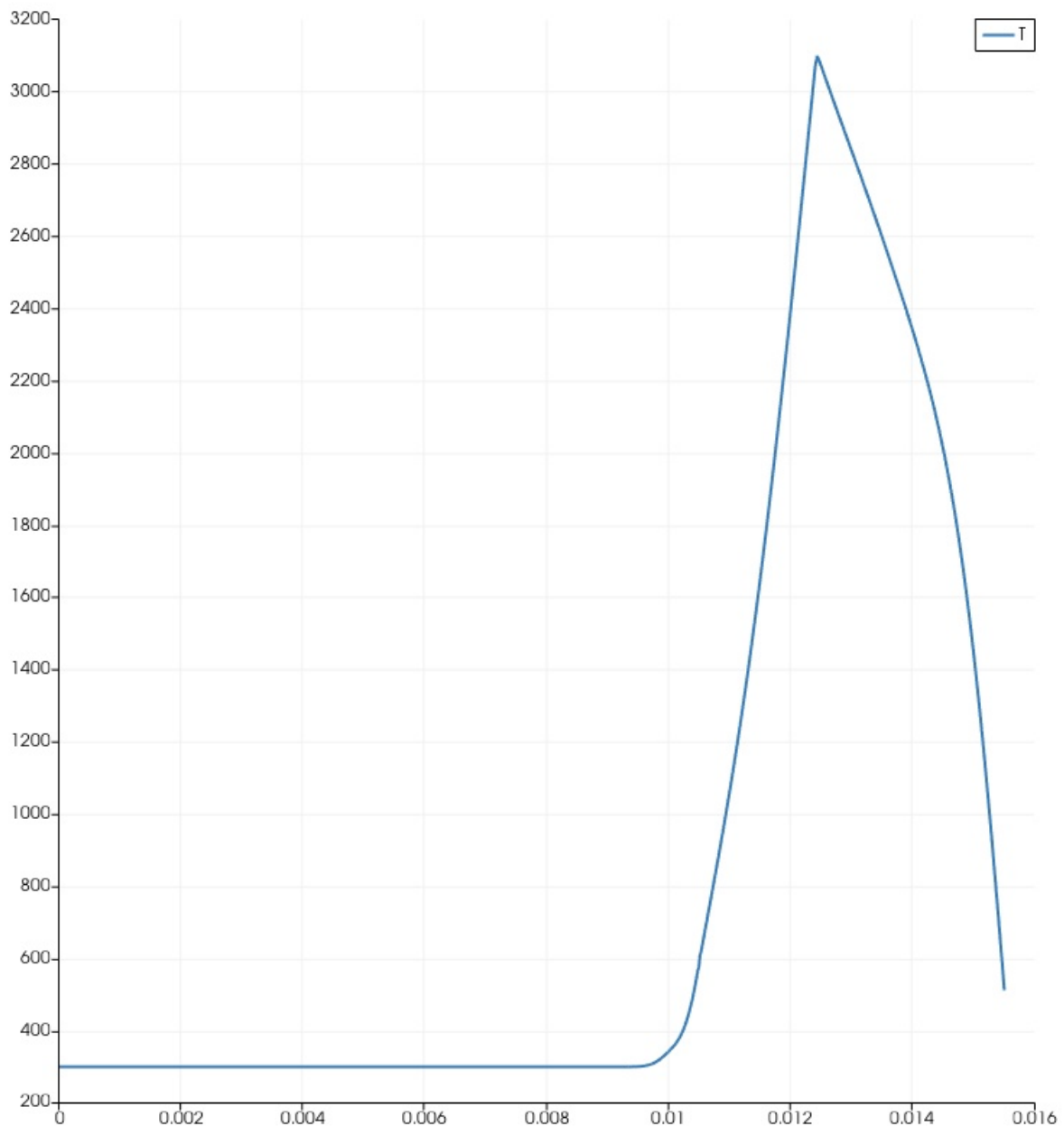
Figure 6.2.15: Temperature profile up to the boundary layer for $h = 0.5 \ mm$ at a distance from the leading edge of $0.028 \ m$

The highest temperature is imposed at the flame location; then it decreases towards the boundary of the domains where the ambient condition and the temperature of the free stream oxidiser are imposed. The heat flux conducted into the liquid layer and the temperature profile in the liquid layer do not change, since their geometry and boundary conditions are not modified.

Chapter 7

Conclusions and future work

7.1   Conclusions

Through a literature survey and the use of the empirical correlations, the characterisation of the transport and thermophysical properties of the paraffin-based fuel formulation has been achieved. Particularly, the evolution of the density and the viscosity with temperature based on the ABCs correlations and the one of the surface tension based on cross-referenced experimental works have been reported. This could be a basis for a database of paraffin properties to be employed in numerical simulations in the future.

The potential of the numerical analysis has been proved as an useful and convenient tool to compare different liquefying fuels, the sensitivity to some parameters and their influence in the hybrid rocket behaviour. Also, it would allow a better visualisation, and therefore, understanding of some processes. The two phenomenon analysed in the current work where:

- The entrainment of fuel droplets into the oxidiser flow, through the use of the the multiphase `interIsoFoam` solver of OpenFOAM. The behaviour with plane and wave initial interface has been investigated, showing that the presence of initial perturbation of the interface allows for an easier realization of the entrainment phenomenon. The three paraffins Sasol Wax 0907, Sasol Wax 6805 ans Sasol Wax 6003 have been analysed; the primary break-up happens earlier for Sasol Wax 6003, then for Sasol Wax 6805 and at the latest for Sasol Wax 0907. This is in accordance with the theoretical condition for entrainment onset of the extended hybrid combustion theory for liquefying fuels. Indeed, the onset is inversely proportional to the viscosity and the surface layer, which have an increasing value from Sasol Wax 6003 to Sasol Wax 0907. Also, a case run in a precedent numerical work has been re-run considering the surface tension value of the paraffin Sasol Wax 0907, which was an order of magnitude bigger. No entrainment was recorder in this case, contrary to the original one.

- The evolution of the temperature profile, under stationary boundary condition, with the solver `chtMultiRegionFoam` of OpenFOAM. The temperature trend along the three phases behaved as expected, raising from the ambient temperature of 300 K to the flame temperature. It was possible to observe that the temperature gradient

in the solid phase is concentrated in the millimeter close to the liquid layer; an exponential trend is recorded along all the three phases. Varying the thickness of the liquid layer higher temperature are reached at the liquid surface; the condition for evaporation is not met under a certain value of liquid layer thickness. Since the simulation was two-dimentional, it was also possible to highlight the temperature profile at the liquid surface along the chamber. A logarithmic trend was recorded, starting from a value around the fusion temperature at the leading edge of the grain, to an higher value at the end of domain. The surface temperature difference at the end of the chamber could increase of more than $500\ K$, varying the thickness from $0.1\ mm$ to $1\ mm$. The heat flux at the solid/liquid and liquid/gas interfaces is also reduced as the thickness is increased. The effect of flame location was also investigated; an higher position of the flame of $8\mathrm{x}10^{-5}m$ results in reduced surface temperature and heat flux.

7.2   Further developments

Further development to improve this work would include:

- Writing a model for the variation of specific heat and thermal conductivity with temperature for the paraffin formulations. Also, the variation of these parameters with pressure and with the inclusion of the additives should be investigated, wither through experimental tests and empirical correlations. This would be necessary to have a correct thermophysical model to use for the numerical simulations.

- The analysis of the entrainment could be coupled with the results obtained from the temperature profile, to insert more accurate transport properties; also, a coupling of this simulation with a multiphase solver for the evaporation could be considered, to analyse the residence time of the droplets.

- Regarding the temperature profile evaluation many efforts would still be required. A first step would be the inclusion of a radiation modeling to analyse the influence of radiative heat transfer. Secondly, the fluid part would need to be evaluated with a multiphase solver, that would record the distribution of the different compounds and return the interaction between the gas flow and the liquid layer.

A set of experimental tests should be conducted in order to validate the numerical simulations and to improve them, taking into account the main divergences with the experimental results. This would allow future research to rely on an extremely useful and cost-effective tool to compare the behaviour and the performance of different propellants and operational parameters.

Bibliography

[1] Standard test method for drop melting point of petroleum wax including petrolatum. *Manual on Hydrocarbon Analysis, 6th Edition* (1998).

[2] Chemical book: Paraffin wax(8002-74-2), Retrieved on 18 October 2020. https://www.chemicalbook.com/ProductMSDSDetailCB2854418_EN.htm.

[3] Food and agriculture organization of the united nations: Microcrystalline wax, Retrieved on 20 October 2020. http://www.fao.org/3/W6355E/w6355e0m.htm.

[4] Parchem: Styrene-ethylene/butylene-styrene block copolymer, Retrieved on 21 October 2020. https://www.parchem.com/chemical-supplier-distributor/Styrene -ethylene-butylene-styrene-block-copolymer-041541.aspx.

[5] ALTMAN, D., AND HUMBLE, R. Hybrid rocket propulsion systems. *Space Propulsion Analysis and Design* (1995), 379.

[6] BERNIGAUD, P. Numerical simulation for liquefying fuels.

[7] BICERANO, J. Pred1iction of polymer properties; marsel dekker, 1996.

[8] BRANTHAVER, J., AND HUANG, S.-C. Analytical separation methods in asphalt research. In *Advances in Asphalt Materials*. Elsevier, 2015, pp. 31–57.

[9] CANTWELL, B. Aircraft and rocket propulsion. *AA283 course* (2007).

[10] CANTWELL, B. J. The wax rocket. *IEEE Spectrum 51*, 12 (2014), 49–53.

[11] CHIAVERINI, M. J., SERIN, N., JOHNSON, D. K., LU, Y.-C., KUO, K. K., AND RISHA, G. A. Regression rate behavior of hybrid rocket solid fuels. *Journal of Propulsion and Power 16*, 1 (2000), 125–132.

[12] DE LUCA, L., BERNELLI ZAZZERA, F., MAGGI, F., TADINI, P., PARDINI, C., ANSELMO, L., GRASSI, M., PAVARIN, D., FRANCESCONI, A., BRANZ, F., ET AL. Active space debris removal by hybrid engine module. In *63rd International Astronautical Congress (IAC)* (2012), Curran Associates, pp. 2660–2673.

[13] DI MARTINO, G., MUNGIGUERRA, S., CARMICINO, C., AND SAVINO, R. Computational fluid-dynamic modeling of the internal ballistics of paraffin-fueled hybrid rocket. *Aerospace Science and Technology 89* (2019), 431–444.

[14] Di Martino, G. D., Carmicino, C., Mungiguerra, S., and Savino, R. The application of computational thermo-fluid-dynamics to the simulation of hybrid rocket internal ballistics with classical or liquefying fuels: A review. *Aerospace 6*, 5 (2019), 56.

[15] Faenza, M., Boiron, A. J., Haemmerli, B., and Verberne, C. J. The nammo nucleus launch: Norwegian hybrid sounding rocket over 100km. In *AIAA Propulsion and Energy 2019 Forum* (2019), p. 4049.

[16] Galfetti, L., Merotto, L., Boiocchi, M., Maggi, F., and De Luca, L. Ballistic and rheological characterization of paraffin-based fuels for hybrid rocket propulsion. In *47th AIAA/ASME/SAE/ASEE Joint Propulsion Conference & Exhibit* (2011), p. 5680.

[17] Garg, V. Paraffin based liquefying fuels for hybrid propulsion systems.

[18] Gariani, G., Maggi, F., and Galfetti, L. Simulation code for hybrid rocket combustion. In *46th AIAA/ASME/SAE/ASEE Joint Propulsion Conference & Exhibit* (2010), p. 6872.

[19] Gater, R. A., and L'Ecuyer, M. R. A fundamental investigation of the phenomena that characterize liquid-film cooling. *International Journal of Heat and Mass Transfer 13*, 12 (1970), 1925–1939.

[20] Gramer, D., Knuth, W., Rice, E., and St. Clair, C. Experimental investigation of a metallized cryogenic hybrid rocket engine. In *34th AIAA/ASME/SAE/ASEE Joint Propulsion Conference and Exhibit* (1998), p. 3509.

[21] Jones, R. Hybrid rocket engines use additive manufacturing to combine the advantages of solid and liquid propellants. stratasys, 2017.

[22] Karabeyoglu, A., Cantwell, B., and Stevens, J. Evaluation of the homologous series of normal alkanes as hybrid rocket fuels. In *41st AIAA/ASME/SAE/ASEE Joint Propulsion Conference & Exhibit* (2005), p. 3908.

[23] Karabeyoglu, M., Altman, D., and Cantwell, B. J. Combustion of liquefying hybrid propellants: Part 1, general theory. *Journal of Propulsion and Power 18*, 3 (2002), 610–620.

[24] Karabeyoglu, M., and Cantwell, B. J. Combustion of liquefying hybrid propellants: Part 2, stability of liquid films. *Journal of Propulsion and Power 18*, 3 (2002), 621–630.

[25] Knol, I. M., and Maicke, B. A. Simulation of surface instabilities in liquefying hybrid rocket fuels. In *AIAA Propulsion and Energy 2019 Forum* (2019), p. 3919.

[26] Kobald, M., Fischer, U., Tomilin, K., Petrarolo, A., and Schmierer, C. Hybrid experimental rocket stuttgart: a low-cost technology demonstrator. *Journal of Spacecraft and Rockets 55*, 2 (2018), 484–500.

[27] Kobald, M., Schmierer, C., Ciezki, H., Schlechtriem, S., Toson, E., and De Luca, L. Viscosity and regression rate of liquefying hybrid rocket fuels. *Journal of propulsion and power 33*, 5 (2017), 1245–1251.

[28] Kobald, M., Toson, E., Ciezki, H., Schlechtriem, S., Di Betta, S., Coppola, M., and DeLuca, L. Rheological, optical, and ballistic investigations of paraffin-based fuels for hybrid rocket propulsion using a two-dimensional slab-burner. *Progress in Propulsion Physics 8* (2016), 263–282.

[29] Kuo, K. K., and Chiaverini, M. J. *Fundamentals of hybrid rocket combustion and propulsion.* American Institute of Aeronautics and Astronautics, 2007.

[30] Lai, S.-M., Chen, W.-C., and Chen, C.-M. Preparation, structure, and properties of styrene-ethylene-butylene-styrene block copolymer/clay nanocomposites: Part ii fracture behaviors. *European polymer journal 44*, 11 (2008), 3535–3547.

[31] Larson, C., DeRose, M., Pfeil, K., and Carric, P. High pressure combustion of cryogenic hybrid fuels in a lab-scale burner. In *Proceedings of the 1996 JANNAF Joint Propulsion Conference, Albuquerque, NM* (1996).

[32] Locca, A. Indagine sperimentale della fenomenologia dell'entrainment in combustibili per endoreattori ibridi.

[33] Lyne, J. E., Brigham, A., Savery, R., Karcher, K., Pyron, J., Adams, L., Reagan, G., Furches, H., Sola, D., and Melendez, L. The use of a 3-d printed, polymer matrix containing pulverized fuel in a hybrid rocket. In *2018 Joint Propulsion Conference* (2018), p. 4597.

[34] Majdalani, J., and Cecil, O. M. Hybrid rockets: To wax or to whirl?, 2017.

[35] Marano, J. J., and Holder, G. D. A general equation for correlating the thermophysical properties of n-paraffins, n-olefins, and other homologous series. 3. asymptotic behavior correlations for thermal and transport properties. *Industrial & engineering chemistry research 36*, 6 (1997), 2399–2408.

[36] Marxman, G., and Gilbert, M. Turbulent boundary layer combustion in the hybrid rocket. In *Symposium (International) on Combustion* (1963), vol. 9, Elsevier, pp. 371–383.

[37] Marxman, G., Wooldridge, C., and Muzzy, R. Fundamentals of hybrid boundary-layer combustion. In *Progress in Astronautics and Rocketry*, vol. 15. Elsevier, 1964, pp. 485–522.

[38] Marxman, G. A. Boundary-layer combustion in propulsion. In *Symposium (international) on Combustion* (1967), vol. 11, Elsevier, pp. 269–289.

[39] Mosher, M. Organic chemistry. (morrison, robert thornton; boyd, robert neilson), 1992.

[40] Muzzy, R. Applied hybrid combustion theory. In *8th Joint Propulsion Specialist Conference* (1972), p. 1143.

[41] Nigmatulin, B. I., Klebanov, L., and Kroshilin, A. Critical heat transfer in the transient boiling of vapor-liquid annular-mist flows. *Teplofizika vysokikh temperatur 18*, 6 (1980), 1242–1251.

[42] NIGMATULIN, R., NIGMATULIN, B., KHODZHAEV, Y. D., AND KROSHILIN, V. Entrainment and deposition rates in a dispersed-film flow. *International journal of multiphase flow 22*, 1 (1996), 19–30.

[43] OLSSON, E. A description of isoadvector-a numerical method for improved surface sharpness in two-phase flows. *Proceedings of CFD with OpenSource Software, Edited by Nilsson. H* (2017).

[44] PARAVAN, C., BISIN, R., CARLOTTI, S., MAGGI, F., AND GALFETTI, L. Diagnostics for entrainment characterization in liquefying fuel formulations. In *2018 Joint Propulsion Conference* (2018), p. 4663.

[45] PARAVAN, C., GALFETTI, L., AND MAGGI, F. A critical analysis of paraffin-based fuel formulations for hybrid rocket propulsion. In *53rd AIAA/SAE/ASEE Joint Propulsion Conference* (2017), p. 4830.

[46] PISCITELLI, F., SACCONE, G., GIANVITO, A., COSENTINO, G., AND MAZZOLA, L. Characterization and manufacturing of a paraffin wax as fuel for hybrid rockets. *Propulsion and Power Research 7*, 3 (2018), 218–230.

[47] PROSEN, E., AND ROSSINI, F. Heats of combustion and formation of the paraffin hydrocarbons at 25-degrees-c. *Journal of Research of the National Bureau of Standards 34*, 3 (1945), 263–269.

[48] ROENBY, J., BREDMOSE, H., AND JASAK, H. A computational method for sharp interface advection. *Royal Society open science 3*, 11 (2016), 160405.

[49] SCHMIERER, C., KOBALD, M., FISCHER, U., TOMILIN, K., PETRAROLO, A., AND HERTEL, F. Advancing europe's hybrid rocket engine technology with paraffin and lox. In *Proceedings of the 8th European Conference for Aeronautics and Space Sciences* (2019).

[50] SINGHAL, A. Tutorial to set up a case for chtmultiregionfoam in openfoam 2.0. 0. *University of Luxembourg, Luxembourg* (2014).

[51] SMOOT, L., AND PRICE, C. Pressure dependence of hybrid fuel regression rates. *AIAA Journal 5*, 1 (1967), 102–106.

[52] STAGGS, J. The heat of gasification of polymers. *Fire safety journal 39*, 8 (2004), 711–720.

[53] STRAND, L., JONES, M., RAY, R., AND COHEN, N. Characterization of hybrid rocket internal heat flux and htpb fuel pyrolysis. In *30th Joint Propulsion Conference and Exhibit* (1994), p. 2876.

[54] STRIEDER, W., AND ARIS, R. Diffusion limited reactions. In *Variational Methods Applied to Problems of Diffusion and Reaction*. Springer, 1973, pp. 42–58.

[55] SURMACZ, P., AND RARATA, G. Hybrid rocket propulsion development and application, 2009.

[56] SUTTON, G. P., AND BIBLARZ, O. *Rocket propulsion elements*. John Wiley & Sons, 2016.

[57] WOOLRIDGE, C., AND KIER, R. An investigation of combustion instability in hybrid rockets.